

# Toward simultaneous flow and pressure assessment in large arteries using non-invasive ultrasound

**Citation for published version (APA):**

Beulen, B. (2009). *Toward simultaneous flow and pressure assessment in large arteries using non-invasive ultrasound*. [Phd Thesis 1 (Research TU/e / Graduation TU/e), Biomedical Engineering]. Technische Universiteit Eindhoven. <https://doi.org/10.6100/IR644053>

**DOI:**

[10.6100/IR644053](https://doi.org/10.6100/IR644053)

**Document status and date:**

Published: 01/01/2009

**Document Version:**

Publisher's PDF, also known as Version of Record (includes final page, issue and volume numbers)

**Please check the document version of this publication:**

- A submitted manuscript is the version of the article upon submission and before peer-review. There can be important differences between the submitted version and the official published version of record. People interested in the research are advised to contact the author for the final version of the publication, or visit the DOI to the publisher's website.
- The final author version and the galley proof are versions of the publication after peer review.
- The final published version features the final layout of the paper including the volume, issue and page numbers.

[Link to publication](#)

**General rights**

Copyright and moral rights for the publications made accessible in the public portal are retained by the authors and/or other copyright owners and it is a condition of accessing publications that users recognise and abide by the legal requirements associated with these rights.

- Users may download and print one copy of any publication from the public portal for the purpose of private study or research.
- You may not further distribute the material or use it for any profit-making activity or commercial gain
- You may freely distribute the URL identifying the publication in the public portal.

If the publication is distributed under the terms of Article 25fa of the Dutch Copyright Act, indicated by the "Taverne" license above, please follow below link for the End User Agreement:

[www.tue.nl/taverne](http://www.tue.nl/taverne)

**Take down policy**

If you believe that this document breaches copyright please contact us at:

[openaccess@tue.nl](mailto:openaccess@tue.nl)

providing details and we will investigate your claim.

**Toward simultaneous flow and pressure  
assessment in large arteries using  
non-invasive ultrasound**

A catalogue record is available from the Eindhoven University of Technology Library

ISBN: 978-90-386-1932-3

Cover Design by Dennis Beulen

Printed by Universiteitsdrukkerij TU Eindhoven, Eindhoven, The Netherlands

The scientific work was financially supported by SenterNovem of the Dutch Ministry of Economic Affairs (IS042015)

# **Toward simultaneous flow and pressure assessment in large arteries using non-invasive ultrasound**

PROEFSCHRIFT

ter verkrijging van de graad van doctor  
aan de Technische Universiteit Eindhoven,  
op gezag van de rector magnificus, prof.dr.ir. C.J. van Duijn,  
voor een commissie aangewezen door het College voor Promoties  
in het openbaar te verdedigen op  
dinsdag 1 september 2009 om 16.00 uur

door

Bart Wilhelmus Anna Maria Mathis Beulen

geboren te Geleen

Dit proefschrift is goedgekeurd door de promotor:

prof.dr.ir. F.N. van de Vosse

Copromotor:

dr.ir. M.C.M. Rutten

# Contents

<b>Summary</b>	<b>1</b>
<b>1 Introduction</b>	<b>3</b>
1.1 Physiology and pathology . . . . .	4
1.2 Ultrasound . . . . .	6
1.3 Assessment of hemodynamic variables . . . . .	11
1.4 Aim and outline . . . . .	13
<b>2 A time-periodic approach for fluid structure interaction in distensible vessels</b>	<b>15</b>
2.1 Introduction . . . . .	16
2.2 Materials and methods . . . . .	18
2.3 Results . . . . .	26
2.4 Applications . . . . .	27
2.5 Discussion . . . . .	29
2.6 Conclusion . . . . .	32
<b>3 Perpendicular ultrasound velocity measurement by 2D cross correlation of RF data: experiments and validation</b>	<b>33</b>
3.1 Introduction . . . . .	34
3.2 Materials and methods . . . . .	36
3.3 Results . . . . .	43
3.4 Discussion . . . . .	45
3.5 Conclusion . . . . .	49
<b>4 Estimation of volume flow in Curved Tubes based on Analytical and Computational Analysis of Axial Velocity Profiles</b>	<b>51</b>
4.1 Introduction . . . . .	52
4.2 Methods . . . . .	55
4.3 Results . . . . .	60
4.4 Discussion . . . . .	68
4.5 Conclusion . . . . .	72
<b>5 Flow estimation in curved vessels by means of non-invasive ul-</b>	

<b>trasound</b>	<b>75</b>
5.1 Introduction . . . . .	76
5.2 Material and methods . . . . .	78
5.3 Results . . . . .	85
5.4 Discussion . . . . .	89
5.5 Conclusion . . . . .	93
<b>6 Towards a non-invasive pressure assessment</b>	<b>95</b>
6.1 Introduction . . . . .	96
6.2 Material and methods . . . . .	100
6.3 Results . . . . .	107
6.4 Discussion . . . . .	111
6.5 Conclusion . . . . .	114
<b>7 General conclusion</b>	<b>115</b>
7.1 Introduction . . . . .	116
7.2 Study results . . . . .	116
7.3 Clinical perspective . . . . .	119
7.4 Conclusion . . . . .	121
<b>Bibliography</b>	<b>123</b>
<b>A Analytical solutions for the axial velocity (<math>w</math>)</b>	<b>135</b>
A.1 Derivation by Dean . . . . .	135
A.2 Derivation by Topakoglu . . . . .	136
A.3 Derivation by Siggers & Waters . . . . .	136
<b>Samenvatting</b>	<b>139</b>
<b>Dankwoord</b>	<b>141</b>
<b>Curriculum Vitae</b>	<b>143</b>

# Summary

## **Toward simultaneous flow and pressure assessment in large arteries using non-invasive ultrasound**

In clinical practice, ultrasound is frequently used as a non-invasive method to estimate geometric properties of large arteries such as diameter and wall thickness and haemodynamic variables such as blood velocity. For the purpose of deducing biomechanical parameters and hemodynamic variables that are related to the development of cardiovascular disease (CVD), such as compliance and vascular impedance, the assessment of only geometry and blood velocity does not suffice. A simultaneous and preferably non-invasive assessment of flow and pressure is required.

Presently applied ultrasound methods do not allow an accurate simultaneous assessment of flow and pressure. For flow estimation, often two measurements are performed: a measurement of the diameter (ultrasound beam positioned perpendicular with respect to the vessel) and a measurement of the maximum axial velocity by means of Doppler ultrasound (ultrasound beam positioned at a non-perpendicular angle with respect to the vessel). By subsequently assuming a certain velocity distribution, e.g., a Poiseuille or Womersley profile, flow is estimated. However, in-vivo, most arteries are tapered, curved and bifurcating, causing the axial velocity distribution to be altered by transversal velocities, resulting in asymmetrical axial velocity profiles. This causes an inaccurate flow estimation since the assumed velocity distributions are only valid for flow in straight vessels. Additionally, a simultaneous accurate assessment of blood velocity and wall motion is not feasible, further deteriorating the flow estimate and hampering an accurate pressure assessment.

In this study, Particle Image Velocimetry (PIV) based algorithms were applied to RF-data acquired using a commercially available clinically approved ultrasound system. This allowed to estimate velocity components perpendicularly to the ultrasound beam, thus enabling a simultaneous and accurate assessment of wall position and axial velocity profiles. The velocity estimation technique was validated by comparing velocity profile measurements performed on steady and unsteady flow in a straight vessel in an experimental setup to computational fluid

dynamics (CFD) computations. Excellent agreement was found for the axial velocity profile. Integration of the measured axial velocity profile resulted in an accurate flow estimate.

Since in-vivo, most vessels are curved, the velocity assessment method was subsequently validated for application to flow in such geometries. In the experimental setup, axial velocity profiles were measured for both steady and unsteady flow in a curved vessel. Measured velocity profiles were again compared to CFD computations. Also in this case, an excellent agreement was found.

An analytical and CFD based study on flow in curved vessels was performed in order to accurately estimate flow from the measured asymmetrical axial velocity profiles. This study resulted in the  $\cos \theta$ -method. Application of the  $\cos \theta$ -method to the asymmetric axial velocity profiles as measured in the curved vessel resulted in an accurate flow estimate for both steady and unsteady flow. A significant improvement with respect to the presently used flow approximation methods was found. For a physiologically relevant flow, the average deviation between the  $\cos \theta$ -integration based flow estimate and reference flow was found to be about 5%, compared to an average deviation of 20% for both the Poiseuille and Womersley approximations.

Finally, efforts were made to estimate local pressure from a single non-invasive ultrasound measurement by combining a vessel diameter measurement with a simultaneous estimation of the local compliance. The local compliance was estimated by measuring the local pulse wave velocity (PWV). Various methods for the estimation of local PWV were evaluated in the experimental setup. The QA-method, a method in which the local PWV is estimated from the ratio between changes in flow and changes in cross-sectional area of the vessel, was found to offer an accurate estimate of the local PWV. By combining the PWV estimate with the diameter waveform an accurate pressure estimation was obtained, indicating that a non-invasive pressure assessment by means of ultrasound is viable.

Although the measurements performed in this study were restricted to a experimental setup, prospects for in-vivo application of the introduced methods look promising. The introduced methods enable an improved assessment of the condition of the vascular system, which in future can be applied to obtain information of the effect of therapeutic interventions and to identify factors which are characteristic for the development of CVD.

## **Chapter 1**

# **Introduction**

## 1.1 Physiology and pathology

### 1.1.1 The cardiovascular system

The major function of the cardiovascular system is transportation of oxygen and nutrients to the tissues, and waste products from the tissues. The cardiovascular system consists of the heart and the vascular system. The heart is a four-chambered pump that drives the blood through the vascular system by cyclic contraction and relaxation of the cardiac muscle.

Blood mainly consists of blood plasma with red blood cells (erythrocytes), white blood cells (leucocytes) and blood platelets (thrombocytes). The volume fraction of the erythrocytes (haematocrit) in blood in healthy subjects is approximately 45%. As a result, these cells dominate the rheological behaviour of the blood. At high shear rates, the erythrocytes align with the flow and deform, resulting in decreased blood viscosity. At low shear rates, the erythrocytes aggregate face to face when they are brought in to contact with each other. These aggregates are known as rouleaux and their presence increases the blood viscosity. At near zero shear rate, secondary aggregation occurs, leading to the formation of a rouleaux network, further increasing the viscosity. The deformability and aggregation of the erythrocytes result in shear thinning behaviour of blood in simple shear (Figure 1.1).

The vascular system can be divided into the systemic and the pulmonary circulation. In the systemic circulation oxygenated blood is carried away from the heart to the body and deoxygenated blood is transported back to the heart. In the pulmonary circulation, oxygen-depleted blood is transported away from the heart, to the lungs, and oxygenated blood returns to the heart. Both circulations consist of a network of arteries, arterioles, capillaries, venules and veins.

Blood is transported to the tissue by the arteries. The smallest branches of the arterial system are the arterioles. The arterioles can adapt the local blood flow to the needs of the tissue by dilating or expanding the vessel lumen. In the capillaries, the blood velocity is low, allowing the exchange of oxygen, nutrients and waste products. The deoxygenated blood is then collected by venules, which gradually join into progressively larger veins. The veins transport the blood from the tissue back to the heart.

The periodic contraction of the cardiac muscle results in a pulsatile blood volume flow and pressure in the arterial system. The aorta and the larger arteries have pronounced elastic properties and act as a buffer for the blood volume ejected from the heart in the systolic phase of the heart cycle. The smaller arteries, arterioles and capillaries are mainly resistive to flow. As a result pressure and flow propagate as waves through the arterial system. The pressure and flow pulses are attenuated as they propagate away from the heart. At the level of the capillaries, both pressure and flow are approximately stationary. A good perfusion of the tissue is accomplished when this steady pressure level is adequately high.

The wall of the larger arteries is composed of three main layers. The innermost

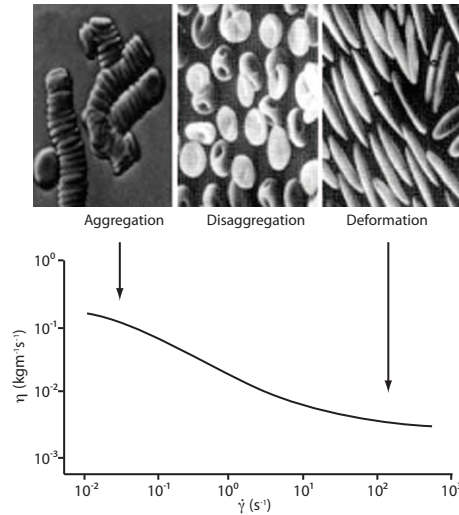


Figure 1.1: Top: aggregation (rouleaux), disaggregation and deformation. Bottom: viscosity in steady shear of normal blood (adapted from Chien et al. (1970)).

layer, the tunica intima consists of a single layer of endothelial cells, supported by an internal elastic lamina. The endothelial cells are in direct contact with the blood flow. The middle layer, the tunica media, is made up of smooth muscle cells and elastic tissue and is usually the thickest layer. The orientation and content of smooth muscle cells and elastic tissue mainly determine the mechanical properties of the artery. The outermost layer, the tunica externa (adventitia) is primarily composed of collagen and anchors the artery to its surroundings.

### 1.1.2 Cardiovascular disease

Diseases involving the heart and blood vessels (arteries and veins), often referred to as cardiovascular disease (CVD), are a common cause of death in adults in the western society (Petersen et al., 2005). The most common type of CVD is atherosclerosis, a disease in which, locally, plaques build up at the inside of arteries. In-vivo studies indicate that atherogenesis, the developmental process that may lead to atherosclerosis, is influenced by local hemodynamics. It has been shown that locations where low and oscillating wall shear stress occur correlate well with the location where atherosclerotic lesions form (Caro et al., 1971; Zarins et al., 1983; Friedman et al., 1992). Typical locations are inside bends (e.g., in coronary arteries) and non-divider walls of bifurcations (e.g., in the carotid bifurcation).

The formation of plaques within an artery causes hardening of the artery, resulting in loss of elasticity of the arterial wall and thus an decrease of compliance. Arteries

with a decreased compliance cannot adequately buffer the volume ejected from the heart, resulting in an increased pulse- and systolic pressure. Additionally, the velocity of the pressure and flow pulses increases, causing reflections to arrive at the heart during the ejection phase, which contributes to an increase of systolic pressure (Schiffrin, 2004). Subsequently, the increased load on the heart can result in ventricular hypertrophy (Boutouyrie et al., 1995). At a later stage, atherosclerosis may cause local narrowing of the vessel's lumen. A significant narrowing of a vessel's lumen causes a decreased mean flow to the parts of the vascular tree distal to the stenosis, which can result in an insufficient blood supply to the tissue and organs fed by the vessel. Estimation of the arterial impedance (the transfer function between pressure and volume flow) can be a valuable method to estimate the condition of the vessel.

Monitoring factors such as compliance and arterial impedance allow the assessment of CVD. However, these biomechanical properties can only be derived if local blood pressure, blood volume flow, and dynamic geometrical information of the vessel wall (diameter, distension (change in diameter), vessel wall thickness and curvature) are known. In clinical practice, these hemodynamic and geometrical parameters cannot always be assessed in a direct way at the required specific sites in the arterial tree, especially if these measurements must be performed non-invasively. As a result, often substitute parameters are used. An alternative way to assess arterial compliance is to use the pulse wave velocity (PWV) (Frank, 1922; Lehmann et al., 1993); the stiffer the artery, the higher the PWV will be. Studies of arterial impedance in humans are hampered by the lack of reliable non-invasive techniques to simultaneously record pressure and flow locally as a function of time. Therefore, vessel diameter and centreline velocity have been applied as a substitute for pressure and flow (Brands et al., 1996). However, this approximation is only valid for fully developed Newtonian flow in straight geometries with linearly elastic wall material properties and small deformations. In-vivo, blood is non-Newtonian and flow is not fully developed, vessels are curved with non-linear vessel wall material properties and the deformation of the vessel wall is relatively large. For an accurate estimation of arterial impedance, accurate estimations of blood volume flow and pressure are required.

Various imaging modalities exist (Table 1.1), which allow to monitor the development of CVD. Because of its high resolution, approximately realtime acquisition and low cost, ultrasound is often preferred.

## 1.2 Ultrasound

Ultrasound is a pressure wave with a frequency above the audible range (20 Hz - 20 kHz). In clinical ultrasound diagnostics, ultrasound in the range of frequencies between 2 MHz and 10 MHz (Kremkau, 1998) is applied to non-invasively assess blood velocity, blood volume flow and blood vessel wall properties. The choice of the applied frequency depends amongst others on the required penetration depth and spatial resolution along the sound propagation direction. Since the attenua-

Table 1.1: Comparison of imaging modalities: ultrasound, computed tomography (CT) and magnetic resonance imaging (MRI). Adapted from Szabo (2004).

	Ultrasound	CT	MRI
What is imaged	Mechanical properties Acoustic impedance	Tissue absorption	Biochemistry ( $T_1$ and $T_2$ )
Acces	Small window	Circumferential around body	Circumferential around body
Acquisition time	Approximately realtime	Hours	Hours
Spatial resolution	0.3 – 3 mm	$\approx 1$ mm	$\approx 1$ mm
Penetration	Frequency dependent 3-25 cm	Excellent	Excellent
Safety	Very good	Ionizing radiation	Very good
Cost	€100k	€1M	€5M
Portability	Excellent	Poor	Poor

tion of the ultrasound wave increases with increasing frequency, the penetration depth decreases with increasing frequency. Conversely, because the resolution is proportional to the wavelength of the applied sound wave, the resolution increases with increasing frequency. For examining superficial arteries, generally ultrasound systems with a transmission frequency of about 7 – 10 MHz are applied, which results in a resolution of approximately 300  $\mu\text{m}$  and a penetration depth that is limited to about 6 – 9 cm.

Pulses of ultrasound are transmitted into the tissue by means of a transducer, which employs piezo electric crystals to convert an electrical signal into an acoustical wave. As a single ultrasound pulse travels through the tissue, the pulse is partly reflected at acoustic boundaries. Additionally, the pulse is attenuated due to scattering and dampening. At the transducer, the ultrasound echo is collected and transformed back into an electric radio frequency signal (RF-signal) by means of the same piezo-electric crystal. Subsequently, echo arrival time is converted into the distance from which the echo originated by assumption of a specific sound propagation speed in the tissue,  $c$ . From one emitted pulse of ultrasound, one scan line is generated by calculating the envelope of the corresponding RF-signal (Figure 1.2 left). Scan lines are generated at the pulse repetition frequency,  $f_{PRF}$ . M-mode images are generated by displaying the scan line as a function of time. An M-mode image provides information on tissue motion along the ultrasound beam (Figure 1.2 centre). A 2D cross section of a tissue can be acquired by either sending out pulses of ultrasound from the same starting point in different directions or by sending out pulses of ultrasound from different starting points. In linear array transducers, a 1D array of piezo transducers is employed to generate parallel scan lines, resulting in a rectangular cross sectional image, which is called a B-mode image (Figure 1.2 right). The B-mode image contains tissue information in axial and transverse direction at a single time point.

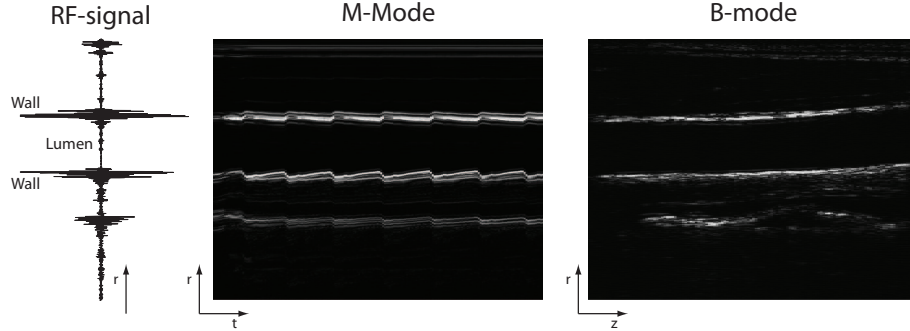


Figure 1.2: From left to right: RF-signal, M-mode image and B-mode image of the common carotid artery. In the RF-signal, the high amplitude wall reflections are clearly visible. As expected, the amplitude of the blood scattering signal is much smaller. In the M-mode image, the envelope of the RF-signal is presented as a function of time in order to provide information of tissue motion in radial direction; the cyclic diameter change is clearly visible. A linear array transducer is applied to generate a B-mode image which provides a 2D cross section of the vessel.

In ultrasound imaging, the lateral resolution (perpendicular to the sound propagation direction) is determined by the ultrasound beam width in the scan plane. To improve lateral resolution, a group of elements is employed to generate the ultrasound pulse. By introducing delays to the employed group of transducers (Figure 1.3), electronic focussing can be accomplished. At the focus point, the lateral beam width is the smallest (and there the best lateral focus is obtained), while away from the focus point, the lateral beam width increases. The combination of transmission and reception focussing greatly improves lateral resolution.

RF-signals consist of contributions due to reflections and scattering. When the dimensions of the acoustic boundary are larger than the wavelength of the ultrasound wave transmitted, the sound wave will partly reflect. Reflection will take place under the same angle as the angle of incidence. However, when the dimensions of the acoustic boundary becomes small compared to the wavelength of the ultrasound wave transmitted, the ultrasound wave will be scattered in all directions. For example, when imaging a blood vessel, the blood will cause scattering because the dimensions of a red blood cell ( $\phi \approx 10 \mu\text{m}$ ) and the interspacing between them is much smaller than the ultrasound wavelength ( $\lambda = c/f \approx 300 \mu\text{m}$ ), reflection will occur at the lumen-wall interface.

The signals due to scattering and reflection are mixed with each other, with noise and reverberations. Reverberations are reflections from in between acoustic boundaries (secondary reflections). These secondary reflections, e.g., often manifest themselves in the lumen of the blood vessel. The power of reflections is in the order of 40 – 60 dB larger than the power of the scattering, while the power of the reverberations is in the order of 20 dB higher than the power of the scattering

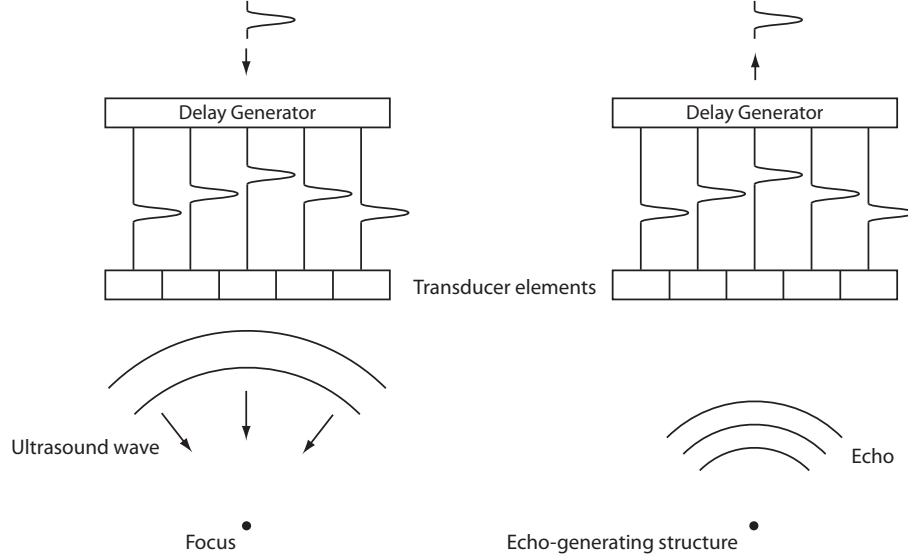


Figure 1.3: The transmitted ultrasound pulse can be focussed by introducing delays to the employed group of transducers (left). Similarly, when the array is receiving echoes, a listening focus can be attained by introducing delays (right).

(Hoeks et al., 1991). Frequency domain analysis allows a discrimination between reflection and scattering components, based on the differences in temporal properties. The schematical power spectral density distribution presented in Figure 1.4 shows the major RF-signal components:

1. Reflections induced by stationary or slowly moving tissue (high spectral power, narrow bandwidth, low temporal mean frequency)
2. Scattering induced by red blood cells (low spectral power, wide bandwidth, temporal mean frequency depending on blood flow velocity)
3. Reverberations (low spectral power, narrow bandwidth, low temporal mean frequency)
4. Noise (low spectral power, uniform spectral distribution)

For blood velocity assessment, generally a filter (e.g. an ordinary high pass filter) is applied to discriminate the scattering from the reflections (Szabo, 2004; Evans et al., 1989). Subsequently, the component of the blood velocity vector,  $\mathbf{v}$ , along the ultrasound propagation direction can be estimated by measuring the Doppler frequency shift between the incident ultrasound pulse and the received echo:

$$v = \frac{f_{DC}}{2f_0}, \quad (1.1)$$

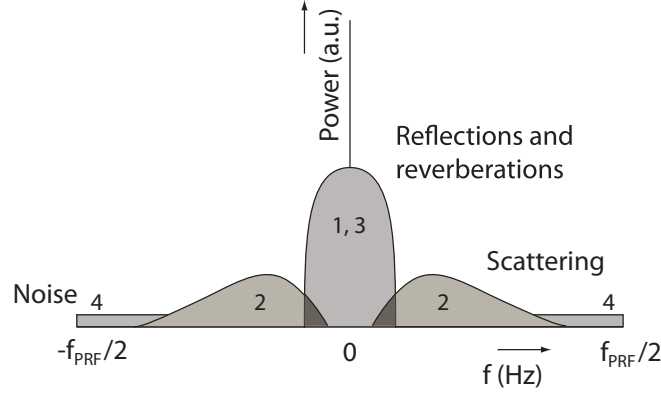


Figure 1.4: Schematic representation of the power spectrum distribution of an RF-signal, indicating the contributions of reflections, scattering and noise.

in which  $v$  is the velocity component of the blood in the direction of the ultrasound beam,  $c$  the speed of sound,  $f_0$ , the transmitted frequency and  $f_D$ , the Doppler shift. By estimation of the insonation angle  $\alpha$  between the ultrasound propagation direction and the blood velocity vector (Figure 1.5), the magnitude of the blood velocity vector can be estimated by:

$$|\mathbf{v}| = \frac{f_D c}{2 f_0 \cos \alpha}. \quad (1.2)$$

For the assessment of velocity distribution, small sample volumes are applied to the RF-signal, which enable to acquire depth dependent Doppler shifts.

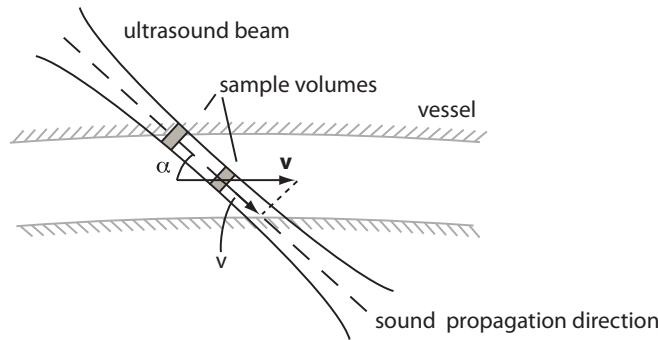


Figure 1.5: For each sample volume, velocity is estimated by application of the Doppler equation (1.2). The Doppler angle  $\alpha$  is the angle between the velocity vector and the sound propagation direction.

Information on vessel wall motion can be obtained by selecting a M-line perpen-

pendicular to the artery of interest and processing the RF signal. This allows the accurate estimation of the vessel diameter waveform (Hoeks et al., 1990, 1997), which is closely related to local pressure inside the vessel. Since ultrasound RF data of blood vessels contains both information on blood velocity and vessel wall motion it offers a promising possibility for the simultaneous, non-invasive assessment of local volume flow and pressure.

### 1.3 Assessment of hemodynamic variables

The ability to accurately, and preferably simultaneously and non-invasively assess pressure and flow at specific sites in the cardiovascular system enables the estimation of biomechanical parameters, such as compliance and vascular impedance. This allows the assessment of the condition of the vascular system, enabling to obtain information of the effect of therapeutic interventions and to identify hemodynamic factors which are characteristic for the development of CVD.

For blood volume flow estimation, the axial blood velocity component and vessel wall position need to be assessed accurately. In order to obtain an accurate estimation of velocity by means of Doppler ultrasound (Section 1.2), the insonation angle  $\alpha$  should be constant and accurately known, small deviations already result in large velocity errors (Fillinger and Schwartz, 1993; Gill, 1985): for an angle of about  $60^\circ$ , which is often applied in clinical practice, an error of 10% in the insonation angle results in an error of approximately 20% in the velocity estimate. Additionally, due to the non-perpendicular orientation, Doppler ultrasound does not allow to accurately estimate the position of the vessel wall and to accurately estimate velocity close to the vessel wall. There, the velocity estimation deteriorates since the wall reflection has a significant contribution in sample volumes recorded there (Figure 1.5).

Volume flow can be estimated either by directly integrating the measured velocity profile or by assuming a specific velocity distribution based on the centreline or maximum velocity. In clinical practice, often a Poiseuille or Womersley profile is assumed and the flow is calculated based on the maximum of centreline velocity (Douchette et al., 1992) since an accurate velocity estimation close to vessel walls is not feasible. The Poiseuille approximation is suitable for quasi-static flow in straight arteries, whereas the Womersley approximation is valid for in-stationary flow in straight arteries.

However, most arteries are tapered, curved and bifurcating, causing the axial velocity distribution to be altered by transversal velocities, resulting in asymmetrical axial velocity profiles and consequently in inaccurate flow estimations (Krams et al., 2005). Because of this, accurate flow estimation based on assumed velocity distributions is not feasible in-vivo. For accurate flow estimation, an improved integration method is required which enables flow estimation based on assessed asymmetric axial velocity profiles. This requires accurate velocity estimation close to the wall, so again, a perpendicular angle between ultrasound

beam and vessel is preferred.

Several blood velocity measurement techniques have been introduced to overcome the angle dependency of Doppler ultrasound. Vector Doppler methods employ two ultrasound beams, angled with respect to each other, to assess the 2D velocity. (Fox, 1978; Overbeck et al., 1992). The drawback of these methods is that for increasing distance, deviation and bias in the velocity estimate increases. Additionally, the inability to accurately measure velocity close to the vessel wall is not overcome. Ultrasound speckle velocimetry (USV) allow flow imaging with high spatial resolution and negligible angle dependency (Bohs et al., 1993, 1995; Sandrin et al., 2001; Trahey et al., 1987) by analysing the acoustic speckle pattern of the flow field. However, for an accurate, low noise velocity assessment, this technique requires specially modified ultrasound systems, custom scanning sequences and custom-developed ultrasound transducers (Bohs et al., 2000; Sandrin et al., 2001). To induce a large amount of scattering, high concentrations of scattering particles are applied. However, due to the requirement of very high particle concentrations (Kim et al., 2004a), the application of USV for in-vivo applications is limited. Additionally, the presence of velocity gradients seriously affects the performance of the PIV algorithms (Adrian, 1991) applied in USV. Jensen and Munk (1998) introduced the transverse oscillation (TO) method, which is based on the principle of applying a transverse spatial modulation to enable the assessment of motion transverse to the ultrasound beam. Both experiments in a experimental setup and in-vivo (Udesen and Jensen, 2003, 2004) have shown that the TO method allows an accurate assessment of blood velocity for transverse flow. To date only experimental ultrasound systems are used to implement the TO method. This method may have the potential of being implemented in a commercial scanner for realtime estimation. Recently, Particle Image Velocimetry (PIV) techniques (Adrian, 2005) were applied to ultrasound data, to estimate 2D velocity (Kim et al., 2004a,b; Liu et al., 2008). Promising results were obtained for velocity field measurements of flows in a phantom setup seeded with Ultrasound Contrast Agent (UCA). PIV based velocity assessment methods have the potential to allow direct volume flow estimation based on the measured velocity profile.

Local pressure estimates can be applied for impedance analysis and to convert parameters such as vessel wall diameter and vessel wall thickness into relevant biomechanical properties, such as elastic modulus (Reneman and Hoeks, 2000), distensibility and compliance of the vessel wall (Meinders et al., 2000). Various methods have been developed which enable local pressure estimation at sites in the vascular system where a direct non-invasive assessment, for example in the carotid artery, is not possible. Pressure waveforms assessed elsewhere (e.g. in the radial or digital artery) can be applied as a substitute for the local pressure, however, this offers a poor approximation since the pressure waveform changes with the location in the arterial tree (McDonald, 1974). Additionally, due to the assessment at two locations, phase errors are introduced (Hoeks et al., 2000). It has been suggested to use a transfer function to derive the central pressure from a peripheral one (Chen et al., 1997), which can be assessed non-invasively,

for example the radial pressure, estimated by means of tonometry. Although the use of transfer functions was proven to be successful (O'Rourke, 1999; Milasseau et al., 2000), it has the inherent problem that vascular parameters of individuals should match that of a reference population (Hoeks et al., 2003). Additionally, the phase difference between diameter and pressure still remains.

Deriving the blood pressure waveform from the diameter waveform circumvents the introduction of possible phase differences and avoids the use of a generalized transfer function (Meinders and Hoeks, 2004). Various methods were developed to estimate the local pressure from the diameter waveform. By simply calibrating the mean and minimum arterial diameter to mean arterial and diastolic pressure, errors in pulse pressure of only 1.6 mmHg were reported (van Bortel et al., 2001). A more realistic exponential relationship between the arterial cross section and pressure (van Loon et al., 1977; Hayashi et al., 1980; Powalowski and Pensko, 1988) can be assumed (Meinders and Hoeks, 2004). However, for these methods still a reference pressure input is required. A promising method to estimate local pressure is by simultaneous assessment of PWV and diameter waveform. The stiffness of the artery is determined from a PWV measurement, which combined with the diameter waveform can be applied to estimate the local pressure.

## 1.4 Aim and outline

### 1.4.1 Aim

The aim of this thesis is to develop and validate a method which enables a simultaneous and accurate estimation of volume flow and local pressure by means of non-invasive ultrasound. The development of the flow and pressure estimation methods is conducted in a phantom setup, which, contrary to in-vivo, allows to perform well-defined experiments, facilitating comparison with analytical approximations and CFD computations, and enables comparison with reference measurement techniques. In-vivo application of the developed methods is outside of the scope of this thesis.

### 1.4.2 Outline

Computational fluid dynamics (CFD) models can be applied as a tool to validate novel velocity (flow) and pressure estimation methods. Chapter 2 focusses on CFD models which enable an accurate estimation of local velocity components and pressure distribution in compliant geometries. Current weak coupling methods for fluid structure interaction (FSI) are compared and a dedicated coupling method appropriate for pressure and flow waves in large arteries is introduced. In Chapter 3, an ultrasound velocity estimation technique is introduced which allows the estimation of velocity components perpendicularly to the ultrasound

beam, using a commercially available ultrasound scanner equipped with a linear array probe. This enables the simultaneous measurement of axial blood velocity and vessel wall position, rendering a viable and accurate flow assessment. The measurement technique is validated by comparing axial velocity profile measurements performed in a phantom setup to analytical and CFD calculations. Physiologically relevant flows in a straight vessel are considered.

In-vivo most arteries are curved and bifurcating, which causes the axial velocity distribution to be altered by transversal velocities, resulting in asymmetrical axial velocity profiles. Novel integration methods are required to estimate the volume flow from the asymmetric axial velocity profile. Chapter 4 concentrates on the assessment of blood volume flow through a curved tube from the asymmetric axial velocity profile. Analytical approximation methods for steady flow in curved tubes are investigated. From the results, a novel volume flow estimation method, the  $\cos\theta$ -method, is derived, which is subsequently validated and compared to the presently applied Poiseuille method by means of a CFD model.

In Chapter 5, the previously introduced ultrasound velocity assessment technique (Chapter 3) is applied to both stationary and non-stationary non-Newtonian flow in a planar curved geometry in a phantom setup. The axial velocity profile measurements are compared to CFD calculations in order to estimate the performance of the velocity assessment technique in the presence of the high spatial and temporal velocity gradients, characteristic for flow in curved geometries. Subsequently, the  $\cos\theta$ -method is applied to estimate the flow from the asymmetric axial velocity profiles. The results are compared to flow estimations obtained by means of the presently applied Poiseuille and Womersley approximations.

Besides an accurate flow assessment, also an accurate simultaneous pressure assessment is required to estimate biomechanical parameters such as compliance and vascular impedance. Chapter 6, focusses on the estimation of local pressure by means of non-invasive ultrasound. Local pressure is estimated from a simultaneous assessment of local pulse wave velocity (PWV) and vessel diameter. Several methods to estimate PWV from ultrasound derived parameters are applied to measurements performed in a phantom setup. Results are compared with reference measurements of both PWV and local pressure.

Finally, a general discussion and conclusion is presented in chapter 7.

## Chapter 2

# A time-periodic approach for fluid structure interaction in distensible vessels

---

This chapter is based on: B. W. A. M. M. Beulen, M. C. M. Rutten, F. N. van de Vosse (2009). A time-periodic approach for fluid structure interaction in distensible vessels *Journal of Fluids and Structures*, doi:10.1016/j.jfluidstructs.2009.03.002

## 2.1 Introduction

Computational fluid dynamics (CFD) is a valuable tool for gaining insight into the hemodynamics of the vascular system.

CFD models can be used to investigate the relationship between local hemodynamics and vascular (dys) function (Taylor et al., 1996), but can also be applied for improvement and validation of clinical measurement methods (Wolters et al., 2005).

In compliant complex geometries, 3D fluid-structure-interaction (FSI) may provide accurate descriptions of deformation and flow phenomena. However, such models are costly in terms of computer time and resources. Consequently, 3D computational methods are mostly applied to small segments of the arterial system (Taylor et al., 1998; Gijsen et al., 1999a,b; van de Vosse et al., 2003). The effects of the distal and proximal part of the section then need to be incorporated by means of proper boundary conditions, e.g., formulated in ordinary differential equations of lesser geometrical scale, as in wave propagation (1D) or lumped parameter (0D) models. So, generally, the modelling of the fluid-structure interaction of blood flow in arteries requires the combination of different types of models (Formaggia et al., 1999, 2001; Quarteroni and Veneziani, 2003; Fernandez et al., 2005), each with their own spatial dimensions (Figure 2.1).

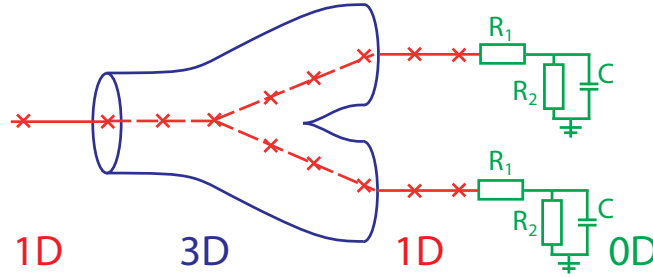


Figure 2.1: Schematic representation of a geometric multi scale model

Lumped parameter models, such as the Windkessel model, relate pressure to flow:  $p(t) = p(q(t))$ . A combination of lumped parameter models and 1D wave propagation models may be applied for the global representation of the circulatory system (Olufsen et al., 2000). Wave propagation models are often applied to describe the propagation of pressure and flow waves through large sections of the arterial system (Hughes and Lubliner, 1973; Olufsen et al., 2000), requiring a significantly smaller amount of computing resources than 3D FSI models. These models can be utilised to provide the 2D/3D models with boundary conditions, either at the inlet or outlet (Vignon-Clementel et al., 2006), but also on a larger section of the model (Reuderink et al., 1993).

Mathematically, FSI models are based on the 3D Navier-Stokes equations, de-

scribing the fluid motion, and the equations of motion for solids describing the vessel wall (structure) motion and deformation. A coupling has to be implemented between the fluid problem and the solid problem by means of dynamic and kinematic interface conditions. The pressure and shear load from the fluid side of the fluid-solid interface has to be in equilibrium with the traction at the boundary of the solid at the fluid-solid interface (dynamic interface condition). In addition, the velocity of the solid must equal the fluid velocity at the fluid-solid interface (kinematic interface condition)

In fully coupled solution methods, the fluid and the solid problem are solved simultaneously (de Hart et al., 2003; van Loon et al., 2004; Giannopapa, 2004). Typically, in arterial FSI problems, the eigenvalues of the system matrices associated with both problems are more than 9 orders of magnitude apart, resulting in a badly conditioned total matrix for the total system. Consequently, these methods can be computationally expensive and require large computer resources. In partitioned FSI approaches (Matthies and Steindorf, 2002), the fluid and the solid problem are solved sequentially, using standard methods for both domains. The fluid and solid problems are then coupled through the interface conditions described above.

In decoupled solution methods, the fluid and solid problem are solved independently. In the case that the wavelength of the pressure pulse travelling through the vessel is large compared to the section of interest, the pressure distribution inside the vessel may be assumed spatially constant and can be chosen equal to the prescribed outlet pressure, which e.g., can be determined from a 0D or 1D model. For arteries with a large length-to-radius ratio, this decoupled procedure may be inadequate due to a non-negligible axial pressure drop. 1D models, however, can also be applied to prescribe the pressure distribution inside the vessel (Reuderink et al., 1993). Although this approximation can be more appropriate, it becomes inaccurate in case the 1D model is incapable to adequately represent the pressure gradients due to complex flow phenomena (e.g. in complex geometries).

For arterial FSI problems, partitioned schemes are preferred. A partitioned approach is likely to be feasible because the flow induced pressure variations, being of the order  $\rho V^2$ , are an order in magnitude smaller than the amplitude of the pressure wave traveling through the arterial system. So inaccuracies in the velocity field will hardly influence the wall motion. In partitioned schemes, weakly and strongly coupled approaches exist.

In weakly coupled methods, the flow induced pressure is transferred timestep-wise to the solid as a normal stress at the fluid-solid interface. This induces the wall motion. Only one solution of the solid and fluid problem is required per time step, making it appealing in terms of computational effort. Two problems, typical for weakly coupled methods, may arise. First, in the weakly coupled approach no convergence may be achieved due to the so-called added mass effect, which amongst others has been analysed by Forster et al. (2007) and Causin et al. (2005), and is found to be dependent on the density/mass ratio between solid and fluid. However, in specific cases, it can be justified to employ a quasi-stationary approach for modeling the solid, averting convergence problems related to the

added mass effect (Section 2.2.1). A second problem that may arise is that the solution of the fluid problem is always one step behind of the solution of the solid problem. Due to the phase error between fluid and solid computation, a temporal computational instability, which cannot be avoided by refinement of the spatial and temporal discretization, can occur. For tubes with a high length-to-radius ratio this can lead to errors in the total volume of the domain considered that are of equal order as the flow flux during a single time step (Rutten, 1998), causing the method not to converge, either due to divergence of the fluid or solid computation.

In general, convergence issues in partitioned schemes can be overcome by strongly coupled methods, which apply sub-iterations and under relaxation for solution of the solid and fluid problem for each time step to converge to the solution of the fully coupled system (Fernandez et al., 2006; Fernandez and Moubachir, 2005; Deparis et al., 2006). The major drawback of these kinds of methods are non-robustness and the increasing amount of computational costs.

An alternative partitioned scheme is based on sequential coupling, as applied in the Sequentially-Coupled Arterial Fluid Structure Interaction (SCAFSI) method, which was recently introduced by Tezduyar et al. (2008a,b). Test computations performed on cerebral and abdominal aortic aneurysm geometries showed improved convergence properties, without requiring a significant increase in computational demand.

In this study, a similar time-periodic approach for weakly coupled 3D FSI is presented, which enables the modeling of time-periodic incompressible flow inside clinically relevant compliant geometries, i.e.: straight and weakly curved vessels, with a high length-to-radius ratio, and bifurcations.

The second section of this chapter starts with an overview of the equations, which describe the flow of an incompressible fluid through a compliant vessel and the deformation and motion of the vessel wall (Section 2.2.1). Next, a description of the time-periodic coupling method, as proposed in this study, is given in Section 2.2.2. The implementation of the models in the computational framework is discussed in Section 2.2.4. In Section 2.2.5, a series of simulations is presented, which is used to study the convergence properties of the time-periodic coupling method. The results of this analysis are presented in Section 2.3. Finally, two applications of FSI computations are presented in Section 2.4. The discussion and conclusions are given in Sections 2.5 and 2.6.

## 2.2 Materials and methods

### 2.2.1 The 3D model

Consider a spatial domain  $\Omega$  and its boundary  $\Gamma$  as illustrated in Figure 2.2. The spatial domain is subdivided into a fluid domain,  $\Omega_f$ , with boundary  $\Gamma_f$ , subdivided into  $\Gamma_{fi}$ ,  $\Gamma_{fo}$  and  $\Gamma_{fs}$  and a solid domain,  $\Omega_s$ , with boundary  $\Gamma_s$ ,

subdivided into  $\Gamma_{si}$ ,  $\Gamma_{so}$  and  $\Gamma_{sf} = \Gamma_{fs}$ . The boundary that separates the fluid and the solid domain is indicated by  $\Gamma_{fs}$ .

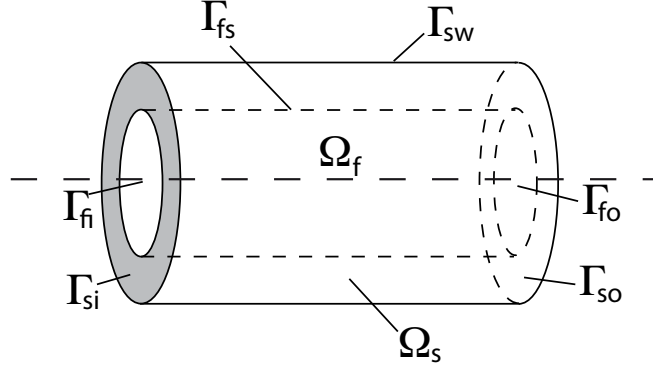


Figure 2.2: Simple compliant tube

The blood velocity and pressure distribution in the vessel are computed by solving the Navier-Stokes equations on the deforming fluid domain  $\Omega_f$  based on the arbitrary Lagrangian-Eulerian (ALE) method (Donea et al., 1982). The displacements in the vessel wall are computed by solving the equations of motion and continuity on the solid domain  $\Omega_s$ .

### Blood flow

Denoting the fluid velocity by  $\mathbf{v}(\mathbf{x}, t)$  (with  $\mathbf{x} \in \Omega_f, t > 0$ ), the pressure by  $p(\mathbf{x}, t)$  and the constant fluid density by  $\rho$ , the ALE formulation of the Navier-Stokes equation for an incompressible fluid reads:

$$\begin{aligned} \rho \frac{\partial \mathbf{v}}{\partial t} \Big|_{\Omega(t)} + \rho(\mathbf{v} - \mathbf{w}) \cdot \nabla \mathbf{v} - \nabla \cdot \boldsymbol{\sigma} - \mathbf{f} &= \mathbf{0} & \text{in } \Omega_f \\ \nabla \cdot \mathbf{v} &= 0 & \text{in } \Omega_f, \end{aligned} \quad (2.1)$$

with  $\boldsymbol{\sigma}$  the Cauchy stress tensor,  $\mathbf{w}$  the velocity of the fluid domain and  $\mathbf{f}$  the external body forces per unit of volume. In this study the body forces are assumed to be zero; influences of gravity are neglected. The time derivative is defined with respect to the moving grid. Considering blood as a Newtonian fluid, the Cauchy stress tensor is defined as

$$\boldsymbol{\sigma} = -p\mathbf{I} + 2\eta\mathbf{D}, \quad (2.2)$$

with  $p$  the fluid pressure,  $\eta$  the viscosity  $\mathbf{I}$  the identity tensor and  $\mathbf{D} = \frac{1}{2}(\nabla \mathbf{v} + (\nabla \mathbf{v})^T)$  the rate of deformation tensor.

For the boundary conditions, at the inflow boundary,  $\Gamma_{fi}$ , a Womersley velocity profile  $v_n(\mathbf{x}, t)$  corresponding to a flow  $q_i(t)$  is prescribed in normal direction. At the outflow boundary,  $\Gamma_{fo}$ , the normal stress is prescribed in terms of a given pressure,  $p_o(t)$ , and at the fluid/solid boundary a no-slip condition is prescribed, the fluid velocity is equal to the grid velocity  $\mathbf{w}$ :

$$\begin{aligned} \mathbf{v} - \mathbf{w} &= v_n(\mathbf{x}, t)\mathbf{n} && \text{on } \Gamma_{fi}, \\ \boldsymbol{\sigma} \cdot \mathbf{n} &= p_o\mathbf{n} && \text{on } \Gamma_{fo}, \\ \mathbf{v} &= \mathbf{w} && \text{on } \Gamma_{fs}, \end{aligned} \tag{2.3}$$

with  $\mathbf{n}$  the outward boundary normal. For more detailed information on the equations applied, the reader is referred to van de Vosse et al. (2003).

### Wall deformation

The displacements in the vessel wall,  $\mathbf{u}$ , are computed by solving the equations of motion (with no body forces) and continuity on the solid domain  $\Omega_s$ :

$$\rho \frac{\partial^2 \mathbf{u}}{\partial t^2} + \nabla \cdot \boldsymbol{\sigma} = \mathbf{0} \text{ in } \Omega_s, \quad \det(\mathbf{F}) - 1 = 0 \text{ in } \Omega_s, \tag{2.4}$$

with  $\boldsymbol{\sigma}$  the Cauchy stress tensor and  $\mathbf{F} = (\nabla_0 \mathbf{x}(t))^T$  the deformation gradient tensor defining the deformation between the reference state  $\Omega_0$  and the current state  $\Omega(t)$ .

The vessel wall is considered a linearly elastic neo-Hookean material for which the Cauchy stress tensor is defined by

$$\boldsymbol{\sigma} = -p\mathbf{I} + G(\mathbf{B} - \mathbf{I}), \tag{2.5}$$

with  $p$  the hydrostatic pressure,  $\mathbf{I}$  the unit tensor,  $G$  the shear modulus and the Finger tensor, defined as  $\mathbf{B} = \mathbf{F} \cdot \mathbf{F}^T$ . The shear modulus is assumed to be constant. Also other, non-linear, material behaviour can be used without loss of generality.

Under the assumption that the vessel wall thickness,  $h$ , is small compared to the vessel radius,  $a_0$ , the momentum equation in radial direction reduces to:

$$\rho h \frac{\partial^2 u_r}{\partial t^2} = p - \frac{\sigma_{\vartheta\vartheta} h}{a_0}. \quad (2.6)$$

The left hand side of equation (2.6) can be approximated by:

$$\rho h \frac{\partial^2 u_r}{\partial t^2} \approx \rho h \omega^2 u_r = \mathcal{O}(10^{-4}) \text{ Pa}. \quad (2.7)$$

For arteries, the internal pressure is typically of  $\mathcal{O}(10^4)$  Pa. Therefore the inertial term in the momentum equation (2.4) may be neglected: circumferential stresses,  $\sigma_{\vartheta\vartheta}$ , are balanced by the internal (transmural) pressure  $p$ . A quasi stationary approach is applied for modelling the solid.

At the cross-sectional surfaces at the inflow and the outflow boundaries,  $\Gamma_{si}$  and  $\Gamma_{so}$ , respectively, all displacements are constrained. At the fluid/solid boundary, the pressure and shear load from the fluid is applied as a traction boundary condition for the solid. For convenience, the shear load will be neglected in this study, since for the intended application, the influence of shear forces is negligible. So, at the fluid/solid boundary,  $\Gamma_{fs}$  the normal stress is prescribed in terms of a given pressure load,  $p_w$ . The outer wall boundary,  $\Gamma_{sw}$ , is considered stress free in normal direction:

$$\begin{aligned} \mathbf{u} &= \mathbf{0} && \text{on } \Gamma_{si} \cup \Gamma_{so}, \\ \boldsymbol{\sigma} \cdot \mathbf{n} &= -p_w \mathbf{n} && \text{in } \Gamma_{fs}, \end{aligned} \quad (2.8)$$

again, with  $\mathbf{n}$  the outward boundary normal.

### Grid motion

The velocity of the fluid mesh,  $\mathbf{w}$ , is determined by solving a linear elastic deformation of a compressible solid problem defined on the fluid domain, where the displacement of the wall is used as an essential boundary condition in  $\Gamma_{fs}$  and where the displacement in  $\Gamma_{fi}$  and  $\Gamma_{fo}$  equals zero. By choosing the finite element space for this linear elastic problem equal to the one used for the fluid solver, isoparametric elements are ensured for all timesteps.

### 2.2.2 Time periodic weak coupling

In this study, the existing decoupled and weakly coupled methods for FSI are compared to the newly introduced time-periodic coupling method.

In the time-periodic approach, the flow induced pressures are transferred time period-wise to the solid. This is allowed as long as periodic functions are applied as boundary conditions and the solution is assumed to be periodic accordingly.

The algorithm is:

Given a pressure  $p_{k-1}(\mathbf{x}, t)$  on the time interval  $[kT, (k+1)T]$ , for each time-step  $t_n$  in the time interval  $[kT, (k+1)T]$ :

1. solve the solid problem to find the displacement  $\mathbf{u}_k(\mathbf{x}, t_n) = \mathbf{u}(p_{k-1}(\mathbf{x}, t_n))$
2. calculate the grid velocity,  $\mathbf{w}_k(\mathbf{x}, t_n)$ , of the fluid domain,
3. solve the fluid problem to find the velocity,  $\mathbf{v}_k(\mathbf{x}, t_n)$ , and pressure distribution,  $p_k(\mathbf{x}, t_n)$

The algorithm continues until  $p_k(\mathbf{x}, t)$  converges to a limit function  $p(\mathbf{x}, t)$  within a predefined tolerance. The algorithm is initiated with the pressure distribution obtained from a 1D wave propagation model, which also provides the boundary conditions for the fluid problem.

For the weakly coupled method, the flow induced pressure is transferred time-step wise to the solid:  $\mathbf{u}_k(\mathbf{x}, t_n) = \mathbf{u}(p_k(\mathbf{x}, t_{n-1}))$ . Again, the boundary conditions for the fluid problem are provided by the 1D wave propagation model. For the decoupled method, not only the boundary conditions are derived from the wave propagation model, but also the axial pressure distribution which drives the wall motion:  $\mathbf{u}_k(\mathbf{x}, t_n) = \mathbf{u}(p_{1D}(x, t_n))$ .

### 2.2.3 1D model

For the 1D approximations, the time-domain based wave propagation model as introduced by Bessems et al. (2007) is applied. Contrary to present models (Stergiopoulos et al., 1999; Formaggia et al., 2001), this model allows phase differences between the boundary layer flow and the flow inside the inviscid core of the vessel. This results in proper estimates for the friction and non-linear term in the momentum balance (Bessems et al., 2007), providing an accurate description of wave propagation (Bessems et al., 2008).

At the outlets of the 1D model, three element Windkessel models, with parameters  $R_1$ ,  $R_2$  and  $C_T$  (Figure 2.1), are defined to relate the outlet pressure to outlet flow (Stergiopoulos et al., 1999). The value of the terminal resistance,  $R_1$ ,

is obtained by modeling minimal reflections at the outlets:

$$R_1 \sim Z_0 = \sqrt{\frac{L_0}{C_0}} = \sqrt{\frac{\rho h E}{2\pi^2(1-\nu^2)a_0^5}}, \quad (2.9)$$

with  $L_0 = \rho/a_0$  representing the local inertance,  $C_0$  the local compliance and  $Z_0$  the local impedance at the distal end of the vessel. The vessel wall thickness and radius are respectively indicated by  $h$  and  $a_0$ ,  $E$  is the Youngs' modulus,  $\nu$  is the Poisson ratio and  $\rho$  is the fluid density. The peripheral resistance,  $R_2$ , and the compliance,  $C_T$ , are adjusted such that pressures within the physiological range are obtained and a physiological pressure drop is achieved:

$$R_1 + R_2 = \frac{\bar{p}}{\bar{q}} \quad \text{and} \quad C_T = \tau/R_2, \quad (2.10)$$

in which  $\bar{p}$  is the desired mean pressure and  $\bar{q}$  is the mean flow prescribed at the inlet. The time constant  $\tau = 1.5$  s was found to result in a physiological pressure drop.

### 2.2.4 Implementation

The 1D wave propagation model is applied to a 1D mesh representing the centreline of the geometry considered. Locally, at a smaller section of the 1D model, a 3D computational domain is defined at which the 3D FSI model is implemented. The equations from both models are solved successively.

To solve the equations resulting from the 1D wave propagation model a spectral element method is employed, as described by Bessems et al. (2007). This results in a solution for the pressure,  $\hat{p}(\xi, t)$ , and the flow,  $\hat{q}(\xi, t)$ , in each node,  $\xi_i$ , of the 1D mesh,  $1 \leq \xi_i \leq N$ .  $N$  is the total number of nodes in the 1D mesh.

To apply the pressure distribution from the 1D model to the 3D section, the pressure at the fluid-solid interface is set equal to the pressure at the nearest point at the centreline, for each node at the fluid-solid interface. The pressure at the points at the 3D centreline is determined from the 1D solution using a linear interpolation (Figure 2.3). The linear interpolation results in  $\hat{p}(\psi_c, t)$  and  $\hat{q}(\psi_c, t)$ , on which the points at the 3D centreline are indicated by  $\psi_c = (\psi_1, \dots, \psi_M)$ . At the entrance of the 3D segment, the flow is prescribed according to  $q(\psi_{in}) = \hat{q}(\xi_{in})$ , at the exit, the normal stress is prescribed according to  $(\sigma \cdot \mathbf{n})_{out} = \hat{p}(\xi_{out})\mathbf{n}$ .

For bifurcating geometries, it is assumed that the pressure gradients within the centre section are negligibly small, such that in the centre section of the 3D

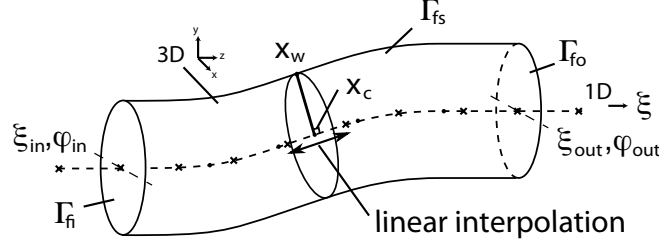


Figure 2.3: Schematic overview of the 1D and 3D domain. The  $\times$  indicates 1D nodes and the  $\bullet$  indicates 3D centreline nodes. For each node located at the fluid-solid interface, for example  $x_w$ , the nearest point located at the centreline, indicated by  $x_c$ , is determined. The pressure in  $x_w$  is set equal to the pressure in  $x_c$ , which is determined from the 1D pressure by a linear interpolation.

bifurcation, a uniform pressure, equal to the pressure in the 1D bifurcation can be prescribed.

In the 3D FSI model a first order Euler-implicit discretization scheme is used for temporal discretization of the equations presented in Section 2.2.1. The equations are consecutively linearised using the Newton-Raphson method, discretised and solved on a mesh consisting of 27-noded, isoparametric tri-quadratic Crouzeix-Raviart hexahedrons using the SEPRAN finite element package (Segal, 2004).

### 2.2.5 Convergence analysis

An idealised model of the common carotid artery (CCA) is used to study the time-periodic approach. The CCA geometry is modelled as a straight vessel with a radius of  $a_0 = 3$  mm and a wall thickness of  $h = 0.5$  mm. The value of the shear modulus  $G$  of the wall is prescribed to be 300 kPa. This value is chosen such that the maximum of the radial deformation for the physiological pressure range is approximately 5% (Milnor, 1989). For the blood flow a Newtonian fluid is used with a density of  $1.06 \cdot 10^3 \text{ kgm}^{-3}$  and a dynamic viscosity of  $4.9 \cdot 10^{-3} \text{ kgm}^{-1}\text{s}^{-1}$ .

At the inlet of the 1D model a smooth waveform resembling CCA flow is prescribed. The outlet of the 1D model is terminated by a three element Windkessel model, with parameters  $R_1 = 3.6 \cdot 10^{12} \text{ kgm}^{-4}\text{s}$ ,  $R_2 = 8.6 \cdot 10^{12} \text{ kgm}^{-4}\text{s}$  and  $C_T = 1.2 \cdot 10^{-13} \text{ m}^4\text{s}^2\text{kg}^{-1}$ . In Figure 2.4, the prescribed flow waveform and the resulting pressure waveform at the exit of the 1D model are presented.

For the input flow, with geometrical and fluid properties as shown above, the Reynolds number, defined as  $\text{Re} = \rho v a_0 / \mu$ , ranges from 100 to 800, which is in the physiological relevant range (Ku, 1983).

The geometry described above is defined at  $p = 0$  mmHg. Before the FSI calcula-

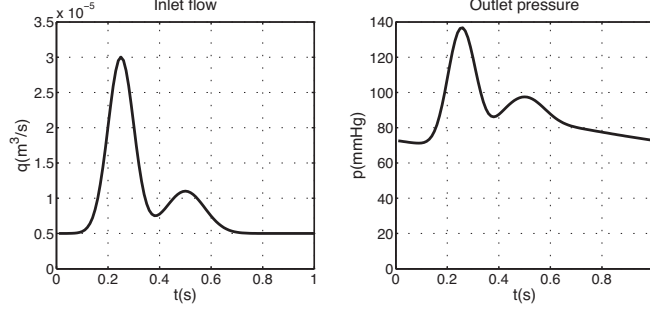


Figure 2.4: At the left, the flow waveform prescribed at the inlet of the 1D model is shown. The resulting pressure waveform at the outlet of the 1D model is shown at the right.

tions are initiated the pressure load on the wall is slowly increased toward diastolic pressure level. This prevents a sudden wall motion, due to a large pressure step, at the first time step.

To study the convergence properties of the time-periodic approach, an FSI computation has been performed for  $t \in [0, 5T]$  on a section of the CCA with a length  $L = 40a_0$ . A discrete  $L_2$ -norm is applied to determine the convergence rate:

$$\epsilon = \|\bar{p}_{n+1} - \bar{p}_n\|_2 = \sqrt{\sum_i (\bar{p}_{n+1}^i - \bar{p}_n^i)^2}, \quad (2.11)$$

in which the nodes in the fluid domain are indicated by  $i$ .  $\bar{p}_n$  is the mean value of the pressure solution from the 3D Navier-Stokes equation, during period  $n$ .

To compare the performance of the time-periodic, decoupled and weakly coupled methods, FSI computations were performed for vessel geometries with increasing length-to-radius ratio ( $L/a_0 = 10, 20, 40, 50$  and  $60$ ). Convergence of inlet pressure ( $p_i$ ) and outlet flow ( $q_o$ ) solutions of the decoupled and time-periodic method are compared by means of the discrete  $L_2$ -norm:

$$\epsilon_q = \left\| \frac{q_{o,dc} - q_{o,tp}}{q_{o,tp}} \right\|_2 \quad \text{and} \quad \epsilon_p = \left\| \frac{p_{i,dc} - p_{i,tp}}{p_{i,tp}} \right\|_2, \quad (2.12)$$

in which the subscripts  $dc$  and  $tp$  respectively indicate the decoupled and time-periodic approach.

## 2.3 Results

The result of the convergence analysis has been presented in Figure 2.5. It clearly shows a monotonic decrease of the residual  $\epsilon$  with increasing period number  $n$ . All pressure and flow solutions presented in the remainder of this study were obtained by performing computations for 5 periods (for  $n = 4$ ,  $\epsilon = \mathcal{O}(10^{-4})$ ).

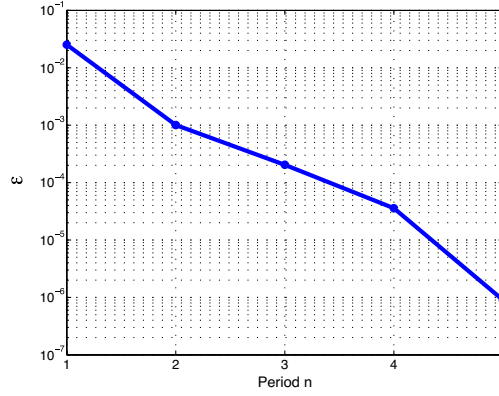


Figure 2.5: Convergence analysis applied to the pressure solution of a time-periodic FSI computation performed on a straight section of the CCA with a length  $L = 40a_0$ .

It was found that the weakly coupled approach is applicable to vessels up to  $\frac{L}{a_0} \approx 10$ , for vessels of larger length the computations diverge. The time-periodic and the decoupled methods are successfully applied to vessels up to  $\frac{L}{a_0} = 60$ . No significant differences with respect to computation time and convergence between both methods were found, which is to be expected, since for both methods equal solution methods are applied and only minor differences in prescribed boundary conditions exist.

In Figure 2.6 the results of the FSI-computations for the inlet/outlet flow and inlet/outlet pressure, for the straight section of  $L = 20a_0$  and  $L = 50a_0$  of the CCA are presented. For each calculation method, respectively, the inlet flow and the outlet pressure are equal since these are the imposed boundary conditions. Generally, for short sections ( $L = 20a_0$ ) minor differences ( $\epsilon_q = 3 \cdot 10^{-2}$ ,  $\epsilon_p = 3 \cdot 10^{-3}$ ) occur, whereas for longer sections ( $L = 50a_0$ ), more significant differences ( $\epsilon_q = 4 \cdot 10^{-1}$ ,  $\epsilon_p = 1 \cdot 10^{-1}$ ) in solution are found between the decoupled and time-periodic approach.

Deviations between 1D and 3D flow and pressure solutions are present which can be caused by the difference in solid model applied for the 1D and 3D computations. A closer analysis of the wall motion shows a maximum difference of 2% in wall distension between 1D and 3D model, which indicates that the 3D solution offers

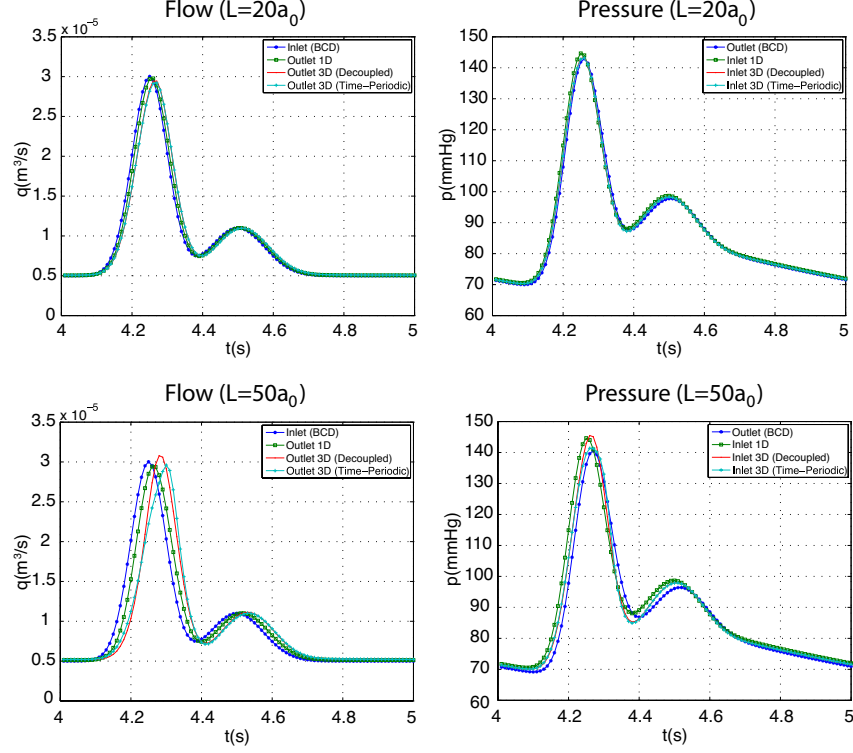


Figure 2.6: Results of the FSI-computations for the inlet/outlet flow and inlet/outlet pressure calculated by the 1D-model, the decoupled approach and the time-periodic approach for straight sections of the CCA with a length of  $L = 20a_0$  and  $L = 50a_0$ .

a sensible solution for the FSI problem.

## 2.4 Applications

In-vivo, the CCA and most other arteries are not straight, but have a significant curvature. MR and ultrasound imaging studies of CCA morphology have shown that the ratio of curvature,  $\delta$  ( $\delta = a_0/R$ ), for the CCA can range up to 3% (Tortoli et al., 2003). Fluid flowing through a curved vessel experiences a centripetal force. The fluid in the core of the tube is forced towards the outside of the bend, which results in secondary flows and thus an energy loss. Therefore, the axial pressure drop in a curved tube is larger than the pressure drop in a straight tube of equal length (Dean, 1928). Besides an axial pressure gradient, also cross-sectional pressure gradients are present: the pressure-load distribution on the vessel wall

is non-uniform due to 3D flow phenomena. Furthermore, the arterial tree is a highly bifurcating network. As in curved vessels, also in bifurcations, non-uniform pressure-load distributions occur, possibly influencing the wall motion.

For both curved and bifurcating geometries, the performance of the time-periodic coupling method is compared to the performance of the decoupled approach. For the curved geometry, a curved section of the CCA with a length of  $40a_0$  and a curvature ratio of 3% is considered (Figure 2.7). For vessel properties and boundary conditions, equal values as presented in section 2.2.5 are applied.

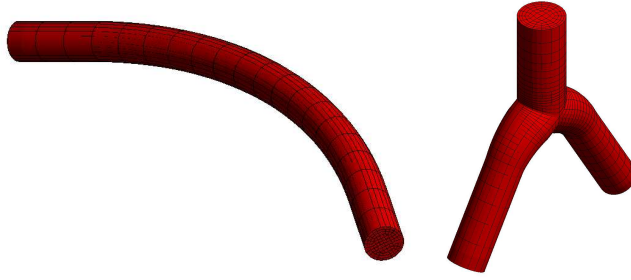


Figure 2.7: Geometry for the curved section of the CCA (left) and the Carotid bifurcation (right)

For the bifurcating geometry, the carotid bifurcation is modelled as an idealised symmetric planar bifurcation (Figure 2.7). The inlet trunk of the bifurcation has a radius of 3 mm, and a length of  $L_i = 4a_0$ . The radius of the outlet trunk is chosen such that the average shear rate at the outlet is equal to the average shear rate at the inlet, the length of the outlet trunks is equal to  $L_o = 8a_0$ . The angle between both outlet trunks is 120 degrees.

At the inlet of the 1D bifurcation model a smooth flow waveform, resembling the CCA flow is prescribed. At the outlets, the 1D model is terminated by a three element Windkessel model, with parameters  $R_1 = 6.5 \cdot 10^{12} \text{ kgm}^{-4}\text{s}$ ,  $R_2 = 8.2 \cdot 10^{11} \text{ kgm}^{-4}\text{s}$  and  $C_T = 1.8 \cdot 10^{-14} \text{ m}^4\text{s}^2\text{kg}^{-1}$  (2.9 and 2.10).

### 2.4.1 Results

The flow field in the curved vessel geometry, as calculated using the time-periodic coupling method clearly shows the development of the asymmetric axial velocity distribution and the presence of the secondary velocity field (Figure 2.8).

For the decoupled and time-periodic approach, a comparison (Figure 2.9) of the inlet/outlet flow and inlet/outlet pressure, indicates deviations between 1D and 3D flow and pressure solutions, which can be caused by the difference in the solid model applied for the 1D and 3D computations. Differences between decoupled and time-periodic coupling method are found to be  $\epsilon_q = 2 \cdot 10^{-1}$  and  $\epsilon_p = 4 \cdot 10^{-2}$ .

For the bifurcating geometry, the flow field calculated using the time-periodic coupling method is presented in Figure 2.10. In the outlet trunks, the characteristic asymmetric axial velocity distribution and secondary velocity field are clearly visible. In Figure 2.11 the results of the FSI-computations for the inlet/outlet flow and inlet/outlet pressure for the carotid bifurcation are presented. The graphs in Figure 2.11 show no significant differences between 1D and 3D, furthermore, also no significant differences ( $\epsilon_q = 5 \cdot 10^{-6}$ ,  $\epsilon_p = 7 \cdot 10^{-8}$ ) in solution arise for the decoupled and time-periodic coupling method.

## 2.5 Discussion

The weakly coupled time-periodic FSI method has been applied successfully to straight, curved and bifurcating geometries. Approximate solutions of the pressure distribution of subsequent time-periods were obtained using the pressure solution of the previous time-step as an initial condition. Contrary to most present models, 1D models were not only applied for supplying boundary conditions, but also as an approximation for the initial axial pressure distribution inside the 3D section. The convergence analysis showed good results, but since no theoretical results were available for the time-periodic approach, no comparison with literature was made. Additionally, it should be noted that the proposed algorithm is not suitable for transient analysis, since it is based on the assumption that periodic functions are applicable for the boundary conditions.

The time-periodic coupling method has been compared to the decoupled and weakly-coupled approaches. The time-periodic coupling method was found to offer an improved computational stability compared to the weakly-coupled approach. For the weak coupling method, convergence problems already arise for vessels with a length-to-radius ratio higher than 10, which for the time-periodic approach only occurs for vessels with a length-to-radius ratio above 60. These numbers (10, 60) are probably related to the wave length of the pressure wave. Decreasing the step size of the temporal discretization from 0.01 s to 0.001 s did not result in an improvement with respect to the computational stability. Since in this study, a quasi stationary approach is applied for modeling the solid, added mass instabilities are not believed to be responsible for the convergence problems in the weakly-coupled approach. More likely, phase errors in the wall motion estimate are. For vessels with a length-to-radius ratio above 60, no convergence is achieved, both for decoupled and time-periodic approaches. Additional simulations, involving only an isolated solid domain, have shown that the non-convergence is occurring in the solid calculation itself and is not a result of coupling issues. Although this non-convergence is odd, and should be solved, it is of minor relevance for this study, since for in-vivo application, the simulation of vessels with a length-to-radius ratio ranging between 10 and 50 is of interest. Due to bifurcating and tapering, straight vessels with a higher length-to-radius ratio are hardly present, therefore, we believe that the simulation of these kind of geome-

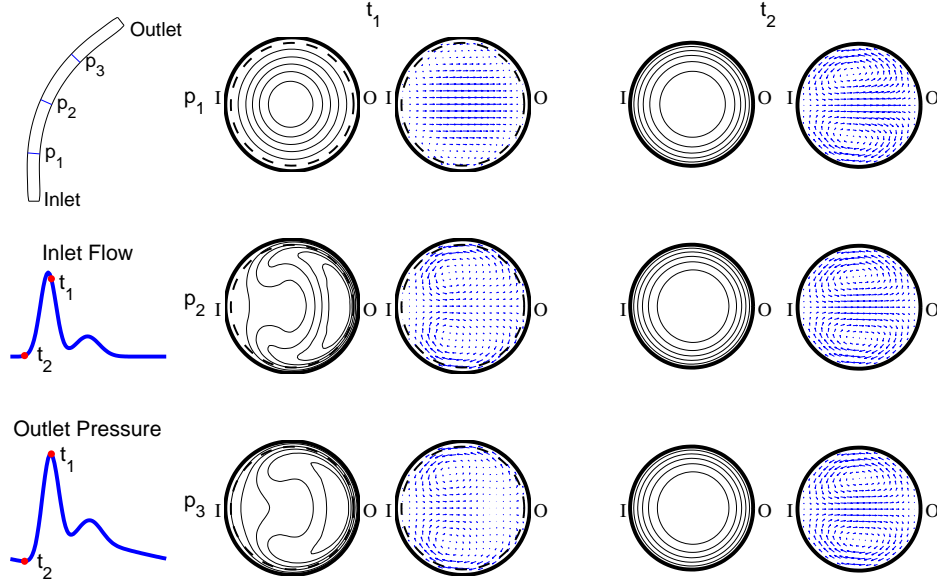


Figure 2.8: Results of the time-periodic FSI-simulation performed on the curved vessel. The flow field is visualised at three positions ( $p_1, p_2$  and  $p_3$ ) at peak systolic time  $t_1$  and end diastolic time  $t_2$ . The contour plots show the axial velocity distribution, the vector plots show the secondary velocity profiles,  $I$  denotes the inside of the bend,  $O$  denotes the outside, the dashed line indicates the position of the vessel wall at the end diastolic time.

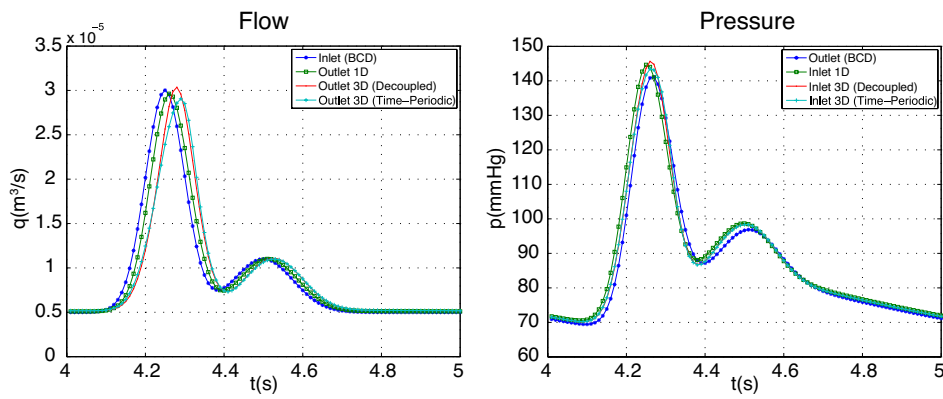


Figure 2.9: Results of the FSI-computations for the inlet/outlet flow and the inlet/outlet pressure calculated by the 1D-model, the decoupled approach and the time-periodic approach for the curved section of the CCA.

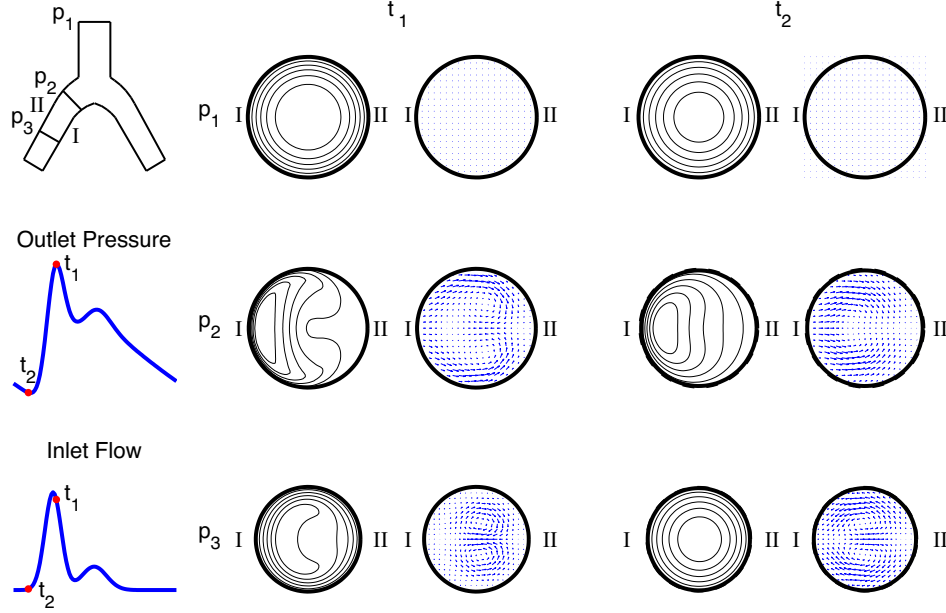


Figure 2.10: Results of the time-periodic FSI-simulation performed on the bifurcation. The flow field is visualised at three positions ( $p_1, p_2$  and  $p_3$ ) at peak systolic time  $t_1$  and end diastolic time  $t_2$ . The contour plots show the axial velocity distribution, the vector plots show the secondary velocity profiles,  $I$  and  $II$  indicate the orientation of the plane with respect to the bifurcation.

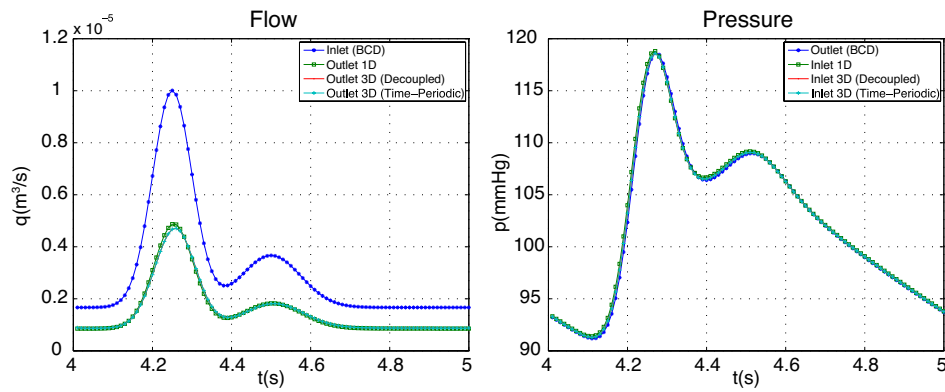


Figure 2.11: Results of the FSI-computations for the inlet/outlet flow and the inlet/outlet pressure calculated by the 1D-model, the decoupled approach and the time-periodic approach for the bifurcation geometry.

tries is not very relevant.

Both the decoupled and time-periodic coupled methods are successfully applied to geometries with a high length-to-radius ratio. The computations show that differences in solution between decoupled and time-periodic approach increase for geometries with increasing length-to-radius ratio. The differences are probably caused by the fact that for 1D and 3D models different material properties and geometry are applied for calculating the wall motion, resulting in differences in wall distension. This will have the most notable effects in vessels of high length-to-radius ratio.

For high length-to-radius geometries, the SCAFSI method, as introduced by Tezduyar et al. (2008a,b), probably also improves convergence properties, since the proposed time-periodic method and the SCAFSI method are similar. Common step in both methods is that for the initial iteration, the wall motion is driven by a reference pressure signal. However, in the SCAFSI algorithm, this reference pressure is assumed spatially constant, whereas in the time-periodic approach, the reference pressure is determined from a 1D wave propagation model. The 1D pressure distribution is a more accurate approximation for the pressure distribution inside 3D geometries than a constant pressure, especially for geometries with a high length/radius ratio. Test computations performed using the SCAFSI method on cerebral and abdominal aortic aneurysm geometries show improved convergence properties, without requiring a significant increase in computational demand (Tezduyar et al., 2008b). However, no results are shown for geometries with a high length-to-radius ratio, which is the focus of this study.

For the FSI-computations performed on the bifurcating geometry, no significant differences arise for the different coupling methods, which indicates that the change of pressure distribution on the vessel wall due to the 3D flow phenomena is too small to significantly influence the vessel wall motion. Also for the curved vessel, the differences observed are probably more a result of the high length-to-radius ratio, than of the 3D flow phenomena due to the curvature. Consequently, it can be concluded that the advantage of the time-periodic coupling method with respect to the decoupled method will primarily show for geometries with a high length-to-radius ratio.

## 2.6 Conclusion

The time-periodic weakly coupled method presented in this study enables the modeling of FSI in long compliant vessels. This is a problem for weakly coupled methods based on timestep-wise coupling. Flow through straight compliant vessels with a length up to 60 times the radius is modelled successfully, whereas weakly coupled methods based on timestep-wise coupling only permit a length-to-radius ratio of 10. The simulations presented in this study show that the time-periodic method can be a valuable tool in the simulation of blood flow in arteries.

## Chapter 3

# Perpendicular ultrasound velocity measurement by 2D cross correlation of RF data: experiments and validation

---

The contents of this chapter have been submitted for publication: B. W. A. M. M. Beulen, M. C. M. Rutten, P. J. Brands, F. N. van de Vosse. Perpendicular ultrasound velocity measurement by 2D cross correlation of RF data: experiments and validation. *Experiments in Fluids*, submitted (2009)

### 3.1 Introduction

Haemodynamic factors, such as blood flow and pressure, play a significant role in cardiovascular (dys)function. For example, blood flow regulates the lumen diameter, whereas intraluminal pressure regulates the wall thickness (Fung, 1993). Furthermore, the blood velocity distribution close to the vessel wall is an important factor in the development and localization of atherosclerosis (Caro et al., 1971).

In clinical practice, ultrasound is often used as a non-invasive method to assess (centreline) blood velocity and vessel wall motion (Brands et al., 1999). Doppler ultrasound allows the measurement of the component of the blood velocity along the ultrasound beam at a high temporal resolution. To assess the axial blood velocity component, the ultrasound beam has to be positioned at an angle with respect to the blood velocity vector. For a reliable velocity assessment it is necessary that this angle is accurately known. Small deviations already result in large velocity errors (Fillinger and Schwartz, 1993; Gill, 1985).

To relate the (centreline) velocity measurement to volume flow, assumptions have to be made on the axial velocity distribution across the vessel. In addition, the position of the vessel walls needs to be accurately known in order to perform the integration from velocity to flow and to determine the vessel diameter. The position of the vessel walls can only be assessed accurately with the ultrasound beam in perpendicular orientation with respect to the vessel. This renders a simultaneous measurement of velocity by Doppler ultrasound and wall position impossible, and thus hampers an accurate flow assessment.

Several blood velocity measurement techniques based on ultrasound have been reported to overcome the angle dependency of Doppler ultrasound and to allow 2D velocity estimation.

Vector Doppler methods were introduced, in which ultrasound beams, positioned at an angle with respect to each other, were applied to assess the 2D velocity, either using a single (Fox, 1978) or two (Overbeck et al., 1992) transducers. The drawback of these methods is that the angle between the beams decreases with depth, resulting in an increasing standard deviation and bias in the velocity estimates.

Ultrasound speckle velocimetry (USV), allows flow imaging with a high spatial resolution and a negligible angle dependency (Bohs et al., 1993, 1995; Sandrin et al., 2001; Trahey et al., 1987). The USV technique enables assessment of 2D velocity vectors by analyzing the acoustic speckle pattern of the flow field. However, for an accurate, low noise velocity assessment, this technique requires specially modified ultrasound systems, custom scanning sequences and custom-developed ultrasound transducers (Bohs et al., 2000; Sandrin et al., 2001). To induce a large amount of scattering, high concentrations of scattering particles are applied. However, due to the requirement of very high particle concentrations (Kim et al., 2004a), the application of USV for in-vivo applications is limited. Additionally, the presence of velocity gradients seriously affects the USV performance (Adrian, 1991).

Jensen and Munk (1998) introduced the transverse oscillation (TO) method,

which is based on the principle of applying a transverse spatial modulation to enable the assessment of motion transversely to the ultrasound beam. Both experiments in a phantom setup and in-vivo (Udesen and Jensen, 2003, 2004) have shown that the TO method allows an accurate assessment of blood velocity for transverse flow. Although at this point, experimental ultrasound systems are used to implement the TO method, it may have the potential of being implemented in a commercial scanner for real time estimation.

The application of Particle Image Velocimetry (PIV) techniques (Adrian, 2005) to ultrasound was first reported by Crapper et al. (2000). PIV algorithms were applied to B-mode video images of a sediment-laden flow, resulting in estimated velocities up to  $6 \text{ cm s}^{-1}$ . Kim et al. (2004a,b) introduced Echo PIV: advanced PIV algorithms were applied on second harmonic images enhanced by an Ultrasound Contrast Agent, generated by a commercially available ultrasound scanner equipped with a phased array sensor transducer. This allowed the assessment of the 2D velocity field, with a spatial resolution of  $1.2(r) \times 1.7(\theta) \text{ mm}$  at the image centre. For stationary flow a dynamic range of 1 to  $60 \text{ cm s}^{-1}$  was reported, obtained at a temporal resolution of 3.8 ms. For pulsating flow, 18 cycles were ensemble averaged to obtain axial velocity profiles with a peak velocity up to  $50 \text{ cm s}^{-1}$  at a temporal resolution of 2 ms. Liu et al. (2008) developed a custom-designed ultrasound system equipped with a linear array probe to ensure a more uniform resolution compared to the phased array transducer. The custom designed system allowed flexible control of the Echo PIV parameters. A comparison between Doppler and echo PIV-based measured peak velocity on high speed non-laminar flow up to  $140 \text{ cm s}^{-1}$  showed a maximum deviation of 6.6 %. For the measured flow rates, echo PIV imaging parameters such as frame rate, beam line density and spatial resolution were adjusted such that the maximum velocity was accurately captured.

In this study an ultrasound velocity assessment technique similar to echo PIV is applied, which focusses on the assessment of the velocity component perpendicular to the ultrasound beam. This enables a simultaneous assessment of both axial velocity profile and vessel wall position at high temporal and radial resolution, thus enabling a more accurate flow assessment. Contrary to the above summarized velocity assessment techniques, a standard linear array transducer, connected to a commercially available, clinically approved ultrasound system equipped with RF-data output and acquisition system is applied for the velocity estimation. The linear array probe is positioned perpendicular to the vessel. The ultrasound system is operated in fast B-mode (high frame rate B-mode). The axial velocity is assessed by applying PIV based analysis techniques to the raw B-mode RF data. The position of the wall can be determined from the radio frequency (RF) ultrasound data (Brands et al., 1999), allowing an accurate integration of velocity to flow. The pressure inside the vessel can be estimated from the wall distension and pulse wave velocity, which both can be determined from the perpendicularly acquired fast B-mode data (Hermeling et al., 2007). This enables a simultaneous assessment of local pressure and flow, which can be applied to characterize the global conditions of the vascular tree (Brands et al., 1996).

The aim of this study is develop and validate a velocity measurement technique.

The validation is performed by comparing velocity measurements in a phantom setup to analytic and Computational Fluid Dynamics (CFD) calculations. In the phantom setup, stationary flow and a physiologically relevant pulsatile flow are generated, using a blood analog fluid which mimicks both the acoustical and mechanical properties of blood.

An overview of the phantom setup, blood mimicking fluid, data acquisition, data processing and a description of the validation experiments is given in the materials and methods section. Next, the results of the validation experiments are presented in the results section. The study is completed with the discussion and conclusion sections.

## 3.2 Materials and methods

### 3.2.1 Phantom setup

In the phantom setup (Figure 3.1), a fluid, mimicking the acoustic and rheological properties of blood, is pumped from a reservoir through a compliant tube, which mimics the blood vessel. A polyurethane tube (HemoLab, Eindhoven, The Netherlands) with a length of about 1.5 m, a radius of 4 mm and a wall thickness of 0.1 mm is applied to mimic the common carotid artery (CCA). The tube is fully submerged in a reservoir of water to prevent deformation under influence of gravity. Additionally, the water acts as an excellent conductor of sound. The tube is terminated by an impedance from which the fluid flows back, through a reservoir, to the inlet of the pump. For the terminal impedance, a Windkessel model is applied. The viscous dissipation in the distal vessel,  $R$ , and the viscous dissipation in the distal capillary bed  $R_p$ , are modelled by local narrowing, the compliance of the arterial system,  $C$ , is modelled by an air-chamber.

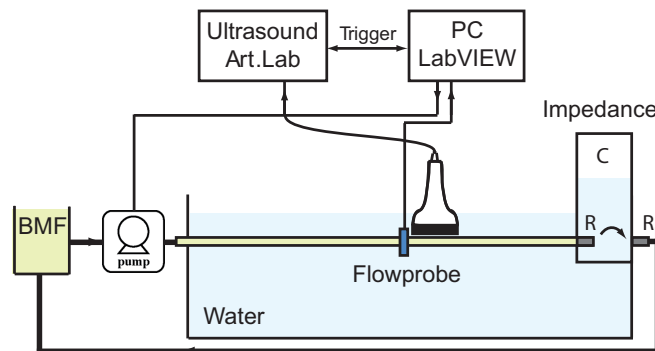


Figure 3.1: Schematic overview of the experimental setup.

The flow is generated by combining a stationary pump and a servo-actuator

operated piston pump (indicated in Figure 3.1 by a single symbol). The stationary pump (Pacific Scientific, IL, USA) is manually set to a specific flow rate, whereas the trajectory of the piston pump (home developed) is computer controlled with LabVIEW software (National Instruments, Austin, TX, USA). The ultrasound probe is placed far (approximately 1 m) from the inlet of the polyurethane tube to ensure development of laminar flow at the measurement site. The probe is accurately positioned perpendicularly to the vessel, by means of a 3D manipulator, such that the mechanical focus of the probe is located at the centre of the vessel. To maximize the signal level, the electrical focus is set equal to the mechanical focus. At about 1 cm upstream of the ultrasonic probe a flow probe (Transonic, 10PAA) is positioned to measure the flow through the vessel. The data from the flow probe measurements is acquired simultaneously with the data from the ultrasound scanner using a common trigger signal generated by a PC using the same LabView software.

### 3.2.2 Blood mimicking fluid

Blood is a non-Newtonian fluid with shear thinning properties: for high shear rates, the viscosity decreases. A shear thinning Blood Mimicking Fluid (BMF), with both acoustical and mechanical properties similar to blood has been developed.

The BMF consists of Xanthan gum (Fluka, 95465),  $0.5 \text{ g l}^{-1}$  dissolved in water (97.3% weight) with 1.8% weight Orgasol particles and 0.9% weight Synperonic NP10 added. Xanthan gum is used to mimic the mechanical behaviour of blood (Brookshier and Tarbell, 1993; van den Broek et al., 2008). Ultrafine polyamide particles (2001UDNAT1, Orgasol, ELF Atochem, Paris, France) with a diameter of  $5 \cdot 10^{-6} \text{ m}$  are used as ultrasound scattering particles. The polyamide particles have a specific density of  $1.03 \text{ g cm}^{-3}$ . The concentration of the particles used results in a blood-similar backscattering of ultrasound waves (Ramnarine et al., 1998). Synperonic NP10 (Fluka 86208) acts as a surfactant to prevent coagulation of the scattering particles.

In general, scattering particles used in BMF are chosen to be naturally buoyant (Ramnarine et al., 1998) with respect to the fluid base. This implies an accurate control of the fluid density to prevent the particles to sediment or float. The shear thinning properties of the developed BMF reduces sedimentation and floating of particles since slow moving particles experience a relatively high drag force, due to high viscosity at low shear. This facilitates the application of the BMF in the phantom setup.

The velocity distribution across the vessel cannot be described by Poiseuille (stationary flow) or Womersley (non-stationary flow) theory, since these were derived for Newtonian fluids. Mathematically, the BMF can be modelled as a generalized, non-Newtonian shear thinning liquid. Application of a power law model (Bird, 1987) enables an analytic approach for calculating the velocity distribution. The

power law model is given by

$$\eta = \eta_0(\lambda\dot{\gamma})^{n-1}, \quad (3.1)$$

with  $\eta_0$  the viscosity at  $\dot{\gamma} = 1/\lambda$ , a time constant  $\lambda$  and  $n$  the power-law constant. The power-law model can only be applied to describe the viscosity at intermediate shear rates, since very low and very high shear rates result in physically unrealistic values for the viscosity.

Assuming that the non-Newtonian properties of a fully developed, stationary flow can be characterized by a power-law model at characteristic shear rate, the velocity distribution for fully developed flow in a straight circular tube is given by (Bird, 1987):

$$v(r) = \frac{Q}{\pi a^2} \frac{1}{\frac{1}{2} - \frac{1}{1/n+3}} \left(1 - \left(\frac{r}{a}\right)^{\frac{1}{n}+1}\right), \quad (3.2)$$

in which  $n = n(\dot{\gamma}_{char})$ . The characteristic shear rate  $\dot{\gamma}_{char}$  is defined as (Gijzen et al., 1999b):

$$\dot{\gamma}_{char} = \frac{2Q}{\pi a^3}, \quad (3.3)$$

in which  $Q$  is volume flow rate through the vessel and  $a$ , the radius of the vessel. Consequently, for shear thinning fluids, this results in velocity profiles that are flattened ( $n < 1$ ) compared to the Poiseuille profiles for Newtonian flow ( $n = 1$ ).

A more realistic viscosity model, which can be applied in CFD analysis, is given by the Carreau-Yasuda model (Bird, 1987):

$$\frac{\eta - \eta_\infty}{\eta_0 - \eta_\infty} = [1 + (\lambda\dot{\gamma})^b]^{(n-1)/b}, \quad (3.4)$$

with  $\eta_0$  the viscosity at low shear rate,  $\eta_\infty$  the viscosity at high shear rate,  $\lambda$  a time constant and  $n$  the power-law constant. The parameter  $b$  determines the transition between the low-shear-rate region and the power-law region.

### 3.2.3 Data acquisition

The commercially available Picus Art.Lab ultrasound system (ESAOTE Europe, Maastricht, The Netherlands) is used to collect the raw RF-data for offline processing. The system is equipped with a 7.5 MHz linear array transducer of 40

mm, consisting of 128 transducer elements. The RF data are sampled at 33 MHz ( $f_s$ ) and have an approximate centre frequency of 6.8 MHz and a quality factor of 2.

For the PIV measurements, the ultrasound system is operated in fast B-mode (high frame rate B-mode), also called multiple M-line mode. Each frame is composed of 14 adjacent M-mode lines generated at a pitch of 0.3125 mm. To maximize the signal level at the focal point, the electrical focus is set equal to the mechanical focus, which is fixed at 2 cm from the transducer surface. The frame rate of the ultrasound system is determined by the number of M-lines and the pulse repetition frequency ( $f_{pr}$ ), the frequency at which individual M-mode lines are acquired, which depends on the maximum depth setting of the ultrasound system. For the PIV measurements the depth is set to 50 mm, which results in a frame rate,  $f$ , of 730 s<sup>-1</sup>. The maximum measurement time is hardware limited to about 3.8 seconds. The RF data matrix obtained from the system is a 3D function of depth ( $r$ ), time ( $t$ ) and position along the probe ( $z$ ) (Figure 3.3).

### 3.2.4 Data processing

The RF data were processed on a PC using Matlab (The MathWorks, Natick, MA, USA). After removal of the DC component of the RF signals, a 4th order Butterworth band pass filter (4.2 MHz and 12.5 MHz) is applied. A 4th order Butterworth high pass filter with a cutoff frequency of 20 Hz is applied in the temporal direction to suppress static and slow moving objects (e.g. wall reverberations).

A cross-correlation based technique similar as in PIV (Adrian, 2005) is applied to determine the axial velocity distribution of the flow through the tube. In optical PIV, the spatial resolution is determined by the number of pixels in the image sensor in combination with the interrogation area size. In the case of a square data area this results in an equal resolution for both spatial directions. For the ultrasound data, the field of view (FOV) is rectangularly shaped (Figure 3.2). The width of the FOV is determined by the transducer element width,  $W_{el}$ , which is equal to  $0.315 \cdot 10^{-3}$  m, and the number of active transducer elements. For 14 active elements and an imaging depth set to 50 mm this results in a FOV of  $4.4 \times 50.0$  mm.

The spatial resolution along the ultrasound beam, determined by the ultrasound wavelength, is much higher than the resolution in perpendicular direction, which depends on the overall size of the aperture. Because of this, data windows of 8 samples (0.2 mm) in radial direction and 14 samples (4.4 mm) in axial direction are applied to the RF-data. The axially stretched data windows are consistent with the objective to accurately assess axial velocity profile and flow through vessels: the small radial dimension of the data window allows the estimation of axial velocity in the presence of large radial gradients, additionally, the axial gradients in axial velocity are presumed to be small compared to the radial gradients,

justifying the large axial dimension of the data window.

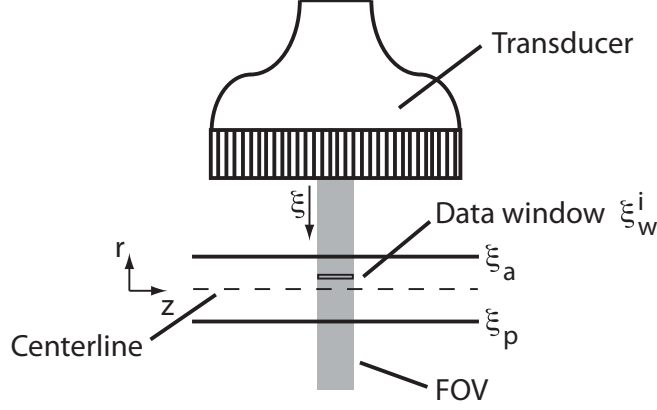


Figure 3.2: Schematic overview of the FOV, the data windows etc.

After identification of the anterior ( $\xi_a$ ) and posterior wall position ( $\xi_p$ ) by means of a sustain attack filter (Meinders et al., 2001), 50% overlapping data windows are applied to the lumen of the vessel. Positions along the coordinate axis  $\xi$  are expressed in ultrasound sample points. The data windows are indicated by their respective centre coordinate  $\xi_w^i$ , in which  $1 \leq i \leq N$ , with  $N$  the total number of applied data windows in a single frame. The position of the data windows, expressed in meters,  $r_w^i$ , with respect to the centreline is given by

$$r_w^i = \frac{2c}{f_s} \left[ \xi_w^i - \frac{\xi_p + \xi_a}{2} \right], \quad (3.5)$$

in which  $c$  is the velocity of sound for the BMF and  $f_s$  the ultrasound sampling frequency. The vessel radius is determined by

$$a = \frac{c}{f_s} (\xi_p - \xi_a). \quad (3.6)$$

Like in optical PIV analysis, for each data window in the acquired frames, the shift between two corresponding data windows from subsequent frames is calculated by performing a 2D cross correlation in the time domain on the raw RF data and determination of the peak position in the cross correlation plane (Figure 3.3).

The position of the peak,  $\delta \hat{\mathbf{x}}(r_w^i) = (\delta \hat{\xi}(r_w^i), \delta \hat{z}(r_w^i))$ , is determined by finding the location of the maximum in the correlation plane after application of a Hilbert transformation, which is applied to calculate the envelope. According to the

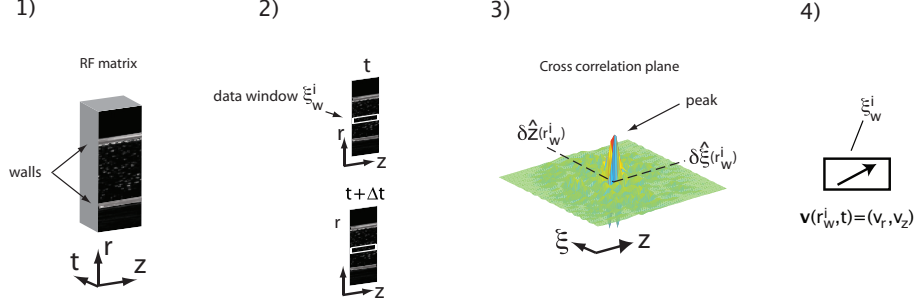


Figure 3.3: Schematic overview of the velocity estimation algorithm. For all frames in the RF matrix (1), data windows,  $\xi_w^i$ , are applied. For each pair of corresponding data window in subsequent frames (2) a cross correlation is performed. The shift between the data windows is estimated by detecting the peak position,  $\delta\hat{\mathbf{x}}(r_w^i) = (\delta\hat{\xi}(r_w^i), \delta\hat{z}(r_w^i))$ , in the cross correlation plane (3) and subsequently performing the peak fit. By incorporating the time difference between subsequent frames, the average velocity,  $\mathbf{v}(r_w^i, t)$ , of the fluid corresponding to the data window (4) is determined from the estimated shift.

central limit theory (Evans et al., 2000), the backscattered echo is Gaussian distributed since it is composed of signal contributions due to many independent scatters (Cloutier et al., 2004). Consequently, to gather sub-pixel information for the peak position, a three point Gaussian-fit estimator (Westerweel, 1993) is applied for determining the fractional displacement  $\epsilon(r_w^i) = (\epsilon_\xi(r_w^i), \epsilon_z(r_w^i))$ :

$$\epsilon_\psi(r_w^i) = \frac{\ln(\delta\hat{\psi}(r_w^i) - 1) - \ln(\delta\hat{\psi}(r_w^i) + 1)}{2[\ln(\delta\hat{\psi}(r_w^i) - 1) + \ln(\delta\hat{\psi}(r_w^i) + 1) - 2\ln(\delta\hat{\psi}(r_w^i))]} \quad \text{for } \psi = \xi, z. \quad (3.7)$$

For each data window, this results in the sub-pixel peak position, with respect to the centre of the cross correlation plane,  $\delta\mathbf{x}(r_w^i) = \delta\hat{\mathbf{x}}(r_w^i) + \epsilon(r_w^i)$ .

The position of the peak with respect to the centre of the cross correlation plane,  $\delta\mathbf{x}(r_w^i)$ , provides an estimate of both the average radial and average axial velocity of the fluid inside the data window. Regarding the fact that a single frame is composed from multiple M-mode lines acquired at the  $f_{pr}$  (ultrasound B-mode imaging is a swept process), the axial velocity can be calculated from the axial shift,  $\delta z(r_w^i)$ , by

$$v_z(r_w^i) = \frac{\Delta z}{\Delta t} = \frac{W_{el}\delta z(r_w^i)}{f^{-1} + f_{pr}^{-1}\delta z(r_w^i)}, \quad (3.8)$$

in which  $\Delta z$  is the axial shift expressed in meters and  $\Delta t$  the actual time difference in seconds corresponding to the axial shift. The radial velocity can be calculated from the radial shift,  $\delta\xi(r_w^i)$ , by

$$v_r(r_w^i) = \frac{\Delta r}{\Delta t} = \frac{2c\delta\xi(r_w^i)}{f_s f^{-1}}, \quad (3.9)$$

in which  $\Delta r$  is the axial shift expressed in meters and  $\Delta t$  the actual time difference in seconds corresponding to the radial shift. In this study, only the axial velocity is assessed, since no radial velocity components are present for developed flow in a straight vessel.

### 3.2.5 Validation measurements

The stationary flow was generated with a constant head system positioned between the stationary pump and the inlet of the phantom vessel to attenuate possible flow oscillations caused by the stationary pump. By varying the resistance,  $R$ , at the outlet of the phantom vessel, stationary flow rates ranging from  $0.23 \text{ lmin}^{-1}$  to  $1.23 \text{ lmin}^{-1}$  were generated, corresponding to  $75 < Re < 800$ , in which the Reynolds number,  $Re$ , is defined as:

$$Re = \frac{2a\bar{v}\rho}{\eta(\dot{\gamma}_{char})}, \quad (3.10)$$

in which  $\bar{v}$  is the average axial velocity and  $\rho$  the BMF density.

Flow rates were estimated by means of the Transonic flow probe, which was calibrated before each measurement using a stopwatch and a measuring beaker. For each flow rate an ultrasound measurement was performed. The RF data were filtered as described in the previous section. Application of the cross correlation algorithm resulted in a 2816 instantaneous velocity profile estimations, sampled at 730 Hz. A median filter with a temporal and spatial window size of respectively,  $4 \cdot 10^{-3} \text{ s}$  and  $6.9 \cdot 10^{-5} \text{ m}$ , was applied to remove outliers. The average velocity profile measurement was compared with the analytic approximation of the velocity profile as defined in (3.2). The power-law constant,  $n$ , was assessed by determining the tangent to the Carreau-Yasuda curve at the characteristic shear rate. The characteristic shear rate was based on the mean flow estimate of the Transonic flowprobe.

For the non-stationary flow measurements, a pulsatile flow waveform with a cycle time of 1 s, a mean of about  $0.7 \text{ lmin}^{-1}$  and a peak flow of about  $1.5 \text{ lmin}^{-1}$  was generated by superimposing the flow pulse of the piston pump on the stationary

flow of the stationary pump. This corresponds to an average Reynolds number of 300 and a peak Reynolds number of 900, which is physiologically relevant (Ku et al., 1985). The impedance at the outlet was set such that the induced pressure was high enough to prevent the vessel to collapse but small enough to lead to a negligibly small vessel wall motion. Using LabView, the piston pump was programmed to generate 30 beats. Simultaneously, the flow was measured. During these 30 seconds, 3.8 seconds of fast B-mode RF data were obtained for offline processing. The trigger signal was used to synchronize the flow measurement with the RF data. The RF data were filtered as described in the previous section. Application of the cross correlation algorithm resulted in 2816 instantaneous velocity profile estimations, sampled at 730 Hz. After the removal of outliers by application of a median filter with a temporal and spatial window size of respectively,  $4 \cdot 10^{-3}$  s and  $6.9 \cdot 10^{-5}$  m, a low pass, zero-phase Butterworth filter with a cutoff frequency of 40 Hz was applied to suppress high frequency noise. So no beat-to-beat averaging was performed allowing for real time flow assessment in future ultrasound systems.

A finite-element CFD model of a rigid walled straight tube (Beulen et al., 2009; van de Vosse et al., 2003) (Chapter 2) was applied to calculate the time-dependent velocity distribution across the vessel. The shear rate dependency of the viscosity was incorporated by implementing the Carreau-Yasuda model (3.4) in the CFD model. For the boundary conditions, at the inlet, the flow as assessed in the experiments was prescribed, at the walls, the no-slip condition was applied. The results of the instantaneous velocity profile measurement were compared with the CFD computations.

Subsequently, the flow measurements were compared to flow estimates based on the integration of the measured axial velocity profiles.

## 3.3 Results

### 3.3.1 Blood mimicking fluid

The kinematic viscosity of the BMF was measured as function of shear rate with a Couette rheometer (RFS 2, Rheometrics Scientific). The viscosity was determined for shear rates between  $0.1 \text{ s}^{-1}$  and  $1000 \text{ s}^{-1}$  with 10 measurements per decade (Figure 3.4).

The parameters  $\eta_0$ ,  $\eta_\infty$ ,  $\lambda$ ,  $a$  and  $n$ , of the Carrea-Yasuda model describing the BMF were determined with a least squares fit of (3.4) on the viscosity data presented in Figure 3.4, and are presented in Table 3.1.

The speed of sound was assessed by a time of flight measurement using a single ultrasound transducer and was found to be equal to  $1510 \text{ ms}^{-1}$  at room temperature. The density of the BMF was calculated by measuring the mass of a known volume of BMF (volumetric pipette) by means of a Mettler balance and was found to be equal to  $1100 \text{ kgm}^{-3}$ .

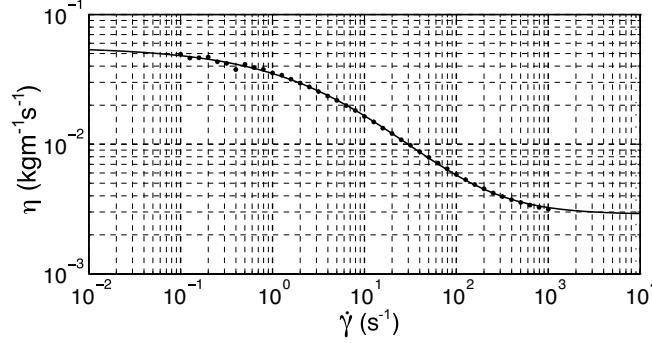


Figure 3.4: Shear thinning behaviour of the BMF, • indicates measurements, the solid line indicates the fit.

Table 3.1: Parameters of the Carreau-Yasuda model describing the BMF as estimated by means of a least squares linear fit.

$\eta_0$ (kgm <sup>-1</sup> s <sup>-1</sup> )	$\eta_\infty$ (kgm <sup>-1</sup> s <sup>-1</sup> )	$\lambda$ (s)	$b$	$n$
$5.6 \cdot 10^{-2}$	$2.9 \cdot 10^{-2}$	$1.0 \cdot 10^{-1}$	$5.3 \cdot 10^{-1}$	$-4.6 \cdot 10^{-2}$

### 3.3.2 Stationary flow

For each measurement, the flow rate, the Reynolds number, the corresponding characteristic shear rate and the resulting power-law constant are presented in Table 3.2.

A comparison between the mean velocity profiles for the ultrasound measurement and the analytic solution of the velocity profile is shown in Figure 3.5. The results were nondimensionalized by the radius  $a$ , of the vessel. The ultrasound transducer was located at  $r/a \approx -5$ .

Excellent agreement was found between the analytic solution and the ultrasound measurements. The root mean square value of the deviation between the measured and calculated velocity profiles ranges from 1 cms<sup>-1</sup>, for the lowest flow rate, to 4 cms<sup>-1</sup>, for the higher flow rates. For the two highest flow rates (1.10 lmin<sup>-1</sup> and 1.23 lmin<sup>-1</sup>), the measured flow profiles appear to be more flat than the calculated velocity profiles.

### 3.3.3 Non-stationary flow

A comparison between the instantaneous velocity profile measurement and the CFD solution of the velocity profile is presented in Figure 3.6. The velocity profiles are shown at 8 distinct phases in the period. The results were nondimensionalized

Table 3.2: Overview of the flow rate, Reynolds number, the characteristic shear rate and the corresponding power law constant

$Q$ (lmin <sup>-1</sup> )	Re	$\dot{\gamma}_{char}$ (s <sup>-1</sup> )	$n$
0.23	75	38	0.52
0.35	140	58	0.55
0.47	214	78	0.57
0.60	302	100	0.59
0.73	397	120	0.62
0.85	489	141	0.64
1.10	691	182	0.68
1.23	800	204	0.70

by the radius,  $a$ , of the vessel. Again the ultrasound transducer was located at  $r/a \approx -5$ .

Overall, the measurements agree very well with the calculated velocity profiles, although minor deviations occur in the near wall region. Especially during the systolic peak deviations between calculation and measurement occur. Near  $r/a = -0.5$ , significant fluctuations of the assessed velocity occur due to an ill-suppressed reverberation.

Integration of the velocity profile over the cross sectional area of the vessel results in a flow estimation. A comparison of the ultrasound-based flow estimate and the direct volume flow measurement is presented in Figure 3.7. To both flow waveforms a low pass, zero phase Butterworth filter with a cutoff frequency of 40 Hz was applied to suppress high frequency noise.

Both flow waveforms agree very well, no significant deviations occurred.

### 3.4 Discussion

The stationary flow measurements indicate that the deviation between the time averaged ultrasound velocity measurement and the analytic solution in the core region is at most about 3 cms<sup>-1</sup>. For the higher flow rates, the measured velocity profiles appear to be more flat than the calculated velocity profiles. For these flow rates, the inlet length might not be sufficient for the flow to fully develop. It should be noted that according to Schlichting (1960), the inlet length,  $L_i$  for a Newtonian laminar flow is given by  $L_i = 0.112Rea_0$ . In the experiment, this condition was sufficiently met, however, due to the non-Newtonian properties of the BMF applied in the experimental setup, the required length might be larger. For both the stationary and non-stationary flow, the deviation between calculated and measured velocity profile increases in the near wall region,  $0.9 < |r|/a < 1.0$ . This can be caused by the fact that the signal of the wall dominates the scattering signal

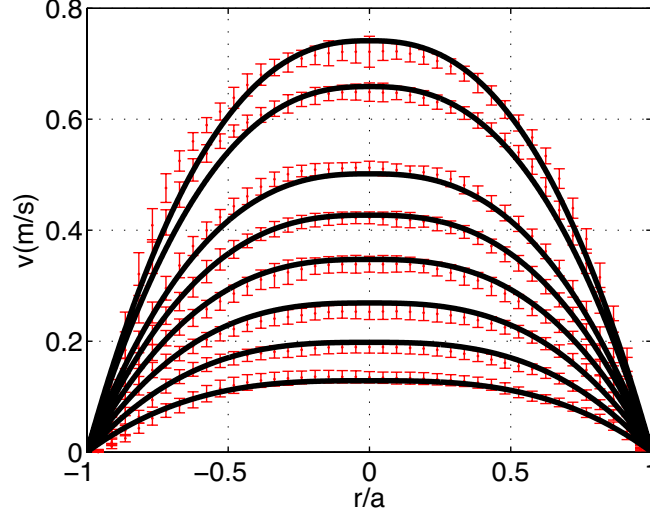


Figure 3.5: Comparison of the ultrasound measurement and the analytic velocity profile ( $\bullet$ , ultrasound measurement;  $-$ , analytic solution)

in this region, which results in errors in the velocity estimation. Furthermore, a small misestimate of the rheologic properties of the BMF can have a significant influence in the near wall region, since close to the wall, the shear rate increases dramatically. This causes deviations in the calculated velocity profile, especially in the near wall region. Finally, the focussing of the ultrasound beam might influence the accuracy of the obtained results. As mentioned in Section 3.2, the beam is focussed at the centre of the vessel. At that position, the beam cross section is minimal. The beam cross section increases upon moving closer to the vessel walls, resulting in an increasing measurement volume. Consequently, the velocity estimate provides an average velocity for an increased measurement volume. Close to the wall, a significant portion of the measurement volume will contain wall signals, causing an underestimation of the velocity.

For the non-stationary flow, at peak systole, a drop of signal occurs at  $r/a \approx -0.7$ , which is approximately the position at which the reverberation of the anterior wall appears. For stationary flow, the reverberation is static, allowing the high pass filter to suppress the reverberation. However, for non-stationary flow, the reverberation is slightly moving. As a result, the applied high pass filter is not able to adequately suppress the reverberations. Furthermore, the velocity approximation is found to be systematically high from  $r = -0.5$  to  $r = 0.9$  for  $t_2$  and  $t_3$ . The small deviations observed are probably caused by measurement errors caused by the flow probe, which result in errors in the CFD derived velocity profiles.

Kim et al. (2004b) have shown that the accuracy and resolution of EchoPIV is improved by application of iterative schemes (Hart, 2000) and smart window

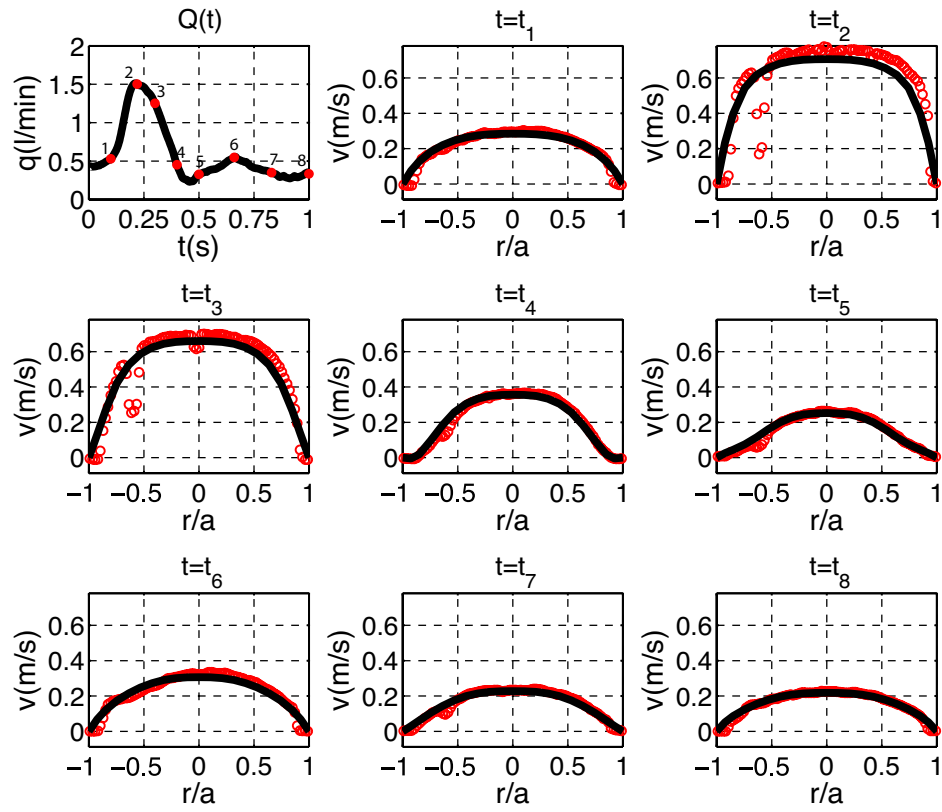


Figure 3.6: Comparison of the ultrasound measurement and the calculated velocity profile (o, ultrasound measurement; —, CFD calculation)

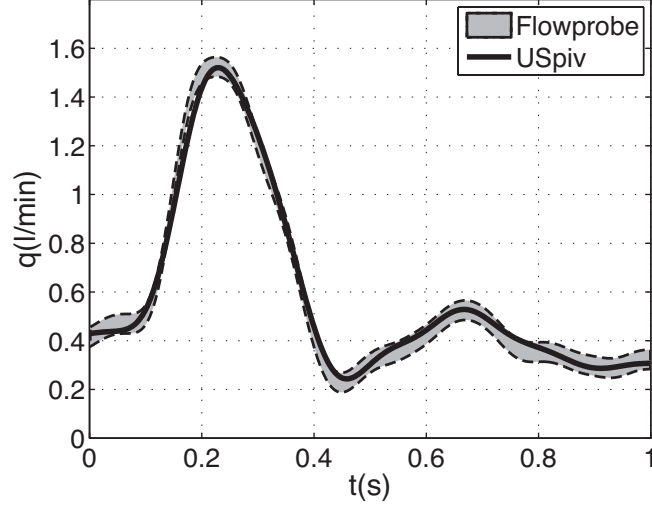


Figure 3.7: Comparison of the ultrasound based flow estimate and the flow probe flow estimate.

offsetting (Westerweel et al., 1997). In principle, these techniques could be applied to the RF data acquired in this study. Although the resolution in radial direction is sufficient, in axial direction, some improvement is desired. However, in axial direction only 14 samples are available, limiting the application of the above mentioned techniques.

Before a practical in-vivo application of the velocity estimation technique is possible, a few issues need to be considered.

First, the ultrasonic backscatter from flowing blood is found to be dependent on the local hemodynamics (Yuan and Shung, 1989). The resulting variation in echogenicity is probably caused by the combined effect of shear rate and acceleration on red blood cell aggregation (Paeng et al., 2004a,b). A drop in echogenicity could have an adverse effect on the accuracy of velocity estimation. To study these consequences, actual blood should be applied in the phantom setup, since for the BMF no aggregation of the scatterers occurs, resulting in a constant echogenicity. Secondly, in-vivo most arteries are curved, resulting in secondary velocity components and an asymmetric axial velocity distribution. The secondary velocity components will result in a motion of the scatterers, transverse to the measurement plane. This may have an adverse effect on the accuracy of velocity estimation. Furthermore, measurements of the axial velocity distribution will result in asymmetric velocity profiles, for which the integration to obtain flow is not trivial. Both consequences will be looked into in upcoming studies.

Finally, probably the biggest challenge for implementation of the velocity estimation technique for in-vivo application is the development of proper clutter removal filters. As in-vivo, the relative strength of the wall signal with respect to

the blood signal is about 60 dB higher, signifying the importance of these filters. The non-stationary flow measurements have shown that reverberations can cause significant errors in the velocity estimation and that adequate filtering is required to suppress these wall signals. In the phantom setup the reverberation occurs at a discrete position because of the uniform vessel wall thickness and properties. As a result, the velocity estimation is disrupted only locally. However, in-vivo, reverberations are present throughout the lumen, further complicating the velocity estimation.

Under the assumption that an adequate anti-clutter filter can be developed, this technique allows a beat to beat analysis of the velocity distribution/flow using a commercially available and clinically approved ultrasound system. In the future, a real time assessment might be possible, since no averaging is required. Furthermore, in combination with pulse wave velocity and distension measurements a simultaneous assessment of pressure and flow will be enabled. This will allow ultrasound to be extended from a local property to a global properties assessment method in clinical practice.

### 3.5 Conclusion

An ultrasound velocity assessment technique is introduced, which allows the estimation of velocity components perpendicularly to the ultrasound beam, using a commercially available ultrasound scanner equipped with a linear array probe. Validation measurements in a phantom setup, with the linear array probe in perpendicular orientation with respect to the vessel have shown that a beat to beat assessment of the axial velocity profile is feasible. In the core region ( $|r|/a < 0.9$ ) an accuracy of  $3 \text{ cm s}^{-1}$  is achieved, in the near wall region ( $0.9 < |r|/a < 1$ ), the accuracy decreases due to the presence of the wall. For a physiologically relevant flow, a successful integration from velocity profile to flow has been performed indicating that this technique can be a valuable asset for an accurate flow estimation in vessels in clinical applications.



## Chapter 4

# Estimation of volume flow in Curved Tubes based on Analytical and Computational Analysis of Axial Velocity Profiles

---

This chapter is based on: A. C. Verkaik, B. W. A. M. M. Beulen, A. C. B. Bogaerds, M. C. M. Rutten, F. N. van de Vosse (2009). Estimation of volume flow in Curved Tubes based on Analytical and Computational Analysis of Axial Velocity Profiles *Physics of Fluids*, **21**(2), 023602-1/13.

## 4.1 Introduction

### 4.1.1 Motivation and aim

Cardiovascular disease (CVD) is one of the most common causes of death in western society; it is responsible for nearly half (49%) of all deaths in Europe (Petersen et al., 2005). The main characteristic changes of arteries related to CVD are stiffening of the arteries, leading to an elevated blood pressure, and the thickening of the artery walls (Laurent et al., 2006). To obtain local hemodynamic variables and to deduce the important biomechanical parameters that are related to the development of CVD, such as compliance, wall shear-stress, pulse wave velocity and vascular impedance, the pressure and flow at specific areas of the blood circulation needs to be monitored, preferably simultaneously and non-invasively.

For more than fifty years ultrasound measurements have been used clinically to investigate patients non-invasively. From the measurements various geometric and hemodynamic variables, such as velocity profiles, vessel diameter, intima-media thickness, wall shear stress and pulse wave velocity can be obtained (Brands et al., 1996). Frequently used methods to determine blood flow velocity in the arteries by means of ultrasound are based on Doppler or cross-correlation to assess axial velocity profiles (Brands et al., 1997). Although the velocity profiles are asymmetric, in general, in clinical practice a Poiseuille profile is assumed and the flow is calculated based on the measured maximum or centreline velocity (Douchette et al., 1992; Mitchell et al., 2004).

The Poiseuille method is adequate for quasi static flow in straight arteries with axial velocities only. However, most arteries are tapered, curved and bifurcating, causing the axial velocity distribution to be altered by transversal velocities, resulting in asymmetrical axial velocity profiles and consequently in inaccurate flow estimations (Krams et al., 2005). To perform the velocity measurements, the ultrasound beam needs to be positioned, not perpendicular, but at a certain angle with respect to the centreline of the artery (the insonation angle). The uncertainty in this angle influences the error of the Doppler measurement (Balbis et al., 2005). Another disadvantage is that the motion of the artery wall cannot be measured accurately at the same time, since the ultrasound beam needs to be positioned perpendicular to the artery for such a measurement.

To study vascular impedance (the transfer function between pressure and the volume flow), it is important to measure simultaneously the pressure and flow at a specific area of the blood circulation of the patient. Theoretically, the local pressure can be deduced from the wall distension and the pulse-wave velocity. A relatively new method to measure axial velocity profiles with ultrasound is a particle imaging velocimetry based ultrasound measurement (Chapter 3). The measured (asymmetric) axial velocity profiles are obtained perpendicularly to the artery and can be combined with the measurement of wall distension at the

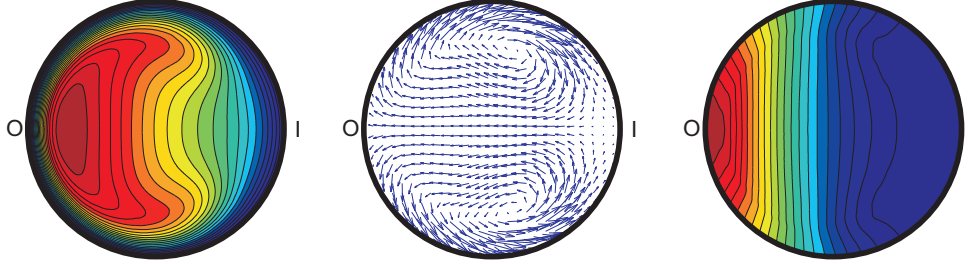


Figure 4.1: An example of the axial velocity distribution in a curved tube (left), the corresponding secondary velocity profile (middle) and the pressure distribution (right), obtained from CFD simulations, where ‘O’ marks the outside of the curve and ‘I’ the inside of the curve.

same time from the same ultrasound signal. To obtain an accurate combined measurement, a novel method needs to be found to accurately estimate the local volume flow from the measured (asymmetrical) axial velocity profiles at a certain cross section of a curved artery. Therefore, this study will focus on the effect of curvature on the axial velocity profile for steady flow through a curved tube and a new volume flow estimation method.

The flow regime of interest is based on the parameters of the carotid artery, to obtain physiologically relevant velocity distributions. The mean axial velocity in the common carotid artery is roughly  $0.2 \text{ ms}^{-1}$ , the radius is about 4 mm and the maximum curvature ratio is about 0.16 (Bovendeerd et al., 1987). It is assumed that blood is a Newtonian fluid with a density of  $\rho = 1.132 \cdot 10^3 \text{ kgm}^{-3}$  and a dynamic viscosity of  $\eta = 3.56 \cdot 10^{-3} \text{ kgm}^{-1}\text{s}^{-1}$ . This results in a Dean number (see theoretical background below for definition) of 580. Therefore, the main region of interest is defined as  $1 \leq Dn \leq 1000$ . The parameters stated above for the density, viscosity and radius are also used for obtaining the analytical and computational results in this study.

#### 4.1.2 Introduction to the theoretical background

Nearly all authors mentioned in the theoretical background later in this paper give the same theoretical/physical explanation to describe steady flow in a curved tube. When a fluid flows from a straight tube into a curved tube, a change in the flow direction is imposed on the fluid. The fluid near the axis of the tube has the highest velocity and therefore experiences a larger centrifugal force ( $\rho w^2/R$ , where  $w$  is the axial velocity,  $\rho$  the density and  $R$  the distance to the centre of curve) compared to the fluid near the walls of the tube. Therefore, the fluid in the centre of the tube will be forced to the outside of the curve. The fluid near the walls, having a lower axial velocity, on the outer side of the curve will be forced

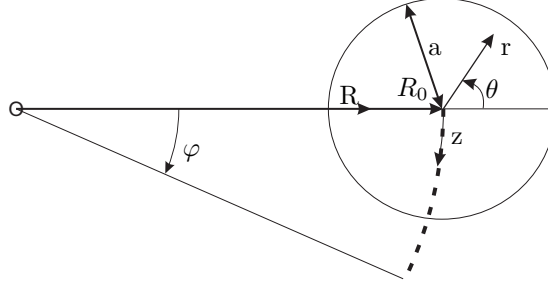


Figure 4.2: The toroidal coordinate system  $(r, \theta, z)$  with velocities  $(u, v, w)$ , which is used to describe flow in a curved tube. The  $z$ -coordinate is defined as  $z = R_0 \varphi$ , where  $R_0$  is the curvature radius of the tube,  $a$  is the radius of the tube and  $R$  is the distance to the centre of curvature, defined as  $R_0 - a < R < R_0 + a$ . In this system  $u$  is the velocity in the  $r$ -direction,  $v$  is the velocity in the  $\theta$ -direction and perpendicular to  $u$ . The velocity in the  $z$ -direction is  $w$ , which is perpendicular to both  $u$  and  $v$ .

inwards along the walls of the tube, because the pressure is lower at the inside of the curve. This overall balance between the radial pressure and the centrifugal forces results in a secondary flow, which influences the axial velocity distribution (Figure 4.1).

During the last century a few analytical approximation methods were derived to explain and predict the behaviour of stationary flow in curved tubes. The solutions obtained by Dean, Topakoglu and Siggers & Waters will be evaluated more extensively and compared with each other (Dean, 1928; Topakoglu, 1967; Siggers and Waters, 2005). These authors derived analytical solutions for small Dean numbers ( $Dn \ll 1$ ) and assumed that the analytical solution for a curved tube is just a small disturbance on the Poiseuille flow of a straight tube, with the flow being driven by the pressure gradient.

Topakoglu (1967) and Siggers & Waters (2005) used the toroidal coordinate system with the coordinates  $(r, \theta, z)$  (Figure 4.2). Dean (1928) used a slightly different definition, but the results as presented in this chapter are adapted to the coordinate system definition of Topakoglu and Siggers & Waters. The most relevant results to this study obtained by the authors with respect to the axial velocity profiles are briefly shown, together with the equations, which relate the flow in a curved tube to the flow in a straight tube.

### 4.1.3 Outline

The chapter is structured as follows. In Section 4.2 a short theoretical background of literature on steady flow in curved tubes is presented. Three analytical approximation methods for fully developed flow in curved tubes are discussed more extensively. Then a novel estimation method, based on the analytical approximation methods, is derived to assess the volume flow through a curved tube from the axial velocity profiles. Finally, a Computational Fluid Dynamics (CFD) model is introduced, which is applied to investigate flow in curved tubes for ranges of flow rate and curvature ratio, where no analytical solution exists.

In the next section (Section 4.3) axial flow profiles from the analytical approximation methods are compared with each other and with the results of the CFD models, as to validate the analytical approximation methods. Furthermore, the CFD solutions are used to validate the novel volume flow estimation method and to compare the new estimation method with the currently used Poiseuille method. The final sections contain the discussion and conclusions.

## 4.2 Methods

### 4.2.1 Theoretical background

In 1928, Dean published the derivation of an analytical solution describing the steady flow of an incompressible fluid in curved tubes with a small curvature,  $\delta = a/R_0$ , where  $a$  is the radius of the tube and  $R_0$  the curvature radius of the tube. This analytical solution was based on the assumption that the secondary flow is just a small disturbance of the Poiseuille flow in a straight tube. He noticed that when the fluid motion is slow, the reduction in flow rate due to the curvature of the tube depends on the single variable  $K$  defined by  $K = 2\text{Re}^2 a/R_0$ , in which the Reynolds number can be defined as  $\text{Re} = aW_{\max}/\nu$ , where  $W_{\max}$  is the maximum velocity in the axial direction and  $\nu$  is the kinematic viscosity.

Dean derived a series solution expanded in  $K$  to describe the fully developed steady flow analytically, in a tube with a small  $K$ -number (see Appendix A.1, which shows the resulting expressions for the axial velocity ( $w$ )). He also derived the ratio of the flow rate through a curved tube in his model ( $Q_{cD}$ ) to that in a straight tube ( $Q_{sD}$ ) driven by the same pressure gradient. This ratio equals:

$$\frac{Q_{cD}}{Q_{sD}} = 1 - 0.03058\left(\frac{K}{576}\right)^2 + 0.01195\left(\frac{K}{576}\right)^4 + O(K^6), \quad (4.1)$$

Dean stated that this equation predicts the flow fairly accurate for  $K < 576$ . When  $K=576$ , a reduction in flow rate is calculated of approximately 1.9%, compared to flow in a straight tube.

The second approximation method was derived by Topakoglu (1967). A power series expansion was performed in  $\delta$  to find the solution for the set of non-linear differential equations he derived (see Appendix A.2). He obtained the following relation for the normalized flow rate through the curved tube in comparison with flow through a straight tube, under the same conditions:

$$\frac{Q_{cT}}{Q_{sT}} = 1 - \frac{1}{48}\delta^2\left(\frac{1.541}{67.2}n^2 + 1.1n - 1\right) + O(n^3), \quad (4.2)$$

where  $n = \left(\frac{Re}{6}\right)^2$ .

In 1968, McConalogue & Srivastava made an extension to the work of Dean. They solved the equations numerically with Fourier series for  $96 < Dn < 600$ . The Dean number was defined as:

$$Dn = 4Re\left(\frac{2a}{R}\right)^{1/2} = \sqrt{\left(\frac{2a^3}{\nu^2 L}\right)\frac{G_{MS}a^2}{\mu}}, \quad (4.3)$$

where  $G_{MS}$  was the mean pressure gradient,  $\nu$  the kinematic viscosity and  $\mu$  the dynamic viscosity coefficient. The Dean number was based on the  $K$ -number proposed by Dean, with  $Dn = 4\sqrt{K}$  and so a Dean number of 96 corresponded to a  $K$ -number of 576.

McConalogue & Srivastava showed that for  $Dn = 600$ , the position of the maximum axial velocity is reached at a distance less than 0.38 times the radius from the outer boundary and that the flow is reduced by 28% in comparison to a straight tube. Collins and Dennis obtained numerical solutions for an extended range of Dean numbers,  $96 < D < 5000$  (Collins and Dennis, 1975). They give the contour plots of the axial and transversal velocities for  $Dn = 96, 500, 605.72, 2000, 5000$ , which show a good agreement with the results of McConalogue and Srivastava (1968) for  $Dn = 96$  and  $Dn = 605.72$ .

The most recent publication of relevance to this study is the article of Siggers & Waters (2005). To derive an analytical approximation method for flow in curved tubes with a small Dean number and small curvature ratio, Siggers & Waters used the series solution for  $w$  expanded in  $Dn$ , where  $w_k$  is allowed to depend on  $\delta$  (see Appendix A.3).

Siggers & Waters have calculated the axial flow rate in a curved tube driven by the axial pressure gradient  $-(\rho\nu^2 G_{SW}/a^3)$  with  $G_{SW} = 4Re$ , which is according to their calculations given by:

$$Q_{cSW} = \pi Dn \left( \frac{1}{8} + \frac{1}{2^7 \cdot 3} \delta^2 - \frac{11}{2^{15} \cdot 3^3 \cdot 5} Dn^2 \delta - \frac{1541}{2^{28} \cdot 3^6 \cdot 5^2 \cdot 7} Dn^4 + O(\delta^4, Dn^2 \delta^3, \dots) \right). \quad (4.4)$$

To obtain the flow ratio, this equation should be divided by the corresponding flow in a straight tube ( $Q_s$ ) and the dimensional flow rate is  $a\nu Q_{cSW}/\sqrt{2\delta}$ .

Table 4.1: Overview of the series expansions used by the authors to derive their analytical approximations.

Author:	Series expansion to:	Flow ratio $\frac{Q_c}{Q_s} =$
Dean (1928)	$K = 2Re^2\delta = \frac{Dn^2}{16}$	$1 - 0.03058\left(\frac{K}{576}\right)^2 + 0.01195\left(\frac{K}{576}\right)^4$
Topakoglu	$\delta$	$1 - \frac{1}{48}\delta^2\left(\frac{1.541}{67.2}n^2 + 1.1n - 1\right)$
Siggers & Waters	$Dn$ & $\delta$	$\frac{\pi Dn}{Q_s}\left(\frac{1}{8} + \frac{1}{2^{7.3}}\delta^2 - \frac{11}{2^{15.3^{3.5}}}Dn^2\delta - \frac{1541}{2^{28.3^{6.5^{2.7}}}}Dn^4\right)$

A summary of the three analytical approximation methods discussed above, has been shown in Table 4.1. In each method a slightly different series expansion method was used and an equation to describe the flow in curved tube compared to the flow in a straight tube was derived.

More extensive overviews of earlier work on flow in curved tubes are given by Pedley (1980), Ward-Smith (1980) and Berger and Talbot (1983).

#### 4.2.2 Flow estimation methods

In clinical practice the volume flow is estimated by assessment of the maximum axial velocity, obtained with Doppler ultrasound, and the assumption of a Poiseuille velocity distribution across the artery. However, the axial velocity profiles of curved arteries become more and more asymmetrical for increasing flow rates ( $Re$ ) and increasing curvature ratios ( $\delta$ ). When the volume flow is estimated based on the maximum velocity, the asymmetry of the velocity profiles is neglected, causing an error in the volume flow estimation. Therefore, a new volume flow estimation method, that can be applied in clinical practice, is investigated and compared with the flow calculations resulting from the Poiseuille method.

Motivated by the analytical solutions for the axial velocities derived by Dean, Topakoglu and Siggers & Waters (see Appendix A), we propose a new method to estimate the flow rate from the velocity profile on a diameter, which we call the ‘cos  $\theta$ -method’. The cross section is divided into two semicircles along the diameter perpendicular to that on which the measurement is taken. The flow rate ( $Q_{cos\theta}$ ) is estimated by assuming the axial flow to be axisymmetric in each semicircle, giving the expression:

$$Q_{cos\theta} = \pi \int_0^a r w^+(r) dr + \pi \int_0^a r w^-(r) dr, \quad (4.5)$$

where  $a$  is the tube radius, and  $w^+(r)$  and  $w^-(r)$  are the measured velocities on the two radii (see Figure 4.3).

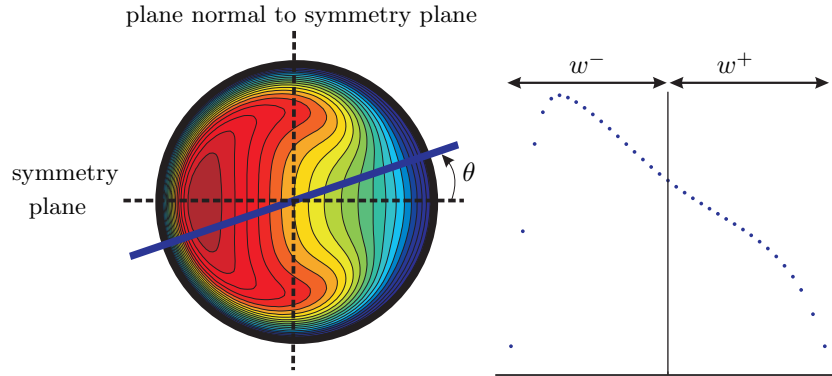


Figure 4.3: Visual explanation of the division of the axial velocity profile into  $w^+$  and  $w^-$ . In this figure the symmetry plane and the plane normal to the symmetry plane of the curved tube are indicated.

We expect this method to produce more accurate results than the Poiseuille method, since each of the three aforementioned analytical approximations shows that the largest correction to Poiseuille flow in the axial velocity profile takes the form  $f(r) \cos \theta$  for some function  $f$ . It can be shown that this correction does not contribute to either the true flux or to the estimate given by the  $\cos \theta$ -method; hence any errors will be given by smaller terms. Conversely, such a term would affect the error in the Poiseuille method, leading to less accurate results.

It should be mentioned that the  $\cos \theta$ -method is in principle applicable for every arbitrary angle of measurement through the tube, as long as the diameter along which the measurement is performed, crosses the centre point. However, in clinical practice the ultrasound beam may not always measure along the true diameter of the artery.

In the results section the (asymmetric) axial velocity profiles calculated with the CFD model (Section 4.2.3) are used as input for the Poiseuille method and the  $\cos \theta$ -method, the imposed flow is used as a reference value.

### 4.2.3 Computational Fluid Dynamics (CFD)

The aim of the CFD simulations is to calculate the axial velocity distribution of steady, fully developed flow in curved tubes. The results will be used to validate the range of applicability of the analytical approximation methods and to investigate the flow in curved tubes at higher Dean numbers, for which the analytical approximation methods are invalid, but which are most relevant for large arteries in humans.

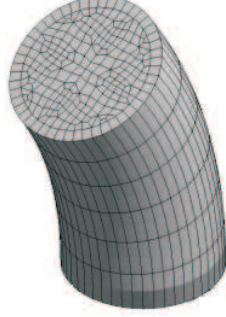


Figure 4.4: The mesh of the CFD model with a curvature ratio of  $\delta = 0.16$ .

It is assumed that the fluid in the curved tube is an incompressible Newtonian fluid. The governing equations are

$$\nabla \cdot \mathbf{v} = 0, \quad \rho \frac{\partial \mathbf{v}}{\partial t} + \rho \mathbf{v} \cdot \nabla \mathbf{v} = -\nabla p + \eta \nabla^2 \mathbf{v},$$

here the gravity and body forces are neglected,  $\mathbf{v}$  is the velocity,  $p$  the pressure,  $\rho$  the fluid density and  $\eta$  the dynamic viscosity. At the tube walls no-slip boundary conditions are applied and at the inlet a flow rate is prescribed.

The mesh of the finite element based CFD model is composed of isoparametric hexahedral volume elements with 27 points. The elements are of the tri-quadratic hexahedron Crouzeix-Raviart type, with a discontinuous pressure over the element boundaries. An integrated or coupled approach is used for the continuity equation (Cuvelier et al., 1986). For the temporal evolution, a first order Euler-implicit discretization scheme is applied. To linearize the convective term, the Newton-Raphson method is chosen. The Bi-CGstab iterative solution method, with an incomplete LU decomposition preconditioner, was applied to solve the linearized set of equations.

A CFD curved tube model for fully developed flow is implemented in the finite element package SEPRAN (Segal, 2004). The mesh of the CFD model consist of a small curved section of 6 axial elements, with a total length of 4 times the radius. It has 18 elements across the diameter and 48 elements along its circumference (see Figure 4.4).

Initially, a Poiseuille velocity distribution is prescribed at the inlet:

$$w(r) = W_{max} \left( 1 - \left( \frac{r}{a} \right)^2 \right). \quad (4.6)$$

For the subsequent time steps the velocity distribution is taken at the plane halfway the tube, this velocity distribution is multiplied with a rotation matrix in order to correct for the curvature, before it is prescribed at the inlet of the

next time step. It was found that the velocity distribution in the midplane is not influenced by the stress free outlet condition. For representative Dean numbers the fully developed curved tube flow obtained with this method was compared to simulations performed with a longer tube, which had a length of 80 times the radius and was long enough to have a fully developed curved tube flow at the end, by only prescribing a Poiseuille inlet flow. A difference of 0.2% was found, whereas a 50-fold reduction in computation time was achieved using the former method.

The simulations were performed for all combinations of  $Dn = 1, 10, 25, 50, 100, 200, 400, 600, 800$  and  $1000$  with  $\delta = 0.01, 0.02, 0.04, 0.08, 0.10$  or  $0.16$ , except  $Dn = 1000$  and  $\delta = 0.01$  due to computational instabilities. For the simulations it is assumed that blood is a Newtonian fluid with a density of  $\rho = 1.132 \cdot 10^3 \text{ kgm}^{-3}$  and a dynamic viscosity of  $\eta = 3.56 \cdot 10^{-3} \text{ kgm}^{-1}\text{s}^{-1}$  (see also Section 4.1.1). In the results section the axial velocity profiles will be analysed and compared to analytical and computational results obtained from literature.

## 4.3 Results

### 4.3.1 Analytical Approximation Methods

Dean, Topakoglu and Siggers & Waters derived analytical approximations by using series expansion, see Table 4.1, to solve the Navier-Stokes equations with the assumption that  $\delta \ll 1$  and  $K \ll 1$  or  $Dn \ll 1$ . The authors all used a different scaling method, which were not always explicitly stated. Therefore, the results of this study are normalized to perform a comparison between the three different analytical approximation methods. The axial velocity profiles are divided by the maximum of their axial velocity. The velocity profiles are given as a function of  $\xi$ , with  $\xi = r/a$  going from  $-1$  to  $1$  (so half of the measurement diameter in the  $-90^\circ < \theta \leq 90^\circ$  plane is defined positive and the other half in the  $90^\circ < \theta \leq 270^\circ$  plane is defined negative).

The  $Q_c/Q_s$  flow ratios of the analytical approximation methods are plotted in Figure 4.5. The solution derived by Dean only depends on  $K$ , so if  $K$  (or  $Dn$ ) does not change, the solution will not change for different curvature ratios. The solutions of Topakoglu and Siggers & Waters do change for different curvature ratios, while the Dean number stays the same. Around  $Dn = 60$  Dean's solution starts to deviate from the other solutions, it even increases for  $Dn > 100$ . The flow ratios derived by Topakoglu and Siggers & Waters give nearly the same result. They keep on decreasing and become negative for  $Dn > 220$  (not visible in Figure 4.5).

Figure 4.6 shows the normalized axial velocity profiles in the plane of symmetry derived by the three analytical solutions for  $Dn = 1, 50, 100$  and  $\delta = 0.01, 0.16$

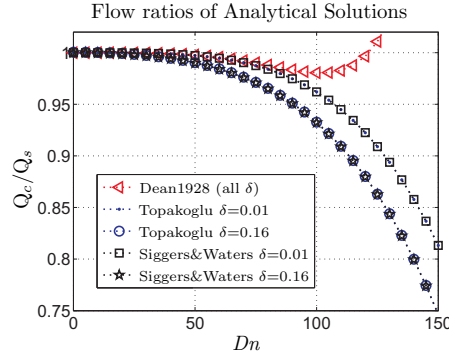


Figure 4.5: The flow ratios between flow in a curved tube ( $Q_c$ ) and flow in a straight tube ( $Q_s$ ) of the analytical approximations derived by Dean, Topakoglu and Siggers and Waters.

based on the equations for the axial velocities of Appendix A. As  $Dn$  increases the position where the maximal velocity is achieved moves towards the outside of the curve, while as  $\delta$  increases this position moves to the inside of the curve, this effect is supported by the analytical solutions of Topakoglu and Siggers & Waters. For example if  $\delta = 0.16$ , then as long as  $Dn < 50$ , the maximum velocity is achieved at a positive value of  $\xi$ , closer to the inside of the curve.

#### 4.3.2 CFD

Results obtained with the CFD model for all simulations performed with a curvature ratio of  $\delta = 0.16$  are shown in Figure 4.7. The position of the maximum velocity can be determined from the axial velocity profiles of the symmetry plane. For a higher Dean number and so a higher Reynolds number, the position of the maximum velocity shifts more to the outside of the curve, which is in accordance to the derived analytical solutions of Dean, Topakoglu and Siggers & Waters.

The position of the maximum velocity as function of the Dean number and the curvature ratio is shown in Figure 4.8. It shows that the position of the maximum velocity as function of the curvature ratio ( $\delta$ , left graph) or as function of the  $Dn$  number (right graph) have different relations. There seems to be a linear relation between the position of the maximum and  $\delta$ , but this linear relation is not the same for different Dean numbers.

The right graph of Figure 4.8 shows that for low Dean numbers the position of the maximum velocity shifts to the inside of the curve. From  $Dn = 50$  and higher the position of the maximum velocity is always shifted to the outside of the curve. For increasing Dean numbers the shift increases. The differences in the position

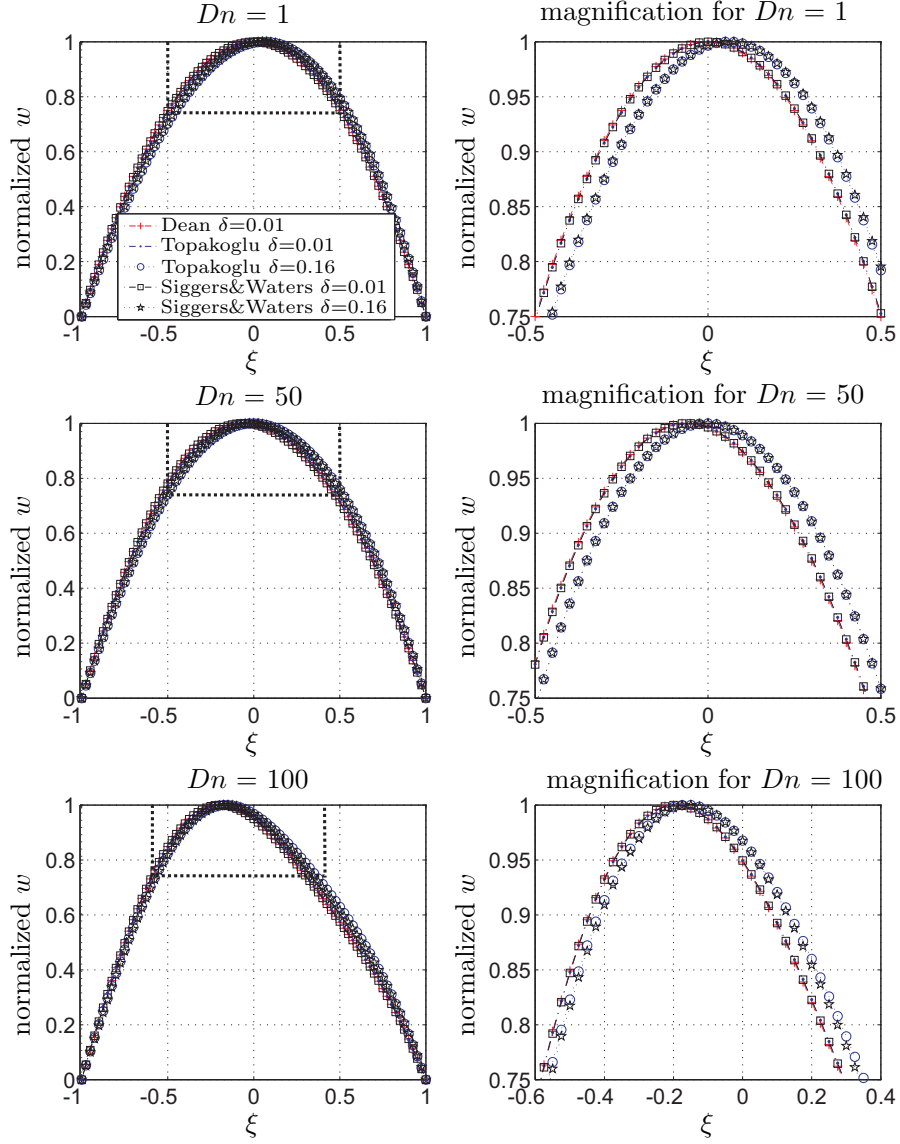


Figure 4.6: The normalized axial velocity profiles of the analytical approximations derived by Dean, Topakoglu and Siggers & Waters for  $Dn = 1$ , 50 and 100 and  $\delta = 0.01$  or 0.16. The right panels depict magnifications of the central region. The velocity profiles derived by Dean do not change for different  $\delta$ 's for a fixed Dean number, therefore, only  $\delta = 0.01$  is shown. The axial velocity profiles with  $\delta = 0.01$  are lying on top of each other for every Dean number, while the velocity profiles of Topakoglu and Siggers & Waters for  $\delta = 0.16$  are shifted to the right.

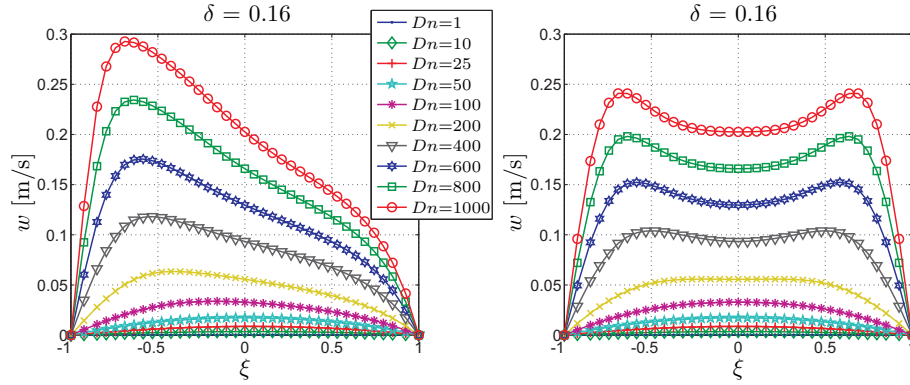


Figure 4.7: The axial velocity profiles for different Dean numbers for  $\delta = 0.16$ . In the left figure the normalized velocity profiles for the symmetry plane and in the right figure the normalized velocity profiles for the plane normal to the symmetry plane.

of the maximum velocity for different curvature ratios but with the same Dean number become less for higher Dean numbers.

The position of the maximum axial velocity as function of Reynolds number is shown in Figure 4.9. Around  $Re = 20$  all curves pass through the symmetry point (zero), which from now on is called ‘zero-shift point’. For smaller Reynolds numbers the position of the maximum is shifted to the inside of the curve and for higher Reynolds numbers the position is shifted to the outside of the curve.

### 4.3.3 CFD vs. Analytical Approximation Methods

The results of the analytical approximation methods and the CFD simulations can be compared by their normalized axial velocity profiles. The analytical solution derived by Siggers & Waters is compared to the profiles calculated with the CFD model in Figure 4.10. These graphs show that the analytical solutions are similar to the CFD simulations for  $Dn \leq 50$  and  $0.01 \leq \delta \leq 0.16$ . For  $Dn = 100$  the analytical approximation deviates from the axial velocity profile derived with the CFD model. This deviation increases for higher Dean numbers. The same results will be obtained for the axial velocity profiles calculated from the analytical approximation method of Topakoglu, as his method gives nearly the same results as the approximation method from Siggers & Waters. The analytical approximation method of Dean agrees with the other analytical solution methods for  $\delta = 0.01$ , as this value is closest to  $\delta=0$ , for which the analytical solution was derived.

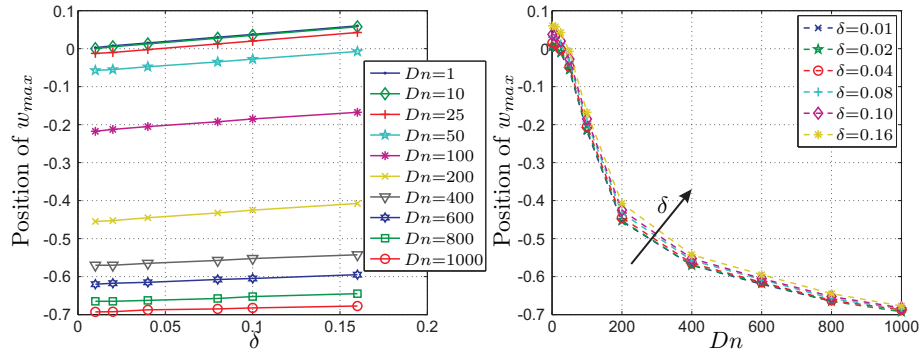


Figure 4.8: The position of the maximum velocity as function of  $\delta$  for different Dean numbers on the left and on the right as function of Dean number for different curvature ratios.

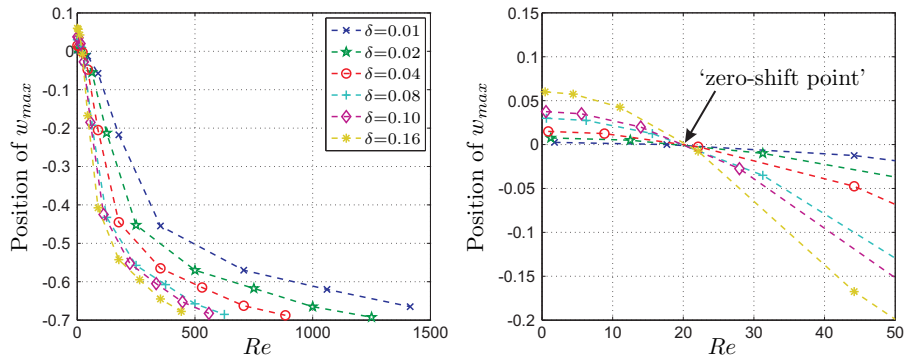


Figure 4.9: The position of the maximum velocity ( $w_{max}$ ) as function of Reynolds number for different  $\delta$ , with on the right a magnification of the zero-shift point around  $Re = 20$ .

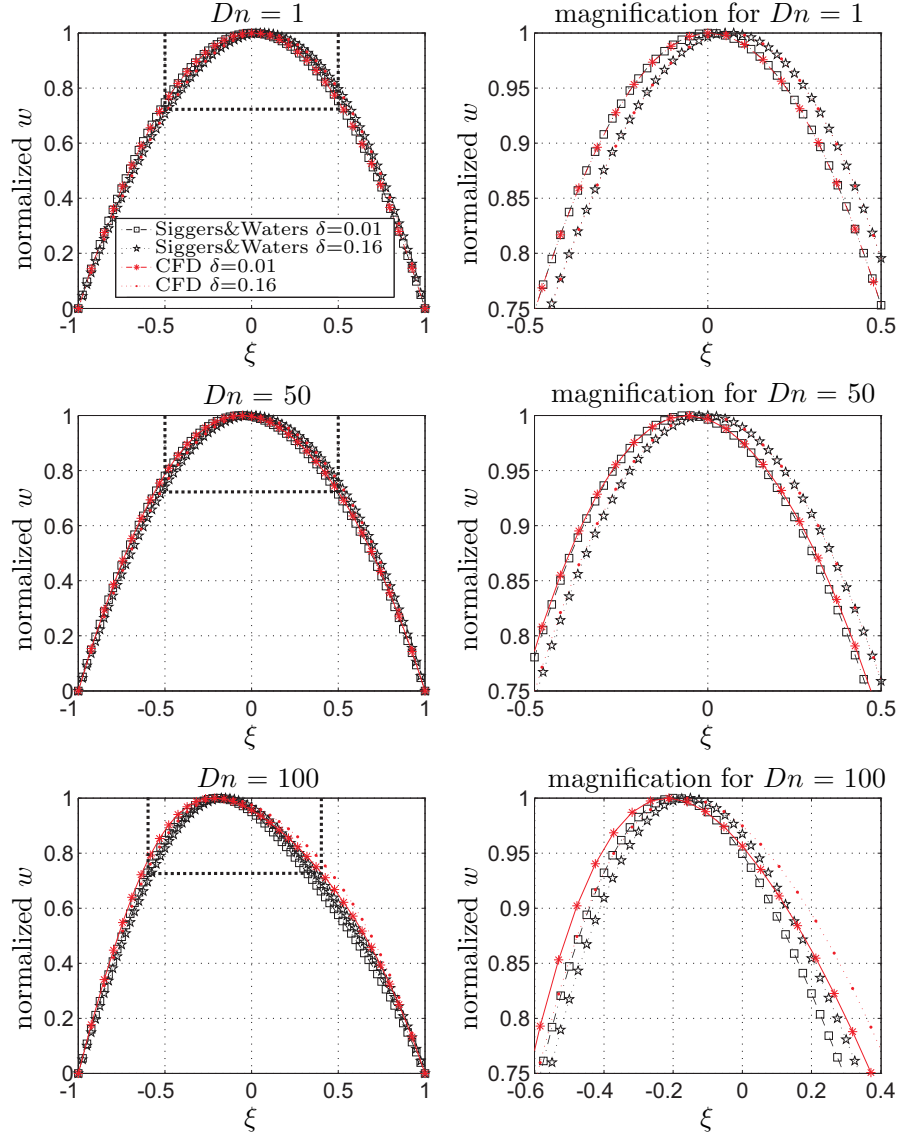


Figure 4.10: The normalized axial velocity profiles of the analytical solution derived by Siggers & Waters versus the results of the infinite tube simulation for  $Dn=1$ , 50 or 100 and  $\delta = 0.01$  or 0.16.

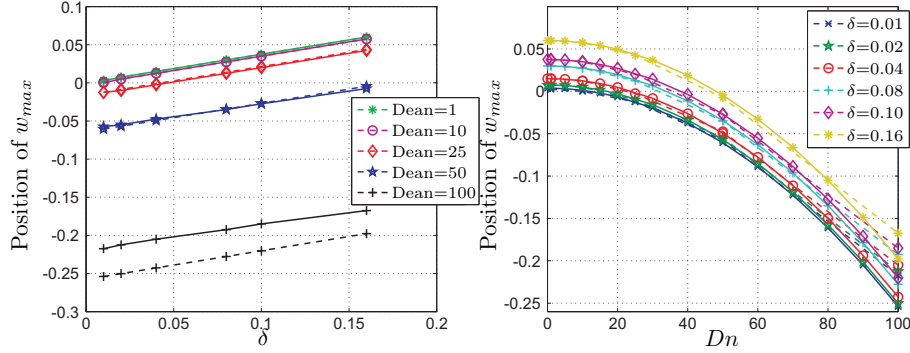


Figure 4.11: Comparison of the results of the CFD simulations (dotted line) and the analytical approximation derived function of Siggers & Waters (solid line). At the left, the position of the maximum velocity is plotted as function of the curvature ratio for different Dean numbers. The right graph shows the position of the maximum velocity as function of Dean number for different curvature ratios. The solutions for  $Dn = 1, 10$  are very close, while a little difference can be seen for  $Dn = 25, 50$  and for  $Dn = 100$  the solutions of the CFD are distinct from the analytical approximation.

Siggers & Waters derived their analytical approximation for curved tubes using series expansion and by assuming that  $Dn \ll 1$  and  $\delta \ll 1$ . The relative position of the maximum velocity  $r_{W_{max}}$  is related to the Dean number and curvature ratio by:

$$r_{W_{max}} = \frac{19Dn^2}{2^{14} \cdot 3^2 \cdot 5} - \frac{3\delta}{8} + O(\delta^3, Dn^2\delta^2, Dn^4\delta, Dn^6). \quad (4.7)$$

Figure 4.11 shows this relative position as function of Dean number for different values of  $\delta$  in comparison with the results obtained with the CFD model (see also Figure 4.8). In the left graph the position of the maximum velocity as function of  $\delta$  is given for both methods and in the right graph as function of the Dean number. Again the results of the analytical approximation coincide with the CFD results for  $Dn \leq 50$ , while for higher  $Dn$  numbers the analytical solutions starts to deviate from the CFD results.

#### 4.3.4 Flow estimation methods

The axial velocity profiles obtained with the CFD model are used as input to compare the volume estimation methods with each other and with the imposed flow. The flow estimation based on the  $\cos \theta$ -method is performed on the axial

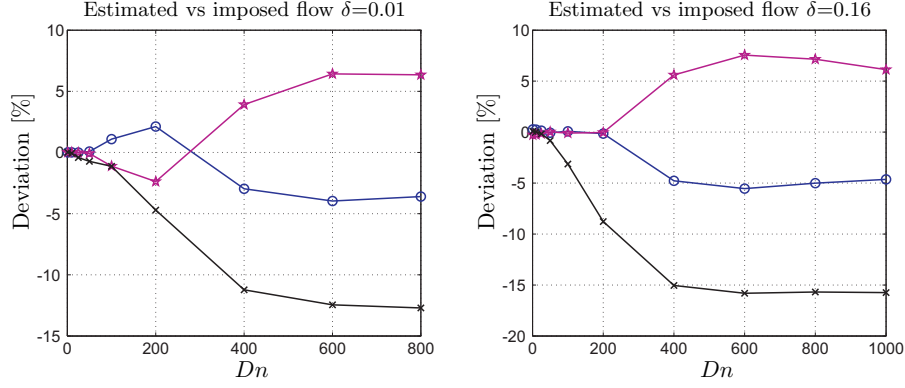


Figure 4.12: The deviation of the estimated volume flow from the imposed volume flow for  $\delta = 0.01$  (left figure) and  $\delta = 0.16$  (right figure) as function of Dean number. The estimated flow is based on the  $\cos \theta$ -method applied to the a velocity measurement along the symmetry plane (-o-) or the plane normal to the symmetry plane (-\*) or the Poiseuille method applied to the symmetry plane (-x-).

velocity profiles of the symmetry plane and the plane normal to the symmetry plane (see Figure 4.3). The deviation of the estimated flow from the imposed flow for the different flow estimation methods are shown in Figure 4.12 for simulations with  $\delta = 0.01$  and  $\delta = 0.16$ .

The results in Figure 4.12 show that the  $\cos \theta$ -method and the Poiseuille method give similar results for  $Dn \leq 100$ . For higher Dean numbers the Poiseuille method shows a consistent underestimation of the volume flow, which is nearly three times larger than the underestimation of the  $\cos \theta$ -method for high Dean numbers ( $Dn > 400$ ). The  $\cos \theta$ -method with the plane normal to the symmetry plane as input results in an overestimation of the flow for higher Dean numbers.

The deviation of the calculated flow of the  $\cos \theta$ -method based on profiles in the symmetry plane are compared to the imposed volume flow for different Dean numbers and curvature ratios (see Figure 4.13).

For a curvature ratio of  $\delta = 0.01$  and  $1 \leq Dn \leq 800$ , the  $\cos \theta$ -method based on the axial velocity profile in the symmetry plane has a maximum deviation from the imposed flow of less than 4%, while the Poiseuille method has a maximum deviation of 12.7%. The  $\cos \theta$ -method based on the axial velocity profile in the plane normal to the symmetry plane results in a maximum deviation of 6.4%,

A curvature ratio of  $\delta = 0.16$  and  $1 \leq Dn \leq 200$  gives similar results for the  $\cos \theta$ -method based on the axial velocity profiles of both the symmetry and its normal plane. For higher Dean numbers the  $\cos \theta$ -method based on the symmetry plane

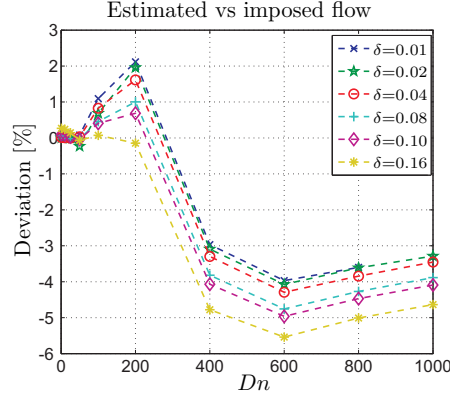


Figure 4.13: The deviation of the estimated volume flow (based on the  $\cos\theta$ -method) compared to the calculated flow in percentages for different curvatures, based on velocity profiles obtained from the symmetry plane.

gives an underestimation of the flow, which is maximally 5.5% at  $Dn = 600$ . The  $\cos\theta$ -method based on the plane normal to the symmetry plane gives an overestimation of the flow which is maximally 7.5% at  $Dn = 600$ . The Poiseuille method gives a consistent underestimation for  $Dn > 50$ , which is maximally 15.8%.

Figure 4.13 shows that for the different curvatures the deviation of the  $\cos\theta$ -method is maximally 5.5% and is reached for all curvatures around  $Dn = 600$ , for higher Dean numbers the deviation decreases. For small Dean numbers ( $1 \leq Dn \leq 25$ ) the higher curvature ratios give a slightly larger error, while for intermediate Dean numbers ( $25 \leq Dn \leq 200$ ) the smaller curvature ratios result in larger deviations from the imposed flow. Finally, for high Dean numbers ( $400 \leq Dn \leq 1000$ ) the largest curvature ratios have the largest deviation.

## 4.4 Discussion

### 4.4.1 Analytical Approximation Methods

All analytical approximation methods have been derived for  $Dn$  or  $K \ll 1$  and  $\delta \ll 1$ , however, the results are accurate for  $Dn \leq 50$ . The equations derived for the flow ratios, that compare flow in a curved tube to flow in a straight tube with the same pressure gradient, already show that Dean's analytical solution does not depend on  $\delta$  for a constant  $K$  or  $Dn$ . His solution becomes unrealistic at smaller Dean numbers, compared to the solutions of Topakoglu and Siggers & Waters,

the flow ratio increases for  $Dn > 100$ . The analytical approximation methods derived by Topakoglu and Siggers & Waters depend on the curvature ratio and give similar results.

Investigation of the axial velocity profiles results in essentially the same observations. The three approximation methods give the same results for  $\delta = 0.01$ . An interesting effect is the displacement of the maximum velocity to the inside of the curve for higher curvature ratios in the analytical solutions derived by Topakoglu and Siggers & Waters. Topakoglu did not mention this effect in his paper. Siggers & Waters did notice that their equation for  $w_{01}$  causes the maximum velocity to move towards the inside of the curve for increasing  $\delta$ , but did not give a physical explanation.

#### 4.4.2 CFD

The fully developed flow profiles calculated with the CFD tube model correspond with results from literature (Collins and Dennis, 1975; McConalogue and Srivastava, 1968). However, it is difficult to compare the results exactly. Often only the Dean number is given in combination with the value of the (scaled) maximum axial velocity, but nothing is known about the exact values for the curvature ratio, diameter, viscosity parameters etc. A complete description of a flow problem in a curved tube requires two of the characteristic dimensionless numbers  $\delta$ ,  $Re$  and  $Dn$  to be stated.

Most research is focused on the flow ratio of flow through a straight tube in comparison with flow in a curved tube driven by the same pressure gradient. For the simulations in this study, flow is prescribed and no attention has been paid to the pressure gradient, since this cannot be assessed by ultrasound measurements yet.

Besides a qualitative comparison between the contour plots of the axial velocities, another more quantitative comparison can be made by observing the position of the maximum velocity. McConalogue & Srivastava used a Fourier-series development method to solve the momentum and continuity equation in the toroidal system numerically (McConalogue and Srivastava, 1968). They published their resulting contour plots of the axial velocity for different values of Dean number between  $Dn = 96$  and  $Dn = 605.72$ . From these contour plots the relative position of the maximum velocity can be deduced.

In Figure 4.14 the results are shown in the same graph as the maximum positions computed with the CFD model. The figure shows a good resemblance between the results from McConalogue & Srivastava and the results of the CFD model. As McConalogue & Srivastava state that they assume  $\delta$  to be small, one should expect their results to agree most closely with the  $\delta = 0.01$  solutions of the simulations. As can be seen in Figure 4.14 their results do match the  $\delta = 0.01$  results closely, except two data points around  $Dn = 200$ .

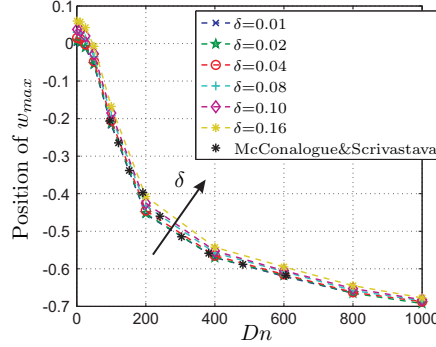


Figure 4.14: The position of the maximum velocity as function of Dean number for different  $\delta$ 's with the results of McConalogue and Srivastava (1968).

#### 4.4.3 CFD vs Analytical Approximation methods

Comparison of the analytical axial velocity profiles with the calculated profiles of the CFD simulations show that the analytical solution predicts the axial velocity very well for  $Dn \leq 50$ . It is striking that, despite the assumptions made for the approximation (small  $\delta$ ), the analytical solution also coincides very well with the results of the CFD model for higher curvature ratios, up to  $\delta = 0.16$ . Furthermore, the equation for the position of the maximum velocity derived by Siggers & Waters coincides very well for  $Dn \leq 50$  with the calculated positions of the CFD model.

The computational method presented in this study and the analytical method of Siggers & Waters both predict that for low Dean numbers the maximum position is shifted to the inside of the curve. This effect increases for an increasing curvature ratio. Since the velocity profiles are fully developed in space and time, the shift to the inside of the curve cannot be explained by entrance effects, which holds for frictionless flow in the core of the tube (Bovendeerd et al., 1987; Agrawal et al., 1978).

A possible explanation could be that for low Dean numbers, and especially for low Dean numbers with a larger curvature ratio, the Reynolds number is low. Then the values of the velocity in the secondary field are small, which results in a negligible pressure gradient in the radial direction which becomes comparable to the pressure distribution in a straight tube. However, the geometry of the tube is still curved: at the inside of the bend the fluid is subject to the highest axial pressure gradient. Therefore the fluid velocity will be maximal at the inside of the tube. This implies that the shift towards the inside of the curve is a pure geometry driven effect.

The shift of the maximum velocity to the inside of the curve for lower Dean numbers was noticed earlier by Murata et al., but not many other authors mention

this phenomenon (Murata et al., 1976). Murata et al. did not investigate this effect for different curvature ratios and Reynolds numbers.

Plotting the relative position of the maximum velocity as function of the Reynolds number shows a ‘zero-shift point’, as we would like to call it (see Figure 4.9). Around  $Re \approx 20$  the effect caused by the axial pressure gradient balances the effect of the centrifugal forces (radial pressure difference). This zero-shift point can also be found by inserting  $r_{Wmax} = 0$  in the equation derived by Siggers & Waters, which results in two solutions. The first solution is  $\delta = 0$ , which corresponds to a straight tube, and the second solution is  $Re = 21.3$ , which corresponds to the zero-shift point.

#### 4.4.4 Flow estimation methods

The Poiseuille method and the  $\cos \theta$ -method give similar results for  $Dn \leq 100$ . For higher Dean numbers the Poiseuille method becomes more and more inaccurate, with an estimation error of 12.7% compared to the imposed flow for  $Dn = 1000$  and  $\delta = 0.01$ . The  $\cos \theta$ -method gives much better results and deviates maximally 4% from the imposed flow. The  $\cos \theta$ -method based on the axial velocity profile in the plane perpendicularly to the plane of symmetry results in a maximum deviation of 6.4%. The results for a curvature ration of 0.16 are similar, but all deviations are slightly elevated.

The  $\cos \theta$ -method has been investigated for different curvature ratios, see Figure 4.13, and the maximal deviation in the symmetry plane is only 5.5%, which is a much better estimation than the Poiseuille method. The analytical approximation methods support the  $\cos \theta$ -method, because all derived methods show that the first correction term on the Poiseuille component of the axial velocity depends on  $\cos(\theta)$ , for a fixed  $r$ . To investigate whether the analytical solutions are right, the axial velocity (obtained from the CFD simulations) is plotted as function of a fixed  $r$ ,  $r = 2$  mm, for  $Dn = 100$  and  $\delta = 0.16$  (Figure 4.15). This figure shows that the axial velocity as function of  $\theta$  for a fixed  $r$ , can be described with a cosine function, which is plotted in the figure based on the mean axial velocity and the amplitude at  $\theta = 0$ .

As shown earlier, the analytical approximation methods are valid for  $Dn < 100$ . So the error of the  $\cos \theta$ -method can be caused by an asymmetric, multi-harmonic change of the axial velocity in curved tubes for higher Dean numbers. Therefore, the axial velocity is plotted as function of a fixed  $r$ ,  $r = 2$  mm, for  $Dn = 1000$  and  $\delta = 0.16$  (see right graph of Figure 4.15). From this result it is clear that for this case a single cosine function cannot approximate the axial velocity as a function of  $\theta$  for a fixed  $r$  anymore.

In clinical practice, the axial velocity profile will not, in general, be measured exactly on the symmetry plane. Therefore the influence of the orientation of the ultrasound beam with respect to the tube is investigated, by estimating the

flow of the axial velocity profiles obtained under a certain angle with respect to the symmetry plane (see Figure 4.16). This indicates that for  $Dn = 1000$  and  $\delta = 0.16$ , the maximum error depending on the angle is an overestimation of volume flow calculation by 6.1%, which is obtained at the plane normal to the symmetry plane ( $\theta = 90^\circ$ ).

## 4.5 Conclusion

The analytical approximation methods for flow in curved tubes derived by Dean, Topakoglu and Siggers & Waters were investigated and a quantitative comparison has been made. The results show that the analytical approximation derived by Dean does not depend on the curvature ratio for a fixed Dean number, while the solutions of Topakoglu and Siggers & Waters do. The solutions derived by Topakoglu and Siggers & Waters give similar results.

A CFD model for fully developed curved tube flow was developed to simulate the axial velocity in a curved tube and simulations were performed in the range of  $1 \leq Dn \leq 1000$  and  $0.01 \leq \delta \leq 0.16$ . The axial velocity profiles obtained with the CFD model are in good agreement with results presented in literature, although it is sometimes hard to compare the results exactly with each other (McConalogue and Srivastava, 1968; Collins and Dennis, 1975).

The analytical approximation methods were compared to the results of the CFD model. The approximations derived by Topakoglu and Siggers & Waters predict the velocity profiles very well for  $Dn \leq 50$  and fair for  $Dn \leq 100$  and all curvature ratios, while Dean's approximation only coincides with  $\delta = 0.01$ . For higher Dean numbers ( $Dn > 100$ ) no proper analytical approximation method exists.

At lower Dean numbers, the position of the maximum velocity shifts to the inside of the curve, while at higher Dean numbers the position of the maximum velocity is located at the outside of the curve. This phenomenon can be explained by the relatively low pressure gradient in radial direction in comparison to the axial pressure gradient, causing the fluid to follow the path with the highest axial pressure gradient, which is at the inner curve at low flow rates.

A zero-shift point is found when the relative position of the maximum velocity, obtained from the CFD simulations, is plotted as a function of the Reynolds number. The equation for the position of the maximum velocity derived by Siggers & Waters was used to derive the exact zero-shift point, which is at  $Re = 21.3$ . At this point the effect caused by the axial pressure difference equals the effect of the centrifugal forces (radial pressure gradient).

The  $\cos \theta$ -method is supported by the analytical approximation methods. For  $Dn \leq 100$  the Poiseuille method is still sufficient, but for  $Dn \geq 100$  the  $\cos \theta$ -method estimates the volume flow nearly three times better than the Poiseuille method,

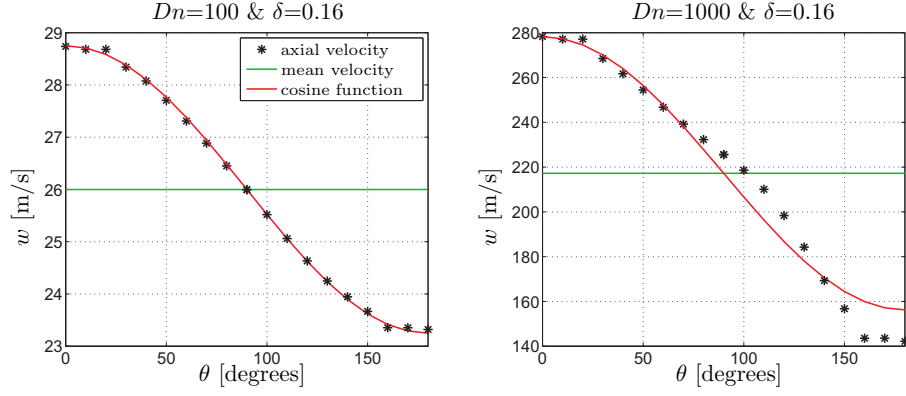


Figure 4.15: The axial velocity for a fixed radius,  $r = 2\text{mm}$ , as function of the angle ( $\theta$ ) with on the left  $Dn = 100$  and  $\delta = 0.16$  and on the right  $Dn = 1000$  and  $\delta = 0.16$ .

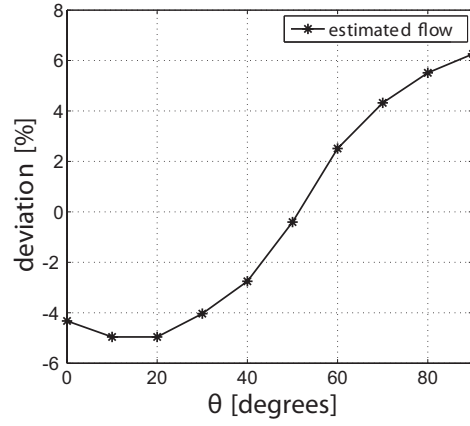


Figure 4.16: The deviation of the estimated volume flow from the imposed flow for different angles with respect to the symmetry plane of the simulation with  $Dn=1000$  and  $\delta = 0.16$ .

for  $\delta = 0.01$  4% versus 12.7%. The axial velocity profile measured at a certain angle from the symmetry plane results in an estimation error of at most 6.2% for  $Dn=1000$  and  $\delta = 0.16$ .

These results indicate that it is possible to estimate the volume flow through a curved tube from a given (asymmetrical) axial velocity profile with the  $\cos\theta$ -method, with a reasonable accuracy. Before this method can be used in clinical practice, the  $\cos\theta$ -method needs to be tested on unsteady flows, non-Newtonian fluids and finally on axial velocity profiles obtained from patients or volunteers. It should be kept in mind that in most arteries the flow is not fully developed. However, if entrance effects have the same  $\cos\theta$  dependent effect on the axial velocity, this will not give additional errors for the flow estimation with the  $\cos\theta$ -method.

## Chapter 5

# Flow estimation in curved vessels by means of non-invasive ultrasound

---

The contents of this chapter have been submitted for publication: B. W. A. M. M. Beulen, A. C. Verkaik, M. C. M. Rutten, F. N. van de Vosse. Volume flow estimation in curved vessels by means of perpendicular ultrasound. *Experiments in Fluids*, submitted (2009)

## 5.1 Introduction

Haemodynamic factors play a significant role in the development and localisation of cardiovascular disease (CVD) (Fung, 1993; Caro et al., 1971). Arteries affected by CVD in general show thickening and stiffening of the vessel walls, leading to elevated blood pressure (Laurent et al., 2006). To deduce the biomechanical parameters that are related to the development of CVD, such as compliance, wall shear stress, pulse wave velocity and vascular impedance, and to obtain local hemodynamic variables, the pressure and flow at specific areas of the arterial system need to be monitored, by preference non-invasively and simultaneously.

In clinical practice, ultrasound is frequently used as a non-invasive method to obtain geometric and haemodynamic variables such as blood (centreline) velocity, wall shear stress, vessel diameter, intima-media thickness (IMT) and pulse wave velocity (PWV) (Brands et al., 1998, 1999). The local flow is derived from the vessel diameter and blood velocity assessment, whereas the local pressure can theoretically be derived from a simultaneous assessment of the vessel wall distension and PWV.

For the velocity assessment, often Doppler ultrasound is applied. To perform the velocity measurements, the ultrasound probe needs to be positioned at a certain insonification angle (non perpendicular) with respect to the blood velocity vector. A reliable velocity assessment necessitates this angle to be accurately known and constant during the measurement. Deviations in insonification angle result in velocity errors of the same order (Fillinger and Schwartz, 1993; Gill, 1985). For flow estimation, a certain velocity distribution, e.g., a Poiseuille or Womersley profile is assumed and the flow is calculated based on the maximum or centreline velocity (Douchette et al., 1992). The Poiseuille approximation is suitable for quasi-static flow in straight arteries, whereas the Womersley approximation is valid for in-stationary flow in straight arteries. However, most arteries are tapered, curved and bifurcating, causing the axial velocity distribution to be altered by transversal velocities, resulting in asymmetrical axial velocity profiles and consequently in inaccurate flow estimations (Krams et al., 2005). Additionally, the position of the vessel walls needs to be known exactly in order to perform the integration of velocity to flow. An accurate assessment of the wall position is only achievable with the ultrasound beam positioned perpendicular to the vessel. As a result, a simultaneous assessment of velocity by Doppler ultrasound and wall position is impossible, which hampers an accurate flow assessment.

Several blood velocity measurement techniques based on ultrasound have been reported to overcome the angle dependency of Doppler ultrasound and to allow 2D velocity estimation. Methods were introduced in which multiple ultrasound beams were applied to overcome the angle dependency (Fox, 1978; Overbeck et al., 1992). However, due to beam widening, these methods resulted in increasing standard deviations and biases in the velocity estimates for increasing depth. Ultrasound speckle velocimetry (USV) enables assessment of 2D velocity vectors by analyzing the acoustic speckle pattern of the flow field (Bohs et al., 1993, 1995;

Sandrin et al., 2001; Trahey et al., 1987). However, for an accurate, low noise velocity assessment, this technique requires specially modified ultrasound systems, custom scanning sequences and custom developed transducers. Furthermore, due to the requirement of very high particle concentrations, the application of USV for in-vivo applications is limited (Kim et al., 2004a). The application of Particle Image Velocimetry (PIV) techniques (Adrian, 2005) to ultrasound was first reported by Crapper et al. (2000). Kim et al. (2004b,a) introduced Echo PIV, which was applied on images enhanced by an Ultrasound Contrast Agent, obtained by means of a commercially available ultrasound scanner equipped with a phased array transducer. Liu et al. (2008) developed a custom-designed ultrasound system which allowed flexible control of the Echo PIV parameters, extending the measurable velocity range and improving the spatial resolution.

In Chapter 3, an ultrasound velocity assessment technique similar to echo PIV was applied to estimate velocity components perpendicular to the ultrasound beam, using a linear array transducer connected to a commercially available, clinically approved ultrasound system equipped with RF data output and acquisition system. In the remainder of this study, this method will be referred to as ultrasonic perpendicular velocimetry (UPV). The UPV method enables simultaneous assessment of axial velocity profile and vessel wall position and was validated by comparing velocity profile measurements performed on stationary and in-stationary flow in a phantom setup to computational fluid dynamics (CFD) calculations (Chapter 3). For flow estimation in curved geometries, Verkaik et al. (2009) introduced the  $\cos \theta$ -method, which allows an accurate flow assessment based on integration of axial (asymmetrical) velocity profiles, assuming that the asymmetry in the velocity distribution is primarily caused by the local curvature of the vessel (Chapter 4). The integration method is supported by the existing analytical approximations for steady and unsteady Newtonian flow in curved vessels (Dean, 1927; Topakoglu, 1967; Siggers and Waters, 2005, 2008). Furthermore, a validation by means of CFD calculations has shown that this method is more accurate than the Poiseuille approximation for stationary Newtonian flow through weakly curved vessels.

The aim of this study is to test the applicability of the UPV assessment in combination with the  $\cos \theta$ -method to assess axial velocity distribution and volume flow for stationary and non-stationary flow in curved vessels. In a phantom setup, measurements of the axial velocity profile in planar curved vessels are performed by means of the UPV method. The flow conditions and vessel geometry are chosen to mimic flow in the CCA. Results of the velocity profile measurements are compared with CFD calculations. Finally, the  $\cos \theta$ -method is applied to estimate the volume flow from the asymmetric axial velocity profiles. The results are compared with the presently applied Poiseuille and Womersley approximations. Furthermore, an analysis of the sensitivity of the integration methods to the exact orientation of the measured velocity profile in the cross section of the artery is analysed by means of a CFD-based analysis.

## 5.2 Material and methods

### 5.2.1 Experimental setup

In the experimental setup (Figure 5.1), a fluid, mimicking the acoustic and rheological properties of blood was pumped from a reservoir through a compliant tube, which mimics the blood vessel. A polyurethane tube (HemoLab, Eindhoven, The Netherlands) with a radius,  $a$ , of 4 mm and a wall thickness of 0.1 mm was applied to mimic the common carotid artery (CCA). The polyurethane tube consisted of multiple straight and curved segments with a length of about 30 cm, produced with a spin coating method, which were smoothly glued together, resulting in a tube with a straight inlet and outlet section and a single curved centre section. Vessels with a curved section with a radius of curvature,  $R$ , of 20 cm and 40 cm were produced. This corresponds respectively to a curvature ratio,  $\delta = a/R$ , of 0.01 and 0.02. The phantom vessel was fully submerged in a reservoir of water to prevent the vessel to deform under influence of gravity. The curved section was positioned in a horizontal plane to prevent influence of gravity on the flow. Additionally, the water acted as a conductor of sound. The tube was terminated by a resistance, from which the fluid flowed back to the reservoir. For the terminal impedance, a Windkessel model was applied. The viscous dissipation in the distal vessel,  $R_s$ , and the viscous dissipation in the distal capillary bed  $R_p$ , were modelled by local narrowing, the compliance of the arterial system,  $C$  was modelled by an air-chamber.

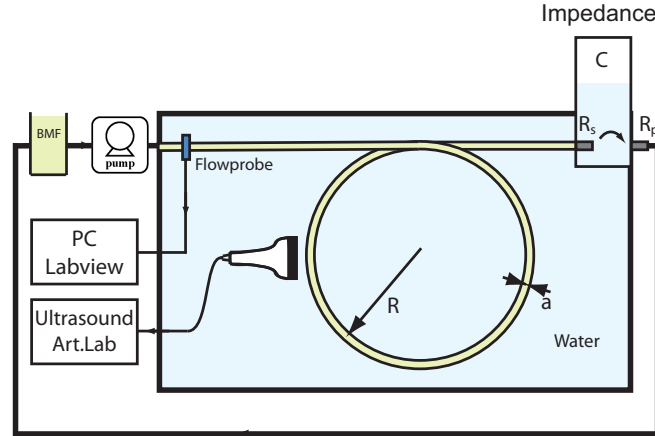


Figure 5.1: Schematic overview of the experimental setup

The flow was generated by combining a stationary pump and a servo-actuator operated piston pump (indicated in Figure 5.1 by a single symbol). The stationary pump (Pacific Scientific, IL, USA) was manually set to a specific flow rate,

whereas the trajectory of the piston pump (home developed) was computer controlled using LabView software (National Instruments, Austin, TX, USA). To ensure a developed velocity distribution at the measurement site, the ultrasound probe was positioned at  $270^\circ$  from the inlet of the curve. The ultrasound probe was accurately positioned in the symmetry plane of the curve, perpendicular to the polyurethane tube, by means of a 3D manipulator, such that the mechanical focus of the probe was located at the centre of the vessel. To maximize the signal level, the electrical focus was set equal to the mechanical focus. At about 1 cm upstream of the ultrasound probe, an ultrasonic flow probe (10PAA, Transonic, NY, USA) was positioned to measure the flow through the tube. The data from the flow probe measurements were acquired simultaneously with the data from the ultrasound scanner using a common trigger signal generated by a PC using the same LabVIEW data acquisition software.

### 5.2.2 Blood mimicking fluid

A shear thinning blood mimicking fluid (BMF), with both acoustical and rheological properties (Figure 5.2) similar to blood was used. The BMF consisted of a Xanthan gum (95465, Fluka, Buchs, Switzerland) solution fluid base, used to mimic the mechanical behaviour of blood, and polyamide particles (2001UD-NAT1, Orgasol, ELF Atochem, Paris, France), added to imitate the acoustical properties of blood (Ramnarine et al., 1998). The kinematic viscosity of the BMF, as measured as a function of shear rate with a Couette rheometer (Chapter 3) is presented in Figure 5.2. For a more elaborate description the reader is referred to Chapter 3.

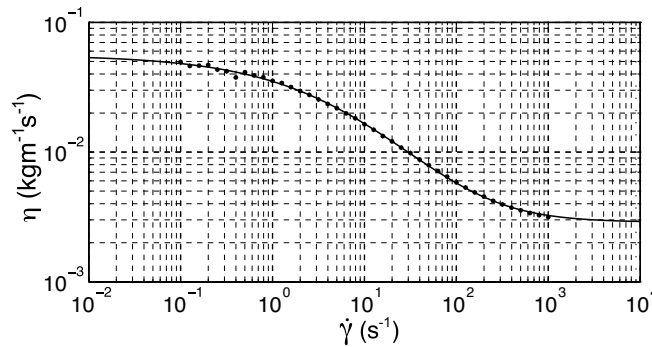


Figure 5.2: Shear thinning behaviour of the BMF, • indicates measurements, the solid line indicates the fit. This figure is identical to Figure 3.4.

Generally, scattering particles should be naturally buoyant with respect to the fluid base. This implies an accurate control of fluid density to prevent particles to sediment or float. Due to the shear thinning properties of the fluid base applied in

the BMF, sedimentation and floating of the particles is reduced since slow moving particles experience a relatively high drag force. This facilitates the application of the BMF in the experimental setup.

Mathematically, the shear thinning properties of the BMF are described using the Carreau-Yasuda model (Bird, 1987; Gijzen et al., 1999b):

$$\frac{\eta - \eta_\infty}{\eta_0 - \eta_\infty} = [1 + (\lambda\dot{\gamma})^b]^{(n-1)/b}, \quad (5.1)$$

with  $\eta_0$  the viscosity at low shear rate,  $\eta_\infty$  the viscosity at high shear rate,  $n$  the power-law constant and  $\lambda$  a time constant. This equation is identical to Equation 3.4 as introduced in Chapter 3. The parameter  $b$  determines the transition between the low-shear-rate region and the power-law region. The solid line in Figure 5.2 indicates the least squares fit of the Carreau-Yasuda model to the measured data.

### 5.2.3 Data acquisition

The commercially available Picus Art.Lab ultrasound system (ESAOTE Europe, Maastricht, The Netherlands) was used to collect the raw RF-data for offline processing. The system was equipped with a 7.5 MHz linear array transducer of 40 mm, consisting of 128 transducers. The RF data were sampled at 33 MHz ( $f_s$ ) and had an approximate centre frequency of 6.8 MHz and a quality factor of 2.

For the velocity profile measurements, the ultrasound system was operated in fast B-mode (also called multiple M-line mode), producing 14 M-mode lines, composing a single frame. To maximize the signal level at the focal point, the electrical focus is set equal to the mechanical focus, which was fixed at 2 cm from the transducer surface. The frame rate of the ultrasound system is determined by the number of M-lines and the pulse repetition frequency ( $f_{pr}$ ), the frequency at which individual M-mode lines are acquired, which depends on the maximum depth setting of the ultrasound system. For the velocity profile measurements, the depth was set to 50 mm, which resulted in a frame rate,  $f$ , of 730 s<sup>-1</sup> and a field of view of 4.4 × 50.0 mm. The maximum measurement time was hardware limited to about 3.8 seconds. The RF data matrix obtained from the system was a 3D function of depth ( $r$ ), time ( $t$ ) and position along the probe ( $z$ ).

### 5.2.4 Data processing

The RF data were processed on a PC and computations were performed with Matlab (The MathWorks, Natick, MA, USA). After removal of the DC component of the RF signals, a 4th order Butterworth band pass filter (4.2 MHz and 12.5

MHz) was applied. For each data point, a 4th order 20 Hz Butterworth high pass filter was applied in the temporal direction to suppress static and slow moving objects (e.g. wall reverberations).

After identification of the vessel-lumen interface by means of a sustain attack filter (Meinders et al., 2001), data windows of  $4.4(z) \times 0.2(r)$  mm at 50% overlap were applied to the filtered RF data. The cross correlation based UPV method, as introduced in Chapter 3, was applied to assess the axial velocity distribution of the flow through the tube. This resulted in 2816 instantaneous velocity profile estimations, sampled at 730 Hz.

### 5.2.5 Velocity assessment

The stationary flow was generated with a constant head system positioned between the stationary pump and the inlet of the phantom vessel to attenuate possible flow oscillations caused by the stationary pump. By varying the resistance at the outlet of the phantom vessel, stationary flow rates varying from  $0.15 \text{ lmin}^{-1}$  to  $1.15 \text{ lmin}^{-1}$  were generated, which corresponded to  $50 < Re < 520$ , in which the Reynolds number,  $Re$ , is defined as:

$$Re = \frac{2a\bar{v}\rho}{\eta(\dot{\gamma}_{char})}, \quad (5.2)$$

where  $\bar{v}$  is the average axial velocity and  $\rho$  the BMF density. The effect of the non-Newtonian properties of the BMF was taken into account by incorporating the viscosity at the characteristic shear rate:  $\eta = \dot{\eta}(\dot{\gamma}_{char})$ . The characteristic shear rate (Gijzen et al., 1999b) was defined here as

$$\dot{\gamma}_{char} = \frac{2Q}{\pi a^3}, \quad (5.3)$$

in which  $Q$  is flow through the vessel and  $a$ , the radius of the vessel. Flow in curved geometries is characterized by the Dean number:

$$D = 4Re\sqrt{2\delta}, \quad (5.4)$$

in which  $Re$  is the Reynolds number and  $\delta$  the curvature ratio. The flow in the tube with  $\delta = 0.01$  was characterized by a Dean number  $30 < D < 300$ , the tube with  $\delta = 0.02$ , by  $50 < D < 400$ . Volume flow rates were measured by means of the Transonic flow probe, which was calibrated before each measurement using a

stopwatch and a measuring beaker to collect steady flow. For each flow rate an ultrasound measurement was performed. The RF data were filtered as described in the previous section, subsequently the UPV method was applied. A median filter with a temporal and spatial window size of respectively,  $4 \cdot 10^{-3}$  s and  $6.9 \cdot 10^{-5}$  m, was applied to remove outliers.

For the non-stationary flow measurements, a pulsatile flow waveform (see Figure 5.8) with a cycle time of 1 s, a mean of  $0.7 \text{ lmin}^{-1}$  and a peak flow of about  $1.6 \text{ lmin}^{-1}$  was generated by superimposing a flow pulse of the piston pump on a stationary flow component generated by the stationary pump. The resistance at the outlet was set high enough to prevent collapse of the vessel and low enough to induce low pressures, leading to negligibly small vessel wall motion and deformation. The stationary flow measurement was performed using the  $\delta = 0.02$  geometry. To circumvent too large displacements of the tube due to the pulsatile pressure wave, the curved section of the vessel was fixed in space by placing the tube in an agar gel (1 wt% agar in water).

The generated flow waveform corresponded to physiologically relevant average and peak Reynolds numbers, equal to 300 and 900 respectively (Ku, 1983). For the flow in the curved section this corresponded to an average and peak Dean number, equal to 240 and 720 respectively. For the calculation of the Womersley parameter,  $\alpha = a\sqrt{\omega\rho/\eta}$ , it was assumed that  $\eta = \eta(\dot{\gamma}_{char}) = \eta(\frac{2Q}{\pi a^3}) \approx 5 \cdot 10^{-3} \text{ kgm}^{-1}\text{s}^{-1}$ . For the first harmonic, the Womersley parameter was found to be 4.5.

Using LabVIEW, the piston pump was programmed to generate 30 beats. Simultaneously, the flow was measured and a trigger signal was generated. During these 30 beats, 3.8 seconds of fast B-mode RF data were obtained for offline processing. The trigger signal was used to synchronize the flow measurement with the RF-data. The RF-data were filtered as described in the previous section. A median filter with a temporal and spatial window size of respectively,  $4 \cdot 10^{-3}$  s and  $6.9 \cdot 10^{-5}$  m, was applied to remove outliers. A low pass, zero-phase Butterworth filter with a cutoff frequency of 40 Hz was applied to suppress high frequency noise.

A finite-element CFD model of a rigid walled curved vessel (Beulen et al., 2009; van de Vosse et al., 2003) (Chapter 2) was applied to calculate the time-dependent velocity distribution across the vessel. The shear rate dependency of the viscosity was incorporated by implementing the Carreau-Yasuda model (5.1), using the parameters that were presented in Table 3.1. For the boundary conditions, at the inlet, the flow as assessed in the experiments was prescribed. At the walls, the no-slip boundary condition was applied. The results of the instantaneous velocity profile measurements were compared with the CFD computations.

### 5.2.6 Flow assessment

Volume flow was estimated from the measured axial velocity profiles by application of the  $\cos \theta$ -method (Chapter 4) and the Poiseuille and Womersley approximations. For the  $\cos \theta$ -method, the measured velocity profile was divided into two equal parts at the centreline. Each part of the profile was integrated over half of the surface of the tube, based on the measured radius, as if it were an axis-symmetric profile (Figure 5.8). The volume flow was approximated by summation of both contributions:

$$Q = \pi \int_0^a v^+(r) r dr + \pi \int_0^a v^-(r) r dr. \quad (5.5)$$

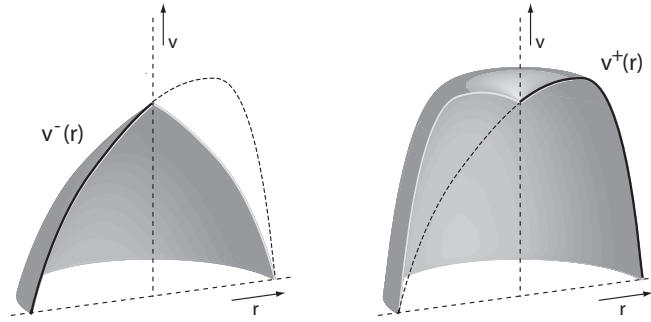


Figure 5.3: Schematic explanation of the integration method: the measured axial velocity profile is divided into two equal parts at the centreline,  $v^-(r)$  (left) and  $v^+(r)$  (right). Each part is integrated over half the surface of the tube as if it were an axis-symmetric profile. The volume flow is approximated by summation of both contributions.

For Doppler velocity measurements, the exact position of the vessel walls, and thus the position of the centre of the vessel, are not known. For that reason it is often assumed that the centreline velocity is equal to the maximum velocity measured over the cross section of the artery (Fraser et al., 2008). Accordingly, for the Poiseuille approximation, the measured velocity profile was approximated by a parabolic velocity profile with a maximum velocity equal to the measured maximum velocity. For the Womersley approximation, the inverse Womersley method (Cezeaux and Grondelle, 1997) was applied to determine the flow rate from the measured maximum velocity. All three flow approximations were compared to the flow as assessed directly during the measurement.

### 5.2.7 Sensitivity Analysis

For application of the flow approximation methods it is frequently assumed that the acquired velocity distribution is obtained by measuring exactly through the centre of the vessel. However, in clinical practice, the exact orientation of the ultrasound beam, with respect to the cross section of the vessel, is not known and varies for each measurement. Depending on the shape of the velocity distribution and the approximation method applied, these uncertainties in positioning can result in significant misestimates in the flow deduced. In order to obtain an estimate of these deviations, the Poiseuille, Womersley and  $\cos \theta$  flow approximation methods were applied to CFD derived velocity profiles. Contrary to an experimental investigation of the sensitivity, a CFD based analysis allows to eliminate the influence of measurement errors in velocity profile and probe positioning on the flow approximations and thus allows to solely focus on the performance of the approximation methods.

At the inlet of the CFD model, the flow, as assessed in the non-stationary flow experiment, was prescribed, at the walls, the no-slip boundary condition was applied. It is assumed that the velocity profile is measured over a line oriented at an angle  $\Phi$  with respect to the symmetry plane ( $\theta = 0$ ) at a distance  $d$  from the centre of the cross section, perpendicularly positioned to the centre line of the vessel (Figure 5.4). In this analysis, the cross-section of the ultrasound beam is assumed to be constant and negligibly small.

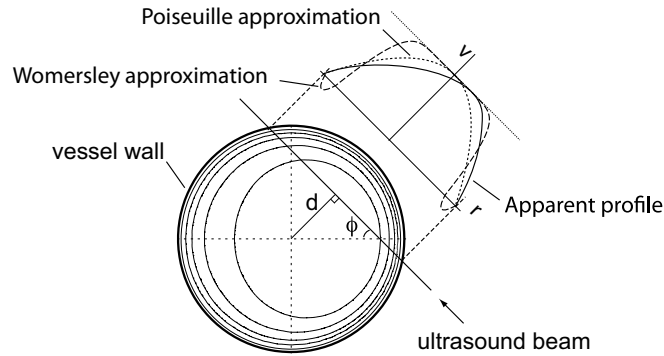


Figure 5.4: Schematic overview showing the apparent velocity profile (input for the  $\cos \theta$ -approximation) and the Poiseuille and Womersley approximations (based on the apparent maximum velocity) for an axial velocity assessment for which the ultrasound beam crosses the vessel at an angle  $\Phi$  and a distance  $d$ , perpendicularly to the centerline.

The velocity profile was determined for  $0 \leq \Phi \leq 2\pi$ , with steps of  $\pi/18$ , and  $0 \leq d \leq a/2$ , with steps of  $a/36$ . For each combination of  $\Phi$  and  $d$ , the apparent velocity profile was divided into two equal parts at the apparent centreline.

Subsequently, the  $\cos \theta$ -method was applied to determine the flow. Furthermore, the apparent maximum velocity was applied as an input for the Poiseuille and Womersley based approximations. After applying a low pass, zero phase Butterworth filter with a cutoff frequency of 40 Hz, the resulting flow waveforms were analysed by comparing the minimum, maximum and mean flow, pulsatility index and rise time to the corresponding properties of the prescribed flow waveform (Leguy et al., 2009). The pulsatility index was defined as the ratio of the difference between maximum and minimum flow and the temporal averaged flow. The rise time was defined as the time difference between the time-point with the maximum second derivative and the time-point with the maximum flow value. For the analysis it was assumed that differences less than 10 % between properties derived from the reference flow and integration based flow waveform were adequate for in-vivo application.

## 5.3 Results

### 5.3.1 Stationary flow

A comparison between the mean velocity profiles for the ultrasound measurement and the CFD solution of the velocity profile is presented in Figure 5.5. The results were non-dimensionalized by the radius,  $a$ , of the vessel. The ultrasound transducer was located at  $r/a \approx -5$ .

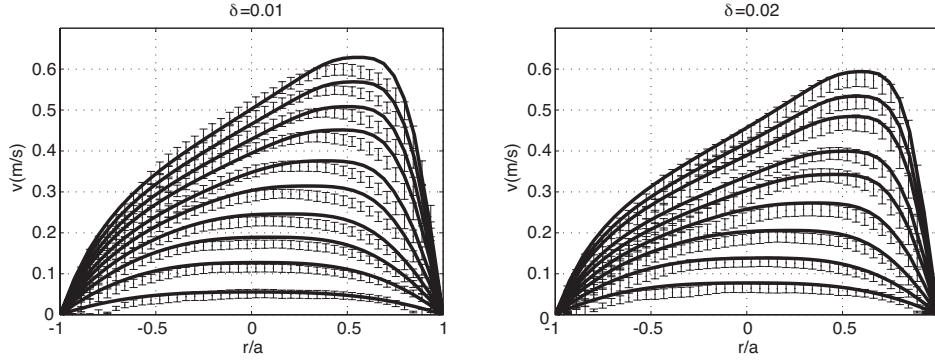


Figure 5.5: Comparison of the ultrasound measurement ( $\cdot$ ) and the CFD velocity profile ( $-$ ) for both the  $\delta = 0.01$  and  $\delta = 0.02$  geometry.

The measured velocity profiles agree quite well with the calculated velocity profiles. The root mean square value of the deviation between the measured and calculated velocity profile is on average  $1.7 \cdot 10^{-2} \text{ ms}^{-1}$  for the measurements performed in the  $\delta = 0.01$  geometry and  $2.4 \cdot 10^{-2} \text{ ms}^{-1}$  for the measurements performed in the  $\delta = 0.02$  geometry. For the  $\delta = 0.01$  geometry, the shift of the

maximum velocity towards the outside of the bend appears to be less pronounced for the measured profiles than for the calculated profiles.

The volume flow is estimated from the measured asymmetric axial velocity profiles by means of the  $\cos \theta$  and the Poiseuille flow estimation method. A comparison of the integration based flow estimates and the reference flow measurement by the flow probe for both the  $\delta = 0.01$  and  $\delta = 0.02$  geometry is presented in Figure 5.6.

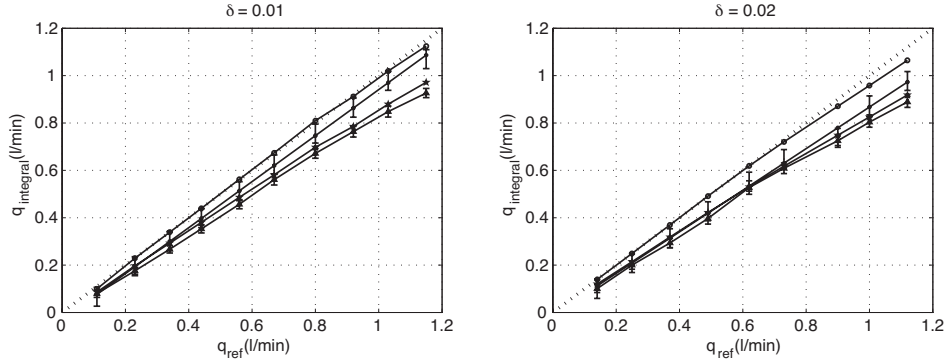


Figure 5.6: Comparison of the flow estimation based on the  $\cos \theta$  (\*) and the Poiseuille method ( $\triangle$ ) to the reference flow measurement for both the  $\delta = 0.01$  and  $\delta = 0.02$  geometry. Additionally, the flow is determined from the CFD calculated velocity profiles using the  $\cos \theta$  ( $\circ$ ) and the Poiseuille-method ( $\star$ ).

A linear fit shows that for the  $\delta = 0.01$  curved vessel, the ratio between the  $\cos \theta$ -based flow estimate and direct flow measurement equals  $0.97 \pm 0.03$ , with a constant flow underestimate of  $-0.03 \pm 0.03 \text{ lmin}^{-1}$ . For the  $\delta = 0.02$  curved vessel, the ratio between the  $\cos \theta$ -based flow estimate and direct flow measurement equals  $0.88 \pm 0.06$ , with a constant flow underestimate of  $-0.01 \pm 0.06 \text{ lmin}^{-1}$ . The CFD based flow estimates show that especially at high Dean and  $\delta$  the  $\cos \theta$  integration method slightly underestimates the flow (about 5% for  $q_{ref} \approx 1.1 \text{ lmin}^{-1}$ ). At low flow rates, the deviation is negligible. At the lowest flow rates, the deviations found for the Poiseuille approximation are comparable to the deviations found for the  $\cos \theta$  method. However, for the Poiseuille approximation, these deviations increase to 20% for the high flow rates ( $q_{ref} \approx 1.1 \text{ lmin}^{-1}$ ).

### 5.3.2 Non-stationary flow

A comparison between the instantaneous velocity profile measurement and the CFD solution of the velocity profile is presented in Figure 5.8. The velocity profiles are shown for 8 distinct phases in the period in Figure 5.7. The results are non-dimensionalized by the radius,  $a$  of the vessel. Again, the ultrasound transducer was located at  $r/a \approx -5$

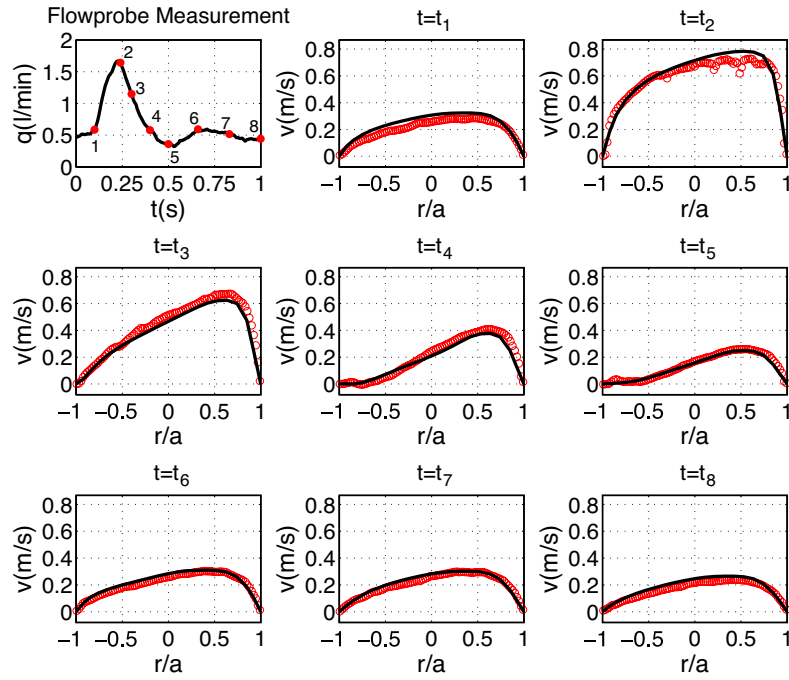


Figure 5.7: Comparison of the ultrasound measurement and the calculated velocity profile ( $\circ$ , ultrasound measurement;  $-$ , CFD calculation).

Overall, the measurements agree very well with the calculated profiles, although some deviations occur at peak systole. The volume flow is estimated from the measured asymmetric axial velocity profiles by means of the  $\cos \theta$ -method, the Poiseuille and Womersley approximations.

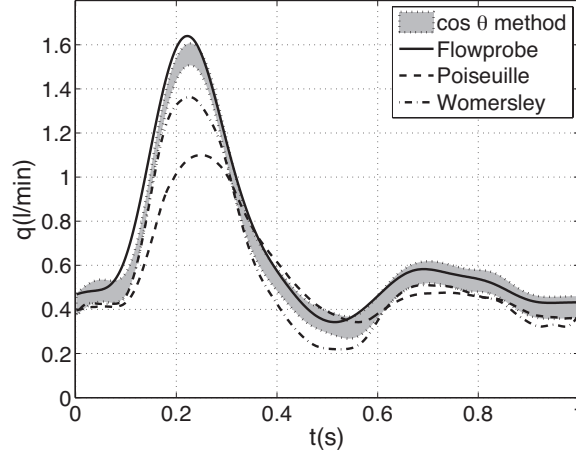


Figure 5.8: Comparison between the flow probe measurement and the  $\cos \theta$ , Poiseuille and Womersley based flow approximations.

The  $\cos \theta$ -based flow approximation agrees well with the reference flow, although some deviation occurs in the systolic peak. The Poiseuille and Womersley based flow approximations clearly underestimate the flow, especially in peak systole.

### 5.3.3 Sensitivity analysis

The results of the comparison of the minimum, maximum and mean flow and the pulsatility index between reference flow waveform and integration based flow waveform (Figure 5.9, 5.10 and 5.11) show the absolute percentual deviation between reference and integration based flow waveform for the previous mentioned properties for different combination of angle,  $\Phi$ , and offset,  $d$ . Regions with an absolute deviation above 10 % are shaded.

The contour plots in Figure 5.9 indicate that for the  $\cos \theta$ -method,  $Q_{min}$ ,  $Q_{mean}$  and the pulsatility index can be assessed with an estimation error of less than 10% for the major part of the  $(\Phi, d)$ -space. However, the estimation of the maximum flow,  $Q_{max}$ , is found to be more sensitive for increasing  $d$ : for  $d > a/10$ , the deviation is already higher than 10%.

The contour plots presented in Figure 5.10 and 5.11 show that both the Poiseuille and Womersley approximation can only be applied to adequately assess the minimum flow. For the maximum and mean flow and the pulsatility index, deviations

between reference flow and integration based flow are above 10 % for the major part of the  $(\Phi, d)$ -space.

For the rise time it is found that for the  $\cos \theta$ -method the mean deviation is 4% (max 8%) compared to respectively 1% (max 8%) and 6% (max 15%) for the Poiseuille and Womersley approximations with respect to the reference flow.

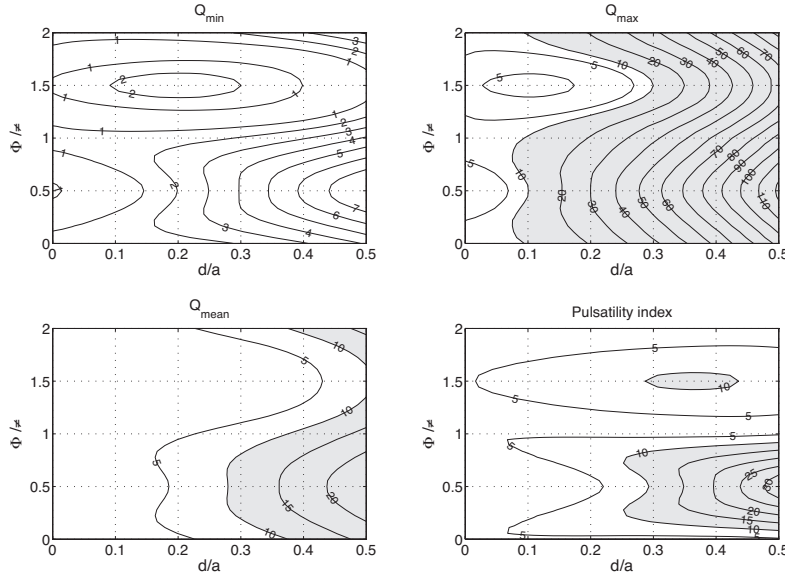


Figure 5.9: Absolute deviation between the reference flow and the  $\cos \theta$ -based flow estimate for offset  $d$  and angle  $\Phi$ . Deviations are expressed in percentages, regions with deviations larger than 10% are shaded.

## 5.4 Discussion

For the stationary flow measurements, the shift of the maximum velocity towards the outside of the bend appears to be less pronounced for the measured profiles than for the calculated profiles. This deviation can be caused by the fact that the flow is not able to develop fully in the  $\delta = 0.01$  geometry. It is difficult to position the curved sections of the vessel exactly in a horizontal plane, especially for the  $\delta = 0.01$  geometry. Small vertical deviations from the horizontal plane can already result in local vertical deviations which are in the same order as the curvature of the vessel. This prevents full flow development and can cause deviations from the CFD-calculated profiles. Additionally, for this weakly curved geometry, the measurement location might be not far enough from the entrance of the curved section to observe fully developed flow.

Overall, the deviations found between calculated and measured velocity profiles

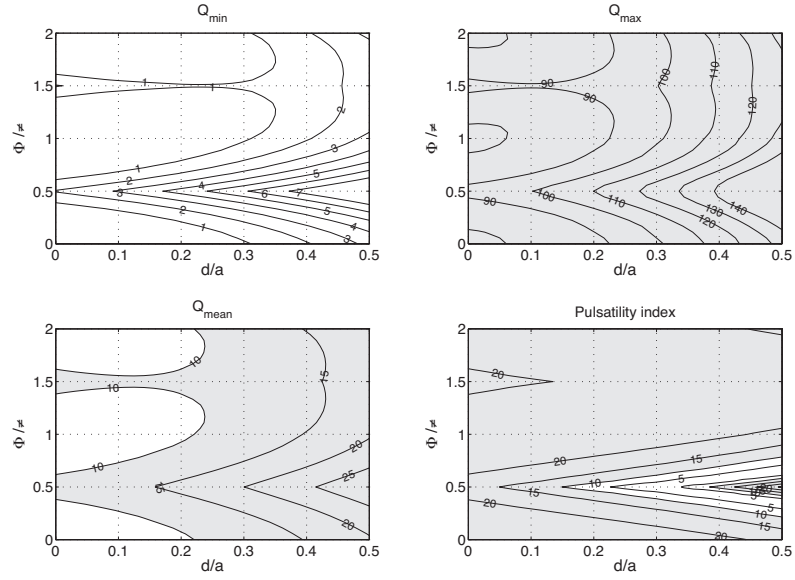


Figure 5.10: Absolute deviation between the reference flow and Poiseuille based flow estimate for offset  $d$  and angle  $\Phi$ . Deviations are expressed in percentages, regions with deviations larger than 10% are shaded.

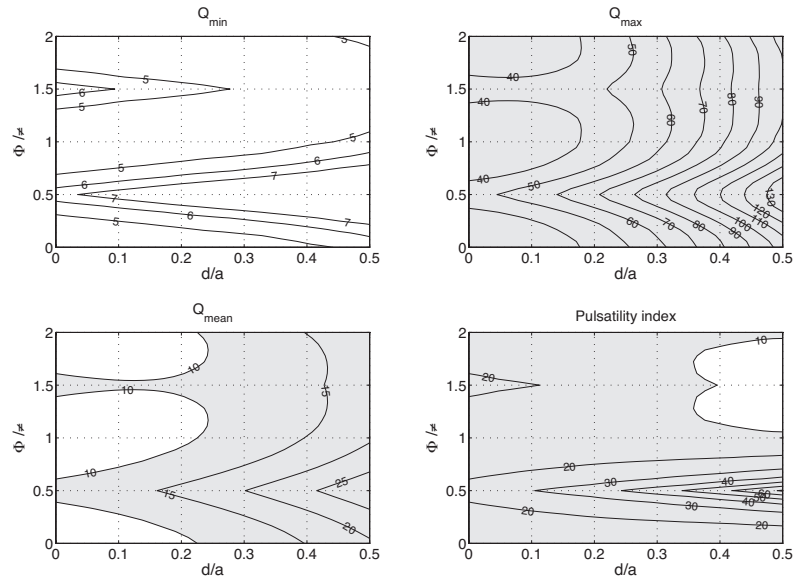


Figure 5.11: Absolute deviation between the reference flow and Womersley based flow estimate for offset  $d$  and angle  $\Phi$ . Deviations are expressed in percentages, regions with deviations larger than 10% are shaded.

are comparable to the deviations found between calculated and measured velocity profiles in straight geometries (Chapter 3). Both for the  $\delta = 0.01$  and  $\delta = 0.02$  geometry, the deviation between the velocity profile measurements and calculated velocity profile increases in the near-wall region,  $0.9 < |r|/a < 1.0$  and especially near the anterior wall ( $r/a = -1$ ), probably due to the fact that the signal of the wall dominates the scattering signal in this region. Additionally, the high spatial velocity gradients can cause a decrease in accuracy of the velocity estimation. Furthermore, a small misestimate of the rheologic properties of the BMF can have a significant influence in the near wall region, since close to the wall, the shear rate increases dramatically. This causes deviations in the calculated velocity profile, especially in the near wall region.

For the measurements performed in the  $\delta = 0.01$  geometry, the  $\cos \theta$ -method proves to be quite accurate, with an average deviation of 3% with respect to the reference flow. For the measurements performed in the  $\delta = 0.02$  geometry this deviation increases to 12%. Deviations found between  $\cos \theta$ -approximation and reference flow are comparable to the deviations reported by Verkaik et al. (2009) for Newtonian flow. The  $\cos \theta$ -method is found to provide a much more accurate flow estimate than the Poiseuille approximation, especially for high flow rates (increasing Dean number) and increasing  $\delta$ . This is to be expected, since the Poiseuille method offers a bad approximation for the flattened velocity profiles that occur for shear thinning fluids.

The analysis of the velocity profiles calculated by the CFD model, has shown that the maximum deviation with respect to the reference flow, induced by the  $\cos \theta$ -method is about 5% for the examined flow rates. The larger deviation found in the measurements (12% for the  $\delta = 0.02$  geometry) can be caused by errors in the measured axial velocity profile. This can be expected from the cross-correlation algorithm since for each data window the average velocity is determined, in the case of large radial velocity gradients this can result in an underestimate of the velocity. Furthermore, close to the wall, the velocity profiles are distorted by the vicinity of the wall, also causing an underestimation of the velocity and thus an underestimation of the flow. Additionally, transverse velocity components, such as secondary velocity components which especially occur in curved vessels, can have a slight influence on the performance of the cross correlation based velocity estimate.

For the non-stationary flow measurements, the comparison between the velocity profile measurements and CFD computations shows that the cross correlation based ultrasonic perpendicular velocimetry is able to cope with the relatively high temporal and spatial velocity gradients which occur in non-stationary flow in curved vessels, allowing an accurate assessment of axial velocity distribution for non-stationary flow in curved vessels. No beat to beat averaging is required to acquire usable velocity profiles.

In the systolic peak, the velocity is slightly underestimated. It appears as if a cut off for the maximum velocity occurs. This is probably caused by the fact that the displacement between two successive fast B-mode frames is too large. According to

the one-quarter rule (Keane and Adrian, 1992), the maximum axial displacement of particles in two successive frames is  $W_{FOV}/4$ , in which  $W_{FOV}$  is the width of the field of view. For ultrasound cross correlation based measurements (Liu et al., 2008), this results in a maximum axial velocity equal to:

$$v_{max} \approx \frac{fW_{FOV}}{4}. \quad (5.6)$$

For the ultrasound system employed in this research,  $f$  is equal to 730 Hz, resulting in  $v_{max} \approx 0.8 \text{ ms}^{-1}$ , which is about equal to the cutoff value found in the velocity measurements. The only possibility to increase the maximum measurable velocity, without decreasing the axial resolution (increasing  $W_{FOV}$ ), is to increase  $f$ . Considering the rapid development of ultrasound systems, it is to be expected that in near future ultrasound systems with increased frame rate will allow the assessment of higher maximum velocities.

Although the  $\cos \theta$ -method was derived for flow estimation for stationary Newtonian flow through weakly curved vessels, it is found that this method is also successfully applicable to non-Newtonian flow for physiologically relevant flow and geometries. The average deviation between the  $\cos \theta$ -integration based flow estimate and the reference flow is about 5% (max about 20%), compared to an average deviation of 20% (max about 40%) for both the Poiseuille and Womersley approximations.

For a successful clinical application it is required that the flow estimation method is not too sensitive to the exact orientation of the measured velocity profile with respect to the centre line of the cross section. The sensitivity analysis shows that the considered approximation methods can all be successfully applied to estimate the minimum flow rate with an error of less than 10%. However, only the  $\cos \theta$ -method is able to estimate the maximum, minimum and mean flow rate and the pulsatility index with an estimation error of less than 10%.

For the  $\cos \theta$ -method it was found that in order to obtain an error of less than 10% in minimum flow, mean flow and pulsatility index, the beam should be positioned at  $d < a/4$ . For the maximum flow estimate is found that the exact positioning is more strict: for  $d > a/10$ , the deviation is already higher than 10%. An experienced ultrasound operator should be able to locate the centre of a vessel within a 10% accuracy by finding the maximum possible vessel diameter and/or the maximum signal. This allows the  $\cos \theta$ -method to be applied for an accurate flow estimation. It should be noted that in practice, the ultrasound beam has a finite cross section. As a result, the estimated velocity always represents an average velocity over a certain measurement volume.

## 5.5 Conclusion

The UPV method has been applied for an accurate assessment of the axial velocity profile for both steady and un-steady non-Newtonian flow in weakly curved vessels in a phantom setup. A comparison between measurements and CFD calculations of the velocity profile shows that the UPV-model allows an accurate assessment of the axial velocity distribution. The deviation between the time averaged ultrasound velocity profile measurement and the CFD solution is on average about  $2 \text{ cm s}^{-1}$ .

For flow estimation, the  $\cos \theta$ -method, Poiseuille and Womersley approximation have been applied to the measured velocity profiles. For stationary flow, the maximal deviation of the  $\cos \theta$ -method derived flow rate compared to the reference flow is 12% whereas the Poiseuille approximation results in deviations up to 20%. For non-stationary flow, the average error between the  $\cos \theta$ -integration based flow estimate and reference flow is about 5%, compared to an average deviation of 20% for both the Poiseuille and Womersley approximations.

A CFD-based comparison of the Poiseuille, Womersley and  $\cos \theta$ -integration methods indicates the Poiseuille and Womersley methods can only be applied to accurately assess minimum flow (error  $< 10\%$ ). The  $\cos \theta$ -method however, is found to allow accurate (error  $< 10\%$ ) assessment of the minimum, mean and maximum flow for velocity profiles assessed at  $d < a/10$  from the centreline, independent on the angle  $\Phi$ .

Overall, ultrasonic perpendicular velocimetry, combined with the  $\cos \theta$ -integration method, proves to provide an accurate flow estimation for flow in slightly curved arteries such as the common carotid artery (CCA). Furthermore, the results show that an accurate flow estimation is feasible, independent on the orientation of the measured velocity profile with respect to the plane of symmetry, even when not exactly measured through the centreline of the vessel. The study shows that ultrasonic perpendicular velocity assessment method combined with the  $\cos \theta$ -method could be a valuable asset for accurate flow assessment in superficial arteries such as the brachial artery and the CCA.



## **Chapter 6**

# **Towards a non-invasive pressure assessment**

## 6.1 Introduction

Diseases involving the heart and blood vessels (arteries and veins), often referred to as cardiovascular disease (CVD), are a common cause of death in adults in the western society (Petersen et al., 2005). The most common type of CVD is atherosclerosis, a disease in which, locally, plaques build up at the inside of arteries, resulting in a decrease of vessel compliance, causing an elevated pressure. At a later stage, the plaques can rupture, causing local narrowing of the vessel lumen, or stenosis, resulting in an increased flow resistance, and consequently, a reduced, possibly insufficient, blood supply to the tissue and organs fed by the vessel.

In clinical practice, ultrasound is frequently applied to non-invasively assess blood velocity, blood volume flow and blood vessel wall properties such as vessel wall thickness and vessel diameter waveforms (Hoeks et al., 1990, 1997; Brands et al., 1999). To convert these properties into relevant biomechanical properties that are related to CVD, such as elastic modulus and compliance of the vessel wall (Reneman and Hoeks, 2000; Meinders et al., 2000; Wilson et al., 1995), local pressure has to be assessed simultaneously with vessel wall thickness and vessel diameter waveforms. Additionally, accurate estimates of vascular impedance (transfer function between pressure and blood flow) can be a valuable tool for the estimation of the condition of the vessel, e.g., to diagnose stenosis. Studies of arterial impedance in humans, however, are hampered by the lack of reliable non-invasive techniques to simultaneously record pressure and flow locally as a function of time. Local pressure assessment has great potential for improving the ability to diagnose and monitor CVD.

The most straightforward approach to estimate local pressure would be to insert a pressure catheter into the artery under investigation. However, this influences local flow and geometry, and most importantly, for routine examination, a non-invasive method is highly preferred. Non-invasively, the pressure can only be estimated reliably at a few arterial locations, e.g. in the radial and digital artery, by performing a tonometer measurement. Pressure waveforms estimated at such locations might be applied as a substitute for the local pressure at a location where a non-invasive estimation is impossible. However, this is only an approximation, since the pressure waveform changes with location in the arterial tree (McDonald, 1974). Additionally, the assessment at two locations results in phase errors (Hoeks et al., 2000). It has been suggested to use a transfer function to derive the central pressure from the peripheral one (Chen et al., 1997). Although the use of a transfer function has proven to be useful (Milasseau et al., 2000; O'Rourke, 1999), it has the inherent problem that vascular parameters (mainly diameter and compliance) of individuals should match that of a reference population (Hoeks et al., 2003), whereas all available data indicate that the dynamic characteristics of central arteries depend on age and vascular condition. Additionally, the phase difference between diameter and pressure still remains. Deriving the blood pressure waveform from the diameter waveform circumvents the introduction of possible phase differences and avoids the use of generalized transfer

functions (Meinders and Hoeks, 2004). By simply calibrating the mean and minimum arterial diameter to end diastolic and mean pressure, errors in carotid pulse pressure of only 1.6 mmHg were obtained (van Bortel et al., 2001), despite the linear relationship assumed between diameter and pressure. In the method developed by Meinders and Hoeks (2004), a more realistic exponential relationship between arterial cross section and pressure (van Loon et al., 1977; Hayashi et al., 1980; Powalowski and Pensko, 1988) is assumed to increase accuracy.

Although the above described methods allow an accurate estimation of local pressure, these methods still consist of the assessment of a waveform closely related to pressure which is subsequently scaled by an additional direct pressure measurement to gain a pressure estimate. However, direct local pressure estimation by a single measurement is preferable. This can be established by combining knowledge of the mechanical behaviour of the arterial wall with an assessment of vessel wall motion. Due to periodic volume ejection of blood from the heart into the elastic arteries, pressure and flow waves travel through the arterial system. Waves propagate from the heart to the periphery, but also, reflected waves travel from the periphery back to the heart (Westerhof et al., 1972). The speed at which these flow and pressure pulses travel, the pulse wave velocity (PWV),  $c$ , is related to the mechanical properties of the vessel by:

$$c = \sqrt{\frac{A}{\rho} \frac{dp}{dA}} = \sqrt{\frac{A}{\rho} \frac{1}{C}} \quad \text{with} \quad C = dA/dp \quad (6.1)$$

which is a function of the cross sectional area of the artery,  $A$ , the density of the blood  $\rho$  and the compliance of the artery,  $C$  (Milnor, 1989; McDonald, 1974). From (6.1) it can be derived that the local pressure,  $p(t)$ , with respect to an unknown constant pressure offset,  $p_0$ , is given by:

$$p(t) - p_0 = \int_{A(0)}^{A(t)} C dA = \int_{A(0)}^{A(t)} \frac{A}{\rho c^2} dA, \quad (6.2)$$

from which follows that local pressure can be estimated from a simultaneous assessment of vessel cross-sectional area and PWV.

Estimation of PWV can either be performed globally or locally. In the global approach, the transit time over a long trajectory of the arterial tree, often composed of both elastic and muscular arteries, is measured, resulting in an average PWV. Therefore, PWV is preferably assessed over a short segment of an artery, thus allowing estimation of local instead of average material properties. In a reflection free system, the local PWV can be obtained from two pressure measurements, one at either end of the segment of interest. However, when reflections are present, the reflected waves will affect the measurement, resulting in an apparent PWV estimate. To resolve this problem, (Taylor, 1959) developed a method in which

a third pressure measurement is added, located half way between the two existing measurement positions, which allows to estimate the true PWV. Bertram et al. (1997) applied the 2 and 3-point methods to pressure signals, acquired both in-vivo and in an experimental setup, and showed that accurate estimation of PWV in the presence of reflections by means of the 3-point method is possible. Cross correlation based methods, in which the time shift between signals, e.g. vessel wall velocity (Struijk et al., 1992), assessed at two measurement locations, is determined, are also hampered by the presence of reflections. However, the influence of reflections can be minimized by looking at characteristic points in the waveform which are not too much influenced by reflections, e.g. the systolic foot (McDonald, 1974; Hermeling et al., 2007).

A few methods exist in which the PWV can be estimated during the reflection free period of the cardiac cycle, e.g., at the start of systole. The method of characteristics (Parker and Jones, 1990), which is based on the one-dimensional equations of flow in elastic tubes without viscous losses, shows that changes in pressure,  $dp$ , are related to changes in velocity,  $dU$ , by means of the 'water hammer' equation:  $dp_{\pm} = \pm \rho c dU_{\pm}$ , in which the '+' sign refers to forward travelling waves and the '-' sign refers to backward waves. For reflection-free periods, this indicates a linear relation between pressure and average velocity. This allows to straightforwardly identify the reflection-free period in a PU-loop and subsequently to easily estimate the PWV (Khir et al., 2001). However, this requires a simultaneous assessment of blood flow and pressure, acquired using equipment with similar frequency characteristics (Hoeks et al., 2000). Since, in this research, the aim is to estimate pressure based on PWV-assessment, this method for PWV estimation is not usable. However, Rabben et al. (2004) proposed a similar method, the QA-method, in which the local PWV in the artery is estimated during a reflection free period of the cardiac cycle as the ratio between the change in flow and the change in cross-sectional area. Again, the reflection free period can be easily identified by a linear section in the QA-loop. In the absence of reflections, the characteristic impedance,  $Z_c$ , is related to compliance,  $C$ , cross sectional area,  $A_0$ , and volume flow,  $Q$ , by:

$$Z_c = \frac{dp}{dQ} = \frac{dp}{dA} \frac{dA}{dQ} = \frac{1}{C} \frac{dA}{dQ}. \quad (6.3)$$

Additionally, the solution from the one-dimensional wave equation (Milnor, 1989) shows that the characteristic impedance is also related to distensibility by:

$$Z_c = \sqrt{\frac{\rho}{A} \frac{1}{C}}. \quad (6.4)$$

By multiplying (6.1) and (6.4) and subsequently inserting (6.3), it can be shown

that the PWV is given by:

$$c = \frac{dQ}{dA}. \quad (6.5)$$

In the study by Rabben et al. (2004), the cross sectional area was estimated from M-mode data (Rabben et al., 2002) by assuming an axi-symmetric geometry. The flow was determined from a Doppler ultrasound velocity measurement, acquired at the same position as the M-mode data, by application of Womersley theory for pulsatile flow in straight tubes (Womersley, 1955). Vessel wall diameter and blood velocity were acquired subsequently and several cardiac cycles were averaged in order to obtain smooth diameter and flow waveforms. As a result, temporal misalignment between the area and flow curves can result in errors in the PWV estimate. Williams et al. (2005, 2007) estimated both flow and diameter waveforms from color flow coded B-mode images, circumventing temporal misalignment errors. However, the assessed flow waveforms were scaled afterwards using an additional Doppler measurement. Additionally, the determination of the vessel area, which also influences the flow, was affected by the insonation angle. The recently validated ultrasound velocity estimation technique (Chapter 3 and 5), combined with the  $\cos \theta$ -integration model (Verkaik et al., 2009) (Chapter 4), enables an accurate assessment of volume flow in both straight and curved vessels at high temporal resolution. Additionally, due to the applied perpendicular insonation angle of the ultrasound beam, the wall diameter of the vessel can be accurately assessed simultaneously, from the same measurement. This renders this technique promising for local PWV-assessment based on the QA-method, and subsequently pressure estimation by application of (6.2), allowing simultaneous flow and pressure estimation based on a single measurement. Additionally, application of the 3-point method to wall motion as assessed at several points along the vessel, by means of the linear array transducer, can be a promising method for PWV estimation. This method enables PWV estimation in the presence of reflections, circumventing the need to find reflection free periods in the cardiac cycle, subsequently resulting in a more straightforward and possibly more accurate PWV assessment.

The aim of this study is to evaluate the QA-method for local PWV assessment and subsequently local pressure estimation, based on perpendicular measurement of the flow and diameter waveforms. Additionally, it is looked into whether vessel wall motion can be applied as an input for PWV assessment by means of the 3-point method. Measurements are performed in a phantom setup. This allows to compare the estimated PWV, pressure and flow waveforms with corresponding values and waveforms obtained using reference measurements.

## 6.2 Material and methods

### 6.2.1 Wave propagation

The one-dimensional equations that describe the pressure and flow in distensible tubes can be derived by integrating the continuity and momentum equation over a cross section of the tube (Pedley, 1980). Under the assumption that the wave length is large compared to the diameter of the tube, that the phase velocity is large compared to the mean fluid velocity and that the wall motion is longitudinally constrained, the one dimensional mass and momentum equations are given by (Milnor, 1989):

$$\begin{aligned} C_0 \frac{\partial p}{\partial t} + \frac{\partial q}{\partial z} &= 0 \\ \rho \frac{\partial q}{\partial t} + A_0 \frac{\partial p}{\partial z} &= -f_0 q \end{aligned} \quad (6.6)$$

with  $f_0$  a friction function defined as:

$$f_0(\omega) = i\omega\rho \frac{F_{10}(\omega)}{1 - F_{10}(\omega)} \quad \text{with} \quad F_{10}(\alpha) = \frac{2J_1(i^{3/2}\alpha)}{i^{3/2}\alpha J_0(i^{3/2}\alpha)}. \quad (6.7)$$

$F_{10}(\alpha)$  is the Womersley function with  $J_0$  and  $J_1$ , Bessel functions of the first kind of order 0 and 1, in which  $\alpha$  is the Womersley parameter, defined as  $\alpha = \sqrt{\omega\rho/\eta}$ . Equations (6.6) can be solved in the frequency domain by substituting harmonic solutions:

$$p(\omega, z, t) = \hat{p}(\omega)e^{i(\omega t - kz)} \quad (6.8)$$

$$q(\omega, z, t) = \hat{q}(\omega)e^{i(\omega t - kz)} \quad (6.9)$$

where  $\hat{p}$  and  $\hat{q}$  are the complex amplitudes of the pressure and flow respectively, and  $k(\omega)$  is the complex wave number, defined as:

$$k(\omega) = \frac{\omega}{c} - i\frac{\gamma(\omega)}{\lambda}, \quad (6.10)$$

in which  $c$  denotes the phase velocity,  $\lambda = 2\pi c/\omega$  the wave length and the exponential decrease of the amplitude of the waves is described by the attenuation constant  $\gamma(\omega)$ .

Substitution of (6.8) and (6.9) in (6.6) yields:

$$\begin{aligned} i\omega C\hat{p} - ik(\omega)\hat{q} &= 0 \\ -ik(\omega)A_0\hat{p} + (i\omega\rho + f_0)\hat{q} &= 0, \end{aligned} \quad (6.11)$$

from which the following expression for the wave number  $k$  is found after setting the determinant of the resulting set equal to zero:

$$k(\omega) = \pm \frac{\omega}{c_0} \sqrt{\frac{1}{1 - F_{10}(\omega)}} = \pm k_0 \sqrt{\frac{1}{1 - F_{10}(\omega)}}, \quad (6.12)$$

in which  $c_0$  denotes the Moens-Korteweg wave speed, which is given by  $c_0 = \sqrt{A_0/\rho C}$ . Again, the wave number is complex. The phase velocity and attenuation constant are presented in Figure 6.1.

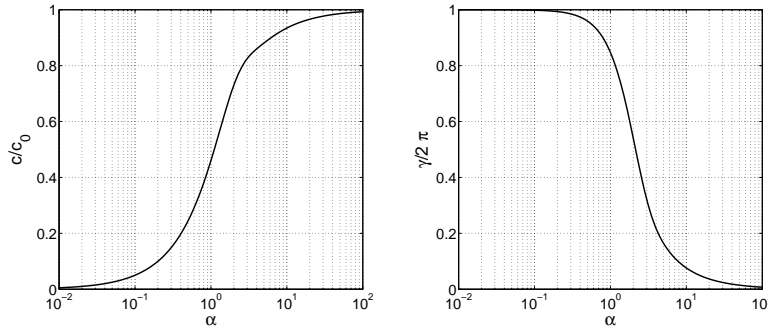


Figure 6.1: Phase velocity  $c/c_0$  and attenuation constant  $\gamma/2\pi$  as a function of  $\alpha$ .

For large Womersley numbers, the wave number  $k(\omega)$  is real, indicating that there is no attenuation, and the phase velocity equals the Moens-Korteweg wave speed.

## 6.2.2 Phantom setup

In a phantom setup (Figure 6.2), a shear thinning blood mimicking fluid (BMF) with both acoustical and mechanical properties similar to blood (Chapter 3), was pumped through a phantom vessel. A polyurethane tube with a radius,  $a$ , of

12.5 mm, a wall thickness of 0.1 mm and a length of about 1.5 m was used as a phantom vessel. The phantom vessel was fully submerged in a reservoir of water to prevent the vessel from deforming under influence of gravity. Additionally, the water acted as a conductor of sound.

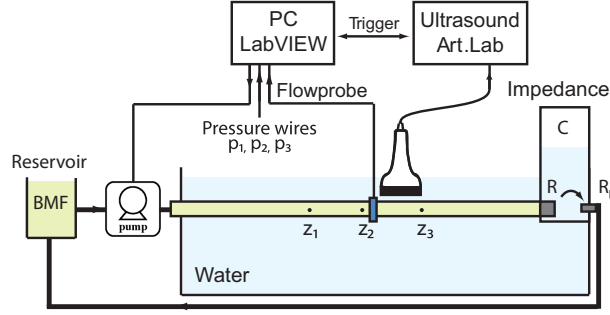


Figure 6.2: Schematic overview of the experimental setup.

At the inlet of the phantom vessel, a pulsatile flow waveform with a cycle time of 1 s, a mean of about  $0.7 \text{ lmin}^{-1}$  and a peak flow of about  $8 \text{ lmin}^{-1}$  was generated by means of a servo-actuator operated piston pump (home developed), from which the trajectory was computer controlled using LabView software (National Instruments, Austin, TX, USA). For the calculation of the Womersley parameter,  $\alpha$ , the viscosity at characteristic shear rate,  $\eta = \eta(\dot{\gamma}_{char}) = \eta(2\bar{Q}/\pi a^3)$ , was taken. The characteristic shear rate was based on a Poiseuille profile like in Gijssen et al. (1999b). For the first harmonic, the Womersley parameter,  $\alpha$ , was approximately equal to 10, from which according to the theory introduced in Section 6.2.1 it can be concluded that for the pressure waves travelling through the phantom setup, the PWV is approximately equal to the Moens-Korteweg wave speed.

The vessel was terminated by an impedance from which the BMF flows back through a reservoir, to the inlet of the pump. For the terminal impedance, a Windkessel model was applied. The viscous dissipation in the distal vessel,  $R$ , and the viscous dissipation in the distal capillary bed  $R_p$ , were modelled by local narrowing, the compliance of the arterial system,  $C$ , was modelled by an air-chamber. The impedance was set such that the maximum wall distension of the polyurethane tube was about 0.5 mm.

The ultrasound probe was positioned at about 0.75 m from the inlet of the tube, in perpendicular orientation with respect to the tube, such that the mechanical acoustic focus was at the centre of the vessel. At about 1 cm upstream of the ultrasound probe, an ultrasonic flow probe (10PAA, Transonic, NY, USA) was positioned to measure the flow through the tube. Three pressure wires (PressureWire, Radi, Uppsala, Sweden) were positioned at equidistant axial positions ( $z_1$ ,  $z_2$  and  $z_3$ ) inside the vessel. The centre pressure wire was positioned near the ultrasonic flow probe, the other two were positioned equidistantly at proximal and distal locations.

The data from the flow probe and pressure wires measurements were acquired simultaneously with the data from the ultrasound scanner using a common trigger

signal generated by a PC, using LabVIEW data acquisition software.

### 6.2.3 Data acquisition

The commercially available Picus Art.Lab ultrasound system (ESAOTE Europe, Maastricht, The Netherlands) was used to collect raw RF-data for offline processing. The system was equipped with a 7.5 MHz linear array transducer of 40 mm, consisting of 128 transducers. This results in a transducer pitch,  $\delta z_p$ , approximately equal to 0.3125 mm. The RF data were sampled at 33 MHz ( $f_s$ ) and had an approximate centre frequency of 6.8 MHz and a bandwidth of 4 MHz.

The ultrasound system was operated in fast B-mode (high frame rate B-mode), also called multiple M-line mode. In the fast B-mode, 14 M-mode lines are produced, composing a single frame. The distance between the employed M-lines is equidistant and can be set between a minimum value of  $\Delta z_p = 1 \times \delta z_p = 0.3125$  mm to a maximum of  $\Delta z_p = 3.5 \times \delta z_p = 1.0938$  mm. The frame rate of the ultrasound system is determined by the number of M-lines and the pulse repetition frequency, the frequency at which individual M-mode lines are acquired, which depends on the depth setting of ultrasound system. In this study, the depth was set to 50 mm, which resulted in an pulse repetition frequency  $f_{pr}$ , of 10211 Hz and a frame rate  $f$ , of 730 Hz. The maximum measurement time is hardware limited to about 3.8 seconds. The RF data matrix obtained from the system is a 3D function of depth ( $r$ ), time ( $t$ ) and position along the probe ( $z$ ). To maximize the signal level at the focal point, the electrical focus was set equal to the mechanical focus, which is fixed at 2 cm from the transducer surface.

### 6.2.4 Data processing

The RF data were processed on a PC using Matlab (The MathWorks, Natick, MA, USA). After removal of the DC component of the RF signals, a 4th order Butterworth band pass filter (4.2 MHz and 12.5 MHz) was applied.

For assessment of vessel wall position, the vessel-lumen interface was identified by means of a sustain attack filter (Meinders and Hoeks, 2004). Subsequently, the C3M estimator (Brands et al., 1997) was applied to assess the anterior and posterior wall velocity for each M-mode line. The dimensions of the data window for the C3M estimator had a temporal size of 50 ms at an overlap of 40 ms and a size in depth equal to 330  $\mu\text{m}$ .

For the flow estimation, a 4th order Butterworth high pass filter with a cutoff frequency of 20 Hz was applied in the temporal direction to suppress static and slow moving objects (e.g. wall reverberations). Data windows of  $4.4(z) \times 0.2(r)$  mm at 50% overlap were applied to the filtered RF data. The cross correlation based velocity estimation method, as validated in Chapter 3, was applied to assess the axial velocity distribution of the flow through the tube.

### 6.2.5 PWV assessment

#### Peak to peak transit time

In order to obtain a reference value for the PWV, the PWV was estimated by generating a steep pressure pulse and measuring the transit time over a long section of the polyurethane tube. Since the polyurethane tube that was applied has uniform mechanical properties and wall thickness nor tube radius varied, the local PWV corresponded with the global PWV. For the assessment of the transit time, the first pressure wire was positioned near the inlet of the tube ( $z_1 = 0$  m), the second 0.15 m downstream ( $z_2 = 0.15$  m) and the third pressure near the outlet of the tube ( $z_3 = 1.28$ ) m.

#### QA-method

In order to obtain PWV by means of the QA-method, the ultrasound system was operated in fast B-mode, employing 14 M-lines, generated at the minimum pitch  $\Delta z_p = 0.3125$  mm. The distance between the employed M-lines was minimized since for the cross correlation based velocity estimation, an increased pitch results in de-correlation, deteriorating the velocity estimation. The fast B-mode RF-data were processed as described in Section 6.2.4. This resulted in 2816 estimations of the vessel diameter,  $d(t)$ , and the instantaneous velocity profile,  $v(r, t)$  waveforms, sampled at 730 Hz. After application of a median filter, with a temporal and spatial window size of respectively,  $4 \cdot 10^{-3}$  s and  $6.9 \cdot 10^{-5}$  m, which was used to remove outliers from the velocity measurement, the velocity profiles were integrated to obtain flow,  $Q(t)$ . To suppress high frequency noise, a low pass Butterworth filter with a cutoff frequency of 20 Hz was applied, both to the diameter and flow waveforms. For application of the QA-method it was assumed that the cross sectional area of the vessel was circular. Consequently, the area waveform,  $A(t)$  was determined from the diameter waveform, by  $A(t) = \pi d(t)^2/4$ .

#### 2 and 3-point method

For estimation of PWV by means of the 2 and 3-point methods, the vessel radial wall position was used as an input. To compensate for global radial vessel motion, the difference between the anterior and posterior radial wall velocity was used as the input to estimate the local PWV. To cancel the influence of axial motion on the wall velocity estimate, the axial motion of the tube was locally constrained by placing the lower half of the tube in an agar gel. Due to this constraint, the compliance decreases locally, which results in an increased local PWV. A reference value for the local PWV was estimated by applying the 2 and 3-point methods to the pressure signals as assessed using the locally positioned pressure wires.

For the 2 and 3-point methods, the assessed signal, e.g. the wall velocity or pressure, was transformed into the frequency domain by means of an FFT. For each harmonic,  $\omega$ , the input signal,  $s$ , is given by

$$s(\omega, z, t) = \hat{s}(\omega)e^{i(\omega t - kz)}, \quad (6.13)$$

with  $k$  the complex wave number as defined in (6.10). Assuming that the signals were reflection free, the complex wave number can be calculated from a simultaneous assessment of  $s$  at two locations,  $s_1 = s(\omega, z_1, t)$  and  $s_2 = s(\omega, z_2, t)$ , by means of the two point method:

$$k_{2P}(\omega) = \frac{i}{\Delta z} \ln \left( \frac{\hat{s}_1(\omega)}{\hat{s}_2(\omega)} \right), \quad (6.14)$$

in which  $\Delta z$  is the distance between the measurement locations  $z_1$  and  $z_2$ . When reflections were present,  $s$  needs to be simultaneously assessed at three locations,  $s_1 = s(\omega, z_1, t)$ ,  $s_2 = s(\omega, z_2, t)$  and  $s_3 = s(\omega, z_3, t)$ , in order to estimate the complex wave number by means of the three point method (Taylor, 1959):

$$k_{3P}(\omega) = \frac{i}{\Delta z} \cosh^{-1} \left( \frac{\hat{s}_1(\omega) + \hat{s}_3(\omega)}{2\hat{s}_2(\omega)} \right) \quad (6.15)$$

where  $\Delta z$  is the distance between two adjacent measurement locations, e.g.  $z_1$  and  $z_2$  or  $z_2$  and  $z_3$ .

For the ultrasound-based assessment of the PWV by means of the 2 and 3-point methods, the ultrasound system was operated in fast B-mode, resulting in 14 M-lines (Figure 6.3). The distance between adjacent employed M-lines was set equal to the maximum value of  $\Delta z_p = 1.0938$  mm ( $3.5 \times \delta z_p$ ), which was favorable since this maximized the observed phase differences in wall motion, and so increases the accuracy of the 2 and 3-point methods.

Processing the fast B-mode RF-data, as described in Section 6.2.4, resulted in an estimate for the wall velocity at 14 locations (corresponding to the 14 M-lines) along the linear array, for a period of 3.8 s. Since Fourier analysis was required for application of the 2 and 3 point methods, only 3 s (3 complete periods) of the wall velocity signals were used.

For the application of the 2 and 3 point methods, the velocity as assessed at maximally, equidistantially spaced locations (solid lines in Figure 6.3) was used to estimate the PWV. For the 3-point method, this resulted in the wall velocity signals assessed at the combinations of transducers: 1, 7 and 13, and 2, 8 and 14

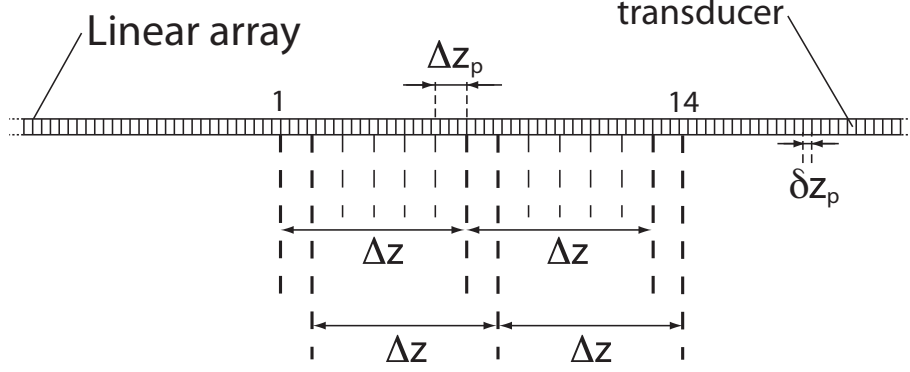


Figure 6.3: Schematic overview of the employed M-lines (dashed lines) generated by means of the linear array. At the locations corresponding to the M-lines, the wall velocity is estimated. For the application of the 2 and 3 point methods, the velocity as assessed at maximally, equidistantly spaced locations (solid dashed lines) is used to estimate the PWV.

(Figure 6.3). In order to compare the 2 and 3-point method, the wall velocity signals as assessed by corresponding transducers were applied for the 2-point method: 1 and 7, and 2 and 8 (Figure 6.3). The resulting distance between two adjacent measurement positions is  $\Delta z = 21\delta z_p = 6.6$  mm. Since the M-lines are obtained subsequently, the wall velocity signals  $s'_2$  and  $s'_3$  need to be corrected for the time delay with respect to  $s_1$  in order to obtain simultaneously assessed velocity waveforms:

$$\begin{aligned}\hat{s}_2 &= \hat{s}'_2 e^{6i\omega/f_{PRF}} \\ \hat{s}_3 &= \hat{s}'_3 e^{12i\omega/f_{PRF}}\end{aligned}\tag{6.16}$$

Subsequently (6.14) and (6.15) were applied to obtain the complex wave number. For each harmonic, the resulting complex wave number was averaged over both combinations of input signals and over 3 periods.

For the pressure wire-based assessment of the PWV by means of the 2 and 3-point method, 3 pressure wires, locally positioned at positions,  $z_1$ ,  $z_2$  and  $z_3$ , with an equidistant spacing of 0.1 m, respectively assess pressure signal  $p_1(t)$ ,  $p_2(t)$  and  $p_3(t)$ . Subsequently, (6.14) was applied to pressure signals,  $p_1(t)$  and  $p_2(t)$ , and (6.15) was applied to pressure signals  $p_1(t)$ ,  $p_2(t)$  and  $p_3(t)$ , to obtain an estimate of the complex wave number, respectively by the 2 and 3-point method. Resulting wave numbers were averaged over 3 periods.

### 6.2.6 Local pressure estimation

Local pressure was estimated from the simultaneous assessment of the PWV and the cross sectional area waveform by means of (6.2). However, the integral was replaced by a cumulative sum, since the diameter waveform, as assessed by means of ultrasound, was a discrete function:

$$p_n = p_0 + \frac{\rho c^2}{A} \sum_{i=1}^n \Delta A_n \quad \text{with} \quad \Delta A_n = A_{n+1} - A_n, \quad (6.17)$$

in which,  $p_n = p(n\Delta t)$  and  $A_n = A(n\Delta t)$ , with  $\Delta t = f^{-1}$  and  $n = 0, 1, 2, \dots, N - 1, N$ ,  $N = 2816$ .

Local pressure was only estimated for the QA-measurement. The agar gel locally obstructed deformation of the cross section of the vessel for the 2 and 3-point measurements, thereby preventing an the accurate estimation of vessel cross sectional area based on diameter measurement, thereby impeding the applicability of (6.17).

## 6.3 Results

### 6.3.1 PWV assessment

#### Peak to peak transit time

The pressure signals as assessed simultaneously by means of the pressure wires are presented in Figure 6.4 (top). For each signal, the time point corresponding to the global maximum is determined and subsequently plotted as a function of pressure wire position (Figure 6.4, bottom). The PWV is assessed by performing a least squares linear fit. The PWV, which is equal to the slope of the linear fit, is found to be:  $c = 9.4 \pm 0.1 \text{ ms}^{-1}$ .

#### QA-method

For three cycles, the cross-sectional area and flow were determined from the velocity and diameter estimation obtained from the RF-data. The resulting area and flow waveforms and the flow versus area loop are presented in Figure 6.5. The straight part of the loop corresponds to the reflection-free period of the cycle. By means of a least squares linear fit of the straight section, which was manually identified, the slope was found to be  $9.4 \pm 0.3 \text{ ms}^{-1}$ .

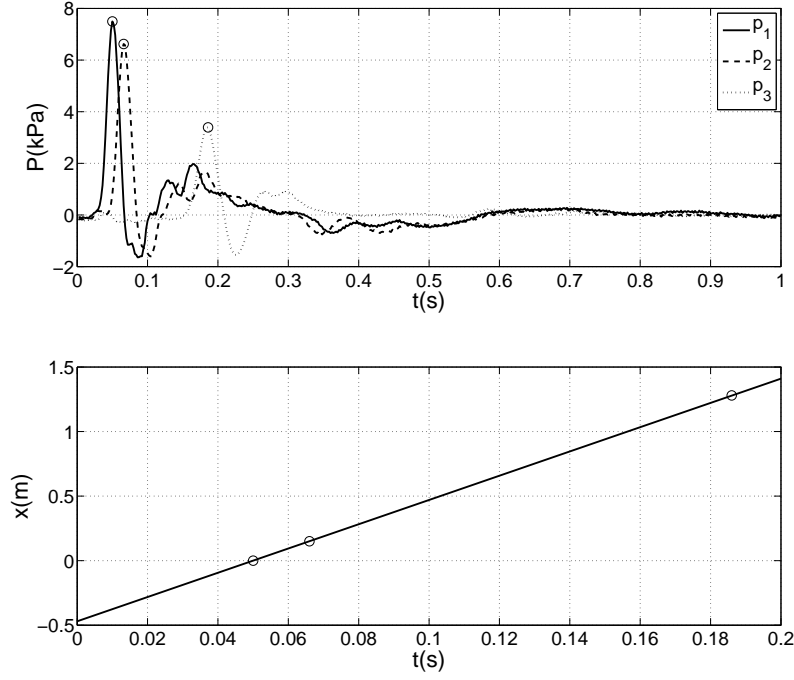


Figure 6.4: In the upper graph, the pressure signals ( $p_1 = p(z_1, t)$ ,  $p_2 = p(z_2, t)$  and  $p_3 = p(z_3, t)$ ) assessed by means of the pressure wires are presented. For each signal, the global maximum is indicated by  $\circ$ . In the lower graph, the time point corresponding to the global maximum in each pressure signal is plotted as a function of the measurement position,  $z_1$ ,  $z_2$  and  $z_3$ . The solid line indicates a least squares linear fit.

## 2 and 3-point methods

For the ultrasound-based PWV assessment, the real part of the complex wave number, as estimated by means of the 2 and 3 point method, is presented in Figure 6.6. For the 3 point method the deviation in the estimated real part of the complex wave number is found to be higher than for the 2 point method. From the wave propagation theory presented in Section 6.2.1 it was concluded that the PWV in the phantom vessel is approximately constant and equal to the Moens-Korteweg wave speed,  $c = c_0$ . As a result, a linear relation between frequency and real part of the complex wave exists, with a slope equal to  $2\pi/c$ . Subsequently,  $c$  is estimated by performing a linear fit to the data. For the 2 and 3-point method applied on the vessel wall velocity signal, respectively, a PWV equal to  $c = 8.7 \pm 0.8 \text{ ms}^{-1}$  and  $c = 8.6 \pm 2.4 \text{ ms}^{-1}$  is found.

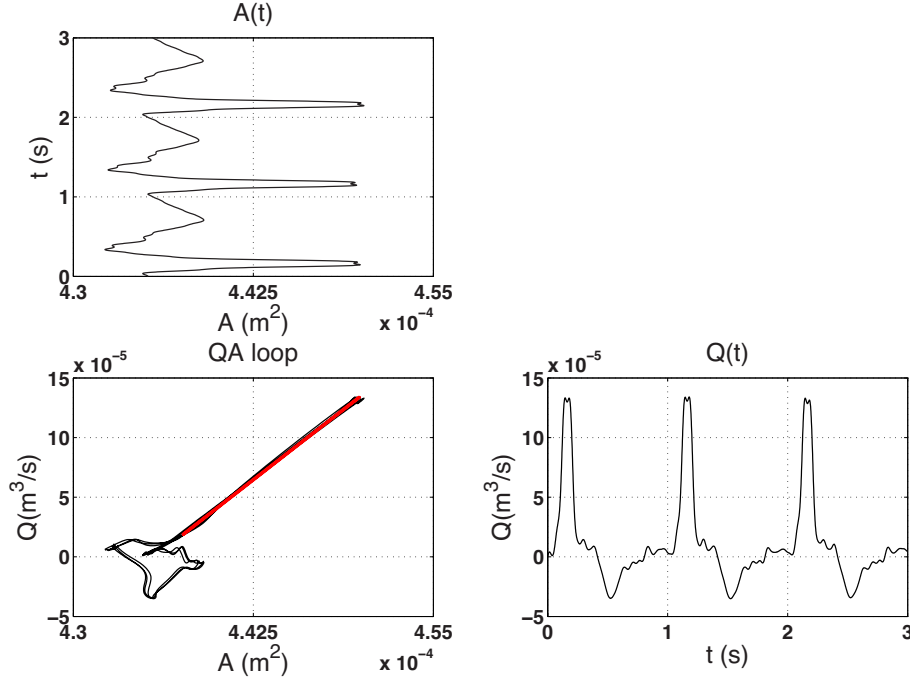


Figure 6.5: Estimated cross sectional area,  $A(t)$ , flow,  $Q(t)$ , and flow versus cross-sectional area loop for 3 cycles. The thick solid line indicated in the QA-loop represents a linear fit to the straight part of the loop.

As a reference, the 2 and 3-point methods were also applied to the pressure signals as acquired using the pressure wires. The real part of the estimated average complex wave number is presented in Figure 6.7. Deviations with respect to the presumed linear relation between the real part of the complex wave number and frequency are found to be more for the 2 point method than for the 3 point method, which is to be expected, since the performance of the 2-point measurement deteriorates in the presence of reflections. By performing a linear fit to the data,  $c$  was estimated to be equal to  $10.5 \pm 0.2 \text{ ms}^{-1}$  and  $10.3 \pm 0.6 \text{ ms}^{-1}$  for the 3 and 2-point method respectively. A slightly higher PWV with respect to the PWV as estimated by means of the QA-method is found.

### 6.3.2 Pressure assessment

For the QA-method, the PWV estimate and the vessel wall diameter waveform are combined to calculate the local pressure estimate by means of (6.17). The resulting pressure waveform is presented in Figure 6.8. As a reference, the pressure as assessed by the pressure wire has been added. The average pressure difference with respect to the pressure wire measurement is about 0.2 kPa, maximum and

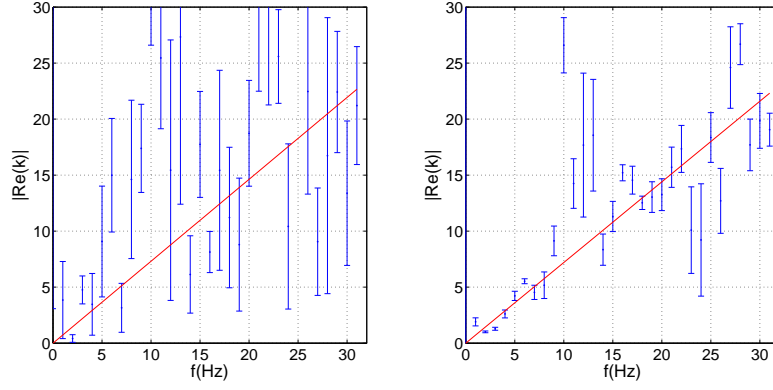


Figure 6.6: Real part of the complex wave number plotted as a function of the harmonic as assessed by applying the 3 point method (left) and 2 point method (right) to wall velocity signals as assessed using ultrasound. The solid lines indicate a linear fit to the data.

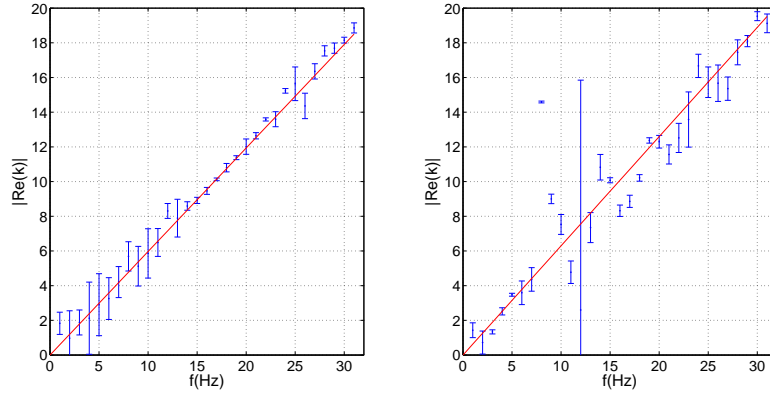


Figure 6.7: Real part of the complex wave number plotted as a function of the harmonic as assessed by applying the 3 point method (left) and 2 point method (right) to pressure signals assessed with pressure wires position at  $\Delta x = 0.10$  m with respect to each other. The solid lines indicate a linear fit to the data.

minimum values are estimated accurately.

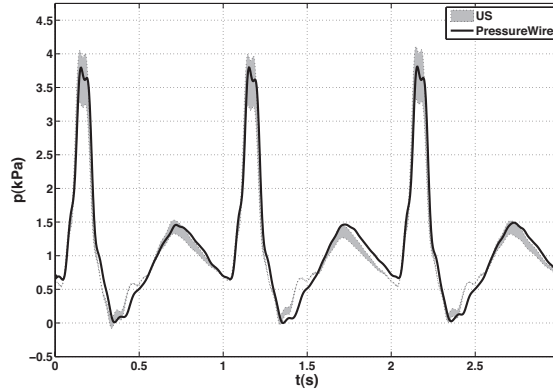


Figure 6.8: Local pressure, as estimated by means of a pressure wire measurement and as estimated from a simultaneous assessment of diameter waveform and PWV.

## 6.4 Discussion

Current non-invasive pressure estimation methods in general consist of the assessment of a waveform closely related to pressure, which is subsequently scaled by an additional pressure measurement to gain the pressure estimate. The PWV based method evaluated in this study however, allows pressure estimation from a single measurement; a simultaneous assessment of the local mechanical properties and motion of the vessel enables an accurate pressure assessment. However, current methods for local PWV estimation, e.g. by means of cross correlation based estimation methods (Struijk et al., 1992; Eriksson et al., 2002), are affected by reflections. Although the impact of reflections can be minimized by looking at characteristic points which are not too much influenced by reflections, e.g. the systolic foot in the distension waveform (McDonald, 1974; Hermeling et al., 2007), this requires an unambiguous approach for identifying these characteristic points. Besides, only a single point of the available distension waveform is employed, whereas an entire waveform is available.

In this study, two promising approaches for local PWV estimation, the QA-method and the 2 and 3 point methods, were evaluated. Both enable a straightforward method for measuring the local PWV.

As for current methods, the applicability of the QA-method is restricted to reflection free periods of the cardiac cycle, however it is more appropriate for practical application since this method allows a simple identification of the reflection free periods, by finding linear sections in the QA-loop. Furthermore, this method is most suitable for the ultrasound measurement technique applied in this study. Contrary to previous studies (Rabben et al., 2004; Williams et al., 2005), in the

present study, the vessel diameter and velocity profile were acquired simultaneously. No additional scaling or velocity profile approximations were applied to deduce flow. This resulted in an accurate simultaneous estimate of volume flow and cross sectional area. Subsequent application of the QA-method resulted in an estimate of the PWV, which accurately corresponded with the reference value as assessed using the peak to peak transit time measurement (Table 6.1). However, it should be noted that for the experimental setup, the reflection free period is relatively long, resulting in a significant linear section in the QA-loop. It is known however, that in most humans, only the early systolic wave is reflection free (Li, 2004), which lasts approximately 50 ms (Rabben et al., 2004). Although this is a short time period, the high sample rate (730 Hz) of the measurement technique applied in this study allows to estimate about 35 sample points in the early systolic wave. This should be sufficient to adequately estimate the slope of the linear section in the QA-loop. Still, it should be noted that the presence and the length of the reflection free period depends on the measurement location in the arterial system. In the periphery, the reflection free period might be significantly shorter.

Table 6.1: Results for the PWV estimation and measurement methods applied in this study.

Method	Setup	Data	$c$ (ms <sup>-1</sup> )
Transit time	Water	Pressure wire	$9.4 \pm 0.1$
QA	Water	Ultrasound	$9.4 \pm 0.3$
2-point	Agar	Ultrasound	$8.7 \pm 0.8$
		Pressure wire	$10.3 \pm 0.6$
3-point	Agar	Ultrasound	$8.6 \pm 2.4$
		Pressure wire	$10.5 \pm 0.2$

Contrary to the QA method, the 3-point method allows to estimate the PWV in the presence of reflections. As a result, no identification of a reflection free period is required, the complete period is applied for the estimation. The 3-point method was applied to ultrasound estimated wall velocity signals and pressure signals as assessed by means of pressure wires. As a reference, also the 2 point method was applied. The results from the 2 and 3-point methods applied to the wall velocity signal show that the 3-point method causes a much higher spread in the real part of the complex wave number compared to the 2-point method, which is not expected since the 3-point method should not be sensitive for reflections (Figure 6.6). Although the values of the PWV as estimated by means of the 2 and 3 point method correspond, they are found to be lower than expected based on the peak to peak transit time and QA-measurement (Table 6.1). Due to the local decrease of compliance as result of the local constriction of wall motion by the agar gel, a slightly higher value of the PWV is expected though. As a reference, the 2 and 3-point methods were also applied to pressure signals estimated by means of pressure wires. A comparison of the resulting real part of the complex wave number shows that, as expected, the 3-point method offers more precise estimates

of the propagation coefficient than the 2-point method (Figure 6.7). Additionally, as expected, a PWV value slightly higher than the value as estimated by the peak to peak transit time method is found (Table 6.1).

An important difference between the ultrasound-based and pressure wire-based assessment is the distance between measurement locations. For the ultrasound-based assessment, the distance equals only 0.66 cm, whereas the distance is equal to  $0.10 \cdot 10^{-2}$  m for the pressure wire-based assessment. The wavelength of the pressure wave traveling through the setup is equal to  $\lambda = c_0 T \approx 10$  m. For sensors positioned a few mm from each other, differences in signals assessed by the sensors are very small. The smaller the distance between measurement location, the more significant small amplitude and phase errors are. Decreasing the distance between pressure wires would allow a more truthful comparison with the ultrasound-based estimation. However, for the pressure wires, the positioning errors become significant for small inter-sensor distances, whereas for the ultrasound-based assessment, the measurement location is fixed by the physical distance between ultrasound transducers and therefore accurately known.

By manually generating input signals with known temporal shift in between, and subsequently mixing these signals with random noise of an increasing amplitude, it is found that the 3 point method is more sensitive to noise in the input signals than the 2 point method. This may cause the relatively poor precision observed in the real part of the complex wave number for the 3-point method.

In the ultrasound transducer, for generating a M-line, internally groups of transducers are employed to focus the ultrasound beam. The resulting beam width is approx 1 mm at the focus. Both the use of groups of transducers and the finite beam width result in the estimation of the average wall velocity for a finite section of the tube. Since the section is relatively large compared to the distance between the measurement locations, this might cause inaccuracies in the estimation of PWV based on the 2 and 3-point methods. This can contribute to the deviation in PWV found with respect to the reference measurement. The currently applied ultrasound system does not allow the activation of a set of transducers in the centre part of the linear array for application of the QA-method and simultaneously activate 2 transducers at the far ends of the linear array for 3-point based PWV estimation. However, such an option would be required for a true simultaneous assessment of PWV and flow.

For the high Womersley number ( $\alpha \approx 10$ ) occurring in the phantom setup, the waves travel at approximately the Moens-Korteweg wave velocity. In-vivo however, except for the aorta, the Womersley number is smaller and ranges from approximately 4 for the large arteries ( $r \approx 4$  mm) to about 1 for the small ( $r \approx 1$  mm) arteries. As a result, the wave speed may vary considerably with frequency, favoring the need for frequency dependent PWV estimation methods such as the 3-point method.

The combination of local PWV based on the QA-method and vessel diameter resulted in an accurate and precise estimate of the local pulse pressure. It should be noted that a constant pressure offset cannot be determined. The PWV estimated by means of the 2 and 3-point methods were not applied for local pressure estimation since the agar gel prevents the circular deformation of the vessel cross

section. This effect, but less severe, can also occur in-vivo due to non-uniform tissue properties surrounding the vessel. Additionally, for in-vivo application, errors in pressure estimate can be introduced due to non-linear material properties of the vessel wall.

## 6.5 Conclusion

Application of the QA-method and the 2 and 3-point methods for local PWV estimation by means of ultrasound were evaluated in a phantom setup. The QA method was found to allow an accurate and precise estimation of the PWV. A PWV value of  $9.4 \pm 0.3 \text{ ms}^{-1}$  was found, whereas the reference value, as estimated by means of a peak to peak transit time measurement, was found to be equal to  $9.4 \pm 0.1 \text{ ms}^{-1}$ . Although in theory, the 3 point method enables an unbiased precise estimation of PWV in the presence of reflections, in practice, applied to ultrasound estimated wall velocity signals, the PWV value obtained by this method,  $c = 8.6 \pm 2.4 \text{ ms}^{-1}$ , was found to be imprecise and to be an underestimation of the actual PWV. The similar 2-point method was also found to result in an underestimate for the PWV ( $c = 8.7 \pm 0.8 \text{ ms}^{-1}$ ). Based on the QA-method derived PWV and vessel diameter measurement, the local pulse pressure was estimated. The average pressure difference between estimated pressure and the reference pressure was found to be about 0.2 kPa. Maximum and minimum pressure values were also estimated accurately. The measurements performed in this study indicate that local pressure assessment by means of ultrasound is feasible.

## **Chapter 7**

# **General conclusion**

## 7.1 Introduction

The objective of this thesis was to develop and validate methods which enable a simultaneous and accurate assessment of volume flow and local pressure by means of non-invasive ultrasound. This enables the derivation of compliance and vascular impedance, which are both important parameters to characterize the cardiovascular disease (CVD) process. To enable an accurate validation of the developed methods, volume flow and pressure measurements were conducted in a phantom setup. Contrary to in-vivo tests, this allowed to perform well-defined experiments, facilitating comparison with analytical approximations and computational fluid dynamics (CFD) computations, and enabled comparison with reference measurements.

## 7.2 Study results

### 7.2.1 CFD as a validation tool

CFD models can be a valuable tool for the validation of novel measurement techniques. The first part of the thesis (Chapter 2) focussed on the application of CFD models for accurate assessment of local velocity components and pressure distribution in arteries. These models are required for the CFD-based validation of velocity, volume flow and pressure assessment methods in clinically relevant geometries. For arterial fluid structure interaction (FSI) problems, partitioned schemes are preferred. In partitioned schemes, weakly and strongly coupled methods exist. In currently applied weak coupling methods, convergence issues arise for vessels with a high length-to-radius ratio. In general, these issues can be overcome by strongly coupled methods, which apply sub-iterations and under-relaxation for solution of the fluid and the solid for each time step to converge to the solution of the fully coupled system (Fernandez et al., 2006; Fernandez and Moubachir, 2005; Deparis et al., 2006). The major drawback of these kinds of methods are poor robustness and the increasing amount of computational costs. In Chapter 2, currently applied weak coupling methods for fluid structure interaction (FSI) were compared and a dedicated coupling method, the time-periodic weakly coupled method, appropriate for pressure and flow waves in long compliant vessels, was introduced. The time-periodic method was found to allow modeling of vessels with a length up to 60 times the radius, without requiring a significant increase in computational effort. The currently applied timestep-wise coupling was found to only permit a length-to-radius ratio up to 10. In general, the length-to-radius ratio of geometries considered for arterial FSI computations is higher than 10, which indicates that the time-periodic method can be a valuable tool in the simulation of blood flow in arteries. Additionally, the introduced method enables an accurate validation of velocity and pressure measurement techniques in a phantom setup.

## 7.2.2 Non-invasive flow assessment

The second part of the thesis (Chapters 3, 4 and 5) focussed on improving volume flow estimation by means of non-invasive ultrasound, based on the accurate assessment and correct integration of the complete axial velocity profile, for both straight and curved geometries. CFD models were applied as a tool to validate the velocity assessment method and the novel integration method.

In clinical practice, volume flow is often estimated based on axial velocity as assessed using Doppler ultrasound. However, an accurate assessment of the complete axial velocity profile by means of Doppler ultrasound is not possible (Leguy et al., 2009). Near the vessel wall, velocity estimates are less accurate. Since the assessment of the centreline or maximum velocity is less subject to measurement errors, the volume flow is estimated by assuming a specific velocity distribution, e.g. a Poiseuille or Womersley profile (Douchette et al., 1992), based on the assessment of the centreline or maximum velocity and the local diameter. However, most arteries are tapered, curved and bifurcating, causing the axial velocity distribution to be altered by secondary velocities, resulting in asymmetrical axial velocity profiles and consequently in inaccurate flow estimations (Krams et al., 2005). For the diameter assessment, a separate measurement needs to be performed since the non-perpendicular insonification angle, required for performing a Doppler measurement, prevents an accurate diameter assessment. Consequently, accurate volume flow estimation based on a single ultrasound measurement is not possible without applying complex probes.

In Chapter 3, an ultrasound velocity estimation method was validated which enables an accurate simultaneous assessment of the complete axial velocity profile and vessel wall position. Particle image velocimetry (PIV) based methods were applied to estimate axial velocity from raw RF-data obtained by means of a linear array transducer positioned perpendicularly with respect to the vessel axis. For the experimental validation, physiologically relevant flows were considered in a straight vessel phantom, employing a blood analog fluid which mimics both the acoustic and mechanical properties of blood. Accurate velocity profile measurements were obtained (deviation about  $3 \text{ cm s}^{-1}$  with respect to CFD for mean velocities varying from 10 to  $40 \text{ cm s}^{-1}$ ), without requiring high concentrations of particles to induce a large amount of scattering such as in ultrasound speckle velocimetry (UPV) (Bohs et al., 1993, 1995; Sandrin et al., 2001; Trahey et al., 1987), custom developed ultrasound systems as in current Echo PIV methods (Liu et al., 2008) or averaging over multiple measurements (Kim et al., 2004a; Liu et al., 2008). Integration of the assessed axial velocity profile to volume flow yielded flow estimates which accurately agreed with reference volume flow assessments.

In Chapter 4, an analytical/CFD based study was presented, which concentrates on the derivation and validation of a flow estimation method which improves the estimation of volume flow through a curved tube based on the (asymmetric) axial velocity profile. The  $\cos \theta$ -method, a novel flow estimation method, was derived from an analysis of existing analytical approximation methods for flow in curved

tubes. The  $\cos\theta$ -method was validated and compared to the currently applied Poiseuille method by means of CFD modelling. Although the Poiseuille method was found to suffice for  $Dn \leq 100$ , the  $\cos\theta$ -method was found to estimate the volume flow nearly three times better than the Poiseuille method for the higher, clinically relevant, Dean numbers. For  $\delta = 0.01$  the maximum deviation from the exact flow is 4% for the  $\cos\theta$ -method, while this is 12.7% for the Poiseuille method in the plane of symmetry. For  $Dn = 1000$  and  $\delta = 0.16$ , the error in flow estimation by means of the  $\cos\theta$ -method was found to be at most 6.2%. The results indicate that the  $\cos\theta$  allows an accurate estimation of volume flow through a curved tube from a given asymmetrical axial velocity profile, whereas the Poiseuille method, which is currently often used in clinical practice, offers a poor flow estimation (Leguy et al., 2009).

In Chapter 5, the PIV-based ultrasound velocity assessment technique, validated in Chapter 3, was applied to both stationary and non-stationary non-Newtonian flow in a planar curved geometry in a phantom setup. For the experiments, again, physiologically relevant flows were considered, employing a blood analog fluid which mimics both the acoustic and mechanical properties of blood. Excellent agreement was found between the axial velocity profile measurement and CFD calculations of the axial velocity profile, which shows that the applied velocity estimation technique is able to cope with the relatively high spatial and temporal velocity gradients occurring in curved tube flow. Subsequently, the  $\cos\theta$ -method was applied to estimate the flow from the asymmetric axial velocity profiles and compared to the currently applied Poiseuille and Womersley approximations. The comparison shows, as expected from the CFD-based analysis presented in Chapter 4, that the  $\cos\theta$ -integration based flow estimate is much more accurate than the Poiseuille and Womersley based estimations. For the non-stationary flow measurements, a deviation of 5% with respect to the reference flow was found for the  $\cos\theta$  method, compared to an average deviation of 20% for both the Poiseuille and Womersley approximation. Additionally, by means of a CFD based analysis, it was found that an accurate flow estimation is feasible, even when not measured exactly through the centre of the tube. This facilitates the flow estimation for in-vivo measurements, since for this case, the exact orientation of the ultrasound beam with respect to the curved vessel, and thus the orientation of the measured velocity profile with respect to the cross section, is generally unknown.

### 7.2.3 Non-invasive pressure assessment

Finally, Chapter 6 focusses on the non-invasive estimation of local pressure. In current clinical practice, local pressure is often assessed by estimating a waveform closely related to pressure that is subsequently scaled by an additional direct pressure measurement to gain a pressure estimate. A direct pressure measurement that can be applied simultaneously with a flow assessment is preferred. In Chapter 6, local pressure was estimated by combining knowledge of the mechanical behaviour of the arterial wall with the assessment of wall motion. Local compli-

ance was estimated by measuring the pulse wave velocity (PWV), subsequently compliance was combined with vessel cross sectional area to estimate pressure.

Measurements of the PWV were performed by means of the QA-method, the 2-point, and the 3-point method. It was found that the QA-method allows a precise and unbiased estimation of the PWV. Although the application of this method is restricted to the reflection free period of the cardiac cycle, it offers a straightforward method for recognizing the reflection free period in a QA-loop. Existing methods (Struijk et al., 1992; Hermeling et al., 2007) require wave separation analysis (Khir et al., 2001) to check whether reflections were present during the measurement. In theory, the 3-point method allows to accurately estimate local PWV in the presence of reflections (Bertram et al., 1997). This has been confirmed in this thesis by measurements using pressure wires. Applied to pressure signals obtained using pressure wires, precise estimates of the PWV were found. However, for ultrasound, the 3-point method (and also the 2-point method) was found to offer a poor estimate of the PWV when applied to vessel wall velocity. This indicates that application of the 2 and 3-point method to vessel wall motion, as assessed by means of the currently used ultrasound probe, is not suitable for local PWV estimation. Based on the QA-method derived PWV and vessel diameter measurement, the local pulse pressure was estimated. The average pressure difference between estimated pressure and the reference pressure was found to be about 0.2 kPa, which is about 5% of the pulse pressure value. Maximum and minimum pressure values were also accurately estimated. This shows that the simultaneous assessment of PWV and wall diameter is a promising method to estimate local pressure.

Studies of arterial impedance in humans are hampered by the lack of reliable non-invasive techniques to simultaneously assess the local pressure waveform and volume flow. The experiments presented in this study show that a precise, unbiased and combined assessment of local pressure and volume flow by means of non-invasive ultrasound assessment is feasible. Since no velocity profile approximations or substitutes for pressure, as in e.g. Brands et al. (1996), are applied, this allows to derive the genuine arterial impedance, instead of a non-dimensionalized form. The methods introduced have the potential to enable an accurate in-vivo derivation of arterial impedance.

### 7.3 Clinical perspective

Although each experiment and CFD computation presented in this study was designed to mimic a relevant in-vivo situation, they still only offer a simplified version of the complex in-vivo situation. Consequently, for in-vivo application of the flow and pressure estimation methods developed, some additional research as described below is required.

Considering the velocity and flow estimation, the most important difference be-

tween the experiments performed in this study and clinical application is the influence of ultrasound reverberations. In the experiments, the vessel wall is modelled as a thin-walled polyurethane tube surrounded by water, whereas in-vivo, the vessel wall is a multilayered complex material, surrounded by tissue. The non-stationary flow measurements in the straight vessel phantom have shown that reverberations can cause significant errors in the velocity estimation. In the phantom setup the reverberation occurs at a discrete position because of the uniform vessel wall thickness and properties. As a result, the velocity assessment is disrupted only locally. However, in-vivo, reverberations are present throughout the lumen, further complicating the velocity estimation. In-vivo, proper clutter removal filters are required to allow an accurate velocity and volume flow assessment. Assuming that adequate filters can be developed and given the increase in sensitivity of novel ultrasound systems, the methods presented in Chapter 3, 4 and 5 will enable an improved in-vivo volume flow assessment for both straight and curved geometries.

In the phantom setup, it is shown that a precise and unbiased non-invasive pressure estimation, based on the simultaneous assessment of PWV and vessel diameter is feasible. Requirements such as an adequately long reflection free period in the cardiac cycle and a circular vessel cross section are accurately met in the phantom setup. In-vivo, however, the length and existence of the reflection free period depends on the location in the arterial system, complicating the applicability of the QA-method for PWV estimation. In the future, application of the 3-point method on wall velocity signals obtained with a linear array probe which allows to obtain M-lines at maximally spaced locations along the transducer array, might allow the accurate and precise assessment of PWV in the presence of reflections, thereby relaxing the need for a reflection free period. Additionally, due to inhomogeneity of the surrounding tissue, the cross sectional area of the vessel might not remain circular during deformation, complicating the cross sectional area estimation based on the diameter assessment.

The methods developed and validated for volume flow and pressure assessment were applied to RF data acquired by means of a commercially available, clinically approved ultrasound system. The methods were merely applied as post processing steps, no adjustments to the hardware of the ultrasound system were employed. As a result, a swift transition from the experimental application to clinical application is possible.

In-vivo application of the measurement methods presented in this study can improve the non-invasive assessment of pressure and volume flow, and subsequently, compliance and vascular impedance. This allows a better assessment of the condition of the vascular system, enabling the acquisition of information of the effect of therapeutic interventions and the identification of factors which are characteristic for the development of CVD.

## 7.4 Conclusion

Non-invasive ultrasound based measurement methods, enabling the simultaneous assessment of volume flow and pressure, were developed. Validation experiments in a phantom setup have shown excellent accuracy and precision for both volume flow and pressure assessments. Compared to current methods, volume flow assessment has been significantly improved, especially in curved geometries. For the pressure assessment only a local ultrasound measurement is required. Although some additional research is required for in-vivo application of the methods developed, the prospects for clinical application look promising. The ability to simultaneously assess pressure and volume flow can significantly improve derivation of parameters such as arterial impedance and compliance.



## Bibliography

- R. J. Adrian. Particle-imaging techniques for experimental fluid mechanics. *Annual Reviews of Fluid Mechanics*, 23:261–304, 1991.
- R. J. Adrian. Twenty years of particle image velocimetry. *Experiments in Fluids*, 39:159–169, 2005.
- Y. Agrawal, L. Talbot, and K. Gong. Laser anemometer study of flow development in curved circular pipes. *Journal of Fluid Mechanics*, 85:497–518, 1978.
- S. Balbis, S. Roatta, and C. Guiot. Curvature affects Doppler investigations of vessels: Implications for clinical practice. *Ultrasound in Medicine & Biology*, 31(1):65–77, 2005.
- S. A. Berger and L. Talbot. Flow in curved pipes. *Annual Reviews of Fluid Mechanics*, 15:461–512, 1983.
- C. D. Bertram, B. S. Gow, and S. E. Greenwald. Comparison of different methods for the determination of the true wave propagation coefficient, in rubber tubes and the canine thoracic aorta. *Medical Engineering & Physics*, 19(3):212–222, 1997.
- D. Bessems, M. C. M. Rutten, and F. N. van de Vosse. A wave propagation model of blood flow in large vessels using an approximate velocity profile function. *Journal of Fluid Mechanics*, 580:145–168, 2007.
- D. Bessems, C. G. Giannopapa, M. C. M. Rutten, and F. N. van de Vosse. Experimental validation of a time-domain based wave propagation model of blood flow in viscoelastic vessels. *Journal of Biomechanics*, 41(2):284–291, 2008.
- B. W. A. M. M. Beulen, M. C. M. Rutten, and F. N. van de Vosse. Fluid structure interaction in distensible vessels: a time periodic coupling. *Journal of Fluids and Structures*, DOI:10.1016/j.jfluidstructs.2009.03.002, 2009.
- R. B. Bird. *Dynamics of Polymeric Liquids*, volume 2. John Wiley and Sons, 1987.

- L. N. Bohs, B. H. Friemel, B. A. McDermott, and G. E. Trahey. A real time system for quantifying and displaying two-dimensional velocities using ultrasound. *Ultrasound in Medicine & Biology*, 19(9):751–761, 1993.
- L. N. Bohs, B. H. Friemel, and G. E. Trahey. Experimental velocity profiles and volumetric flow via two-dimensional speckle tracking. *Ultrasound in Medicine & Biology*, 21(7):885–898, 1995.
- L. N. Bohs, B. J. Geiman, M. E. Anderson, S. C. Gebbart, and G. E. Trahey. Speckle tracking for multi-dimensional flow estimation. *Ultrasonics*, 38:369–375, 2000.
- P. Boutouyrie, S. Laurent, X. Girerd, A. Benetos, P. Lacolley, E. Abergel, and M. E. Safar. Common carotid stiffness and patterns of left ventricular hypertrophy in hypertensive patients. *Hypertension*, 25:651–659, 1995.
- P. H. M. Bovendeerd, A. A. van Steenhoven, F. N. van de Vosse, and G. Vossers. Steady entry flow in a curved pipe. *Journal of Fluid Mechanics*, 177:233–246, 1987.
- P. J. Brands, A. P. G. Hoeks, M. C. M. Rutten, and R. S. Reneman. A noninvasive method to estimate arterial impedance by means of assessment of local diameter change and the local center-line blood flow velocity using ultrasound. *Ultrasound in Medicine & Biology*, 22(7):895–905, 1996.
- P. J. Brands, A. P. G. Hoeks, L. A. F. Ledoux, and R. S. Reneman. A radio frequency domain complex cross-correlation model to estimate blood flow velocity and tissue motion by means of ultrasound. *Ultrasound in Medicine & Biology*, 23(6):911–920, 1997.
- P. J. Brands, J. M. Willigers, L. A. F. Ledoux, R. S. Reneman, and A. P. G. Hoeks. A noninvasive method to estimate pulse wave velocity in arteries locally by means of ultrasound. *Ultrasound in Medicine & Biology*, 24(9):1325–1335, 1998.
- P. J. Brands, A. P. G. Hoeks, J. M. Willigers, C. Willekes, and R. S. Reneman. An integrated system for the non-invasive assessment of vessel wall and hemodynamic properties of large arteries by means of ultrasound. *European Journal of Ultrasound*, 9:257–266, 1999.
- K. A. Brookshier and J. M. Tarbell. Evaluation of transparent blood analog fluid: Aqueous xanthan gum/glycerin. *Biorheology*, 30:107–116, 1993.
- C. Caro, G. Fitzgerald, and R. Schroter. Atheroma and arterial wall shear: Observation, correlation and proposal of shear dependent mass transfer mechanism for atherogenesis. *Proceedings of the Royal Society London B: Biological Science*, 117:109–159, 1971.
- P. Causin, J. F. Gerbeau, and F. Nobile. Added-mass effect in the design of partitioned algorithms for fluid-structure problems. *Computer Methods in Applied Mechanics and Engineering*, 194:4506–4527, 2005.

- J. L. Cezeaux and A. Grondelle. Accuracy of the inverse Womersley method for the calculation of hemodynamic variables. *Annals of Biomedical Engineering*, 25:536–546, 1997.
- C. H. Chen, E. Nevo, B. Fetics, P. H. Pak, F. C. P. Yin, W. L. Maughan and D. A. Kass. Estimation of central aortic pressure waveform by mathematical transformation of radial tonometry pressure. *Circulation*, 95:1827–1836, 1997.
- S. Chien, S. Usami, R. J. Dellenback, and M. I. Gregersen. Shear dependent deformation of erythrocytes in rheology of human blood. *American Journal of Physiology*, 219(1):136–142, 1970.
- G. Cloutier, M. Daronat, D. Savéry, D. Garcia, L. G. Durand, and S F. Foster. Non-Gaussian statistics and temporal variations of the ultrasound signal backscattered by blood at frequencies between 10 and 58 MHz. *The Journal of the Acoustical Society of America*, 116(1):566–577, 2004.
- W. M. Collins and S. C. R. Dennis. The steady motion of a viscous fluid in a curved tube. *The quarterly journal of mechanics and applied mathematics*, XXVIII(2):133–156, 1975.
- M. Crapper, T. Bruce, and C. Gouble. Flow field visualization of sediment-laden flow using ultrasonic imaging. *Dynamics of Atmospheres and Oceans*, 31:233–245, 2000.
- C. Cuvelier, A. Segal, and A. A. van Steenhoven. *Finite element methods and Navier-Stokes equations*. D. Reidel Publishing Comp., Dordrecht, 1986.
- J. de Hart, G. W. M. Peters, P. J. G. Schreurs, and F. P. T. Baaijens. A three-dimensional computational analysis of fluid-structure interaction in the aortic valve. *Journal of Biomechanics*, 36(1):103–112, 2003.
- W. R. Dean. Note on the motion of fluid in a curved pipe. *Philosophical Magazine and Journal of Science*, 4(20):209–223, 1927.
- W. R. Dean. The streamline motion of fluid in a curved pipe. *Philosophical Magazine and Journal of Science*, 5(30):673–695, 1928.
- S. Deparis, M. Discacciati, G. Fourestey, and A. Quarteroni. Fluid-structure algorithms based on Steklov-Poincaré operators. *Computer Methods in Applied Mechanics and Engineering*, 195:5797–5812, 2006.
- J. Donea, S. Giuliani, and J. P. Halleux. An arbitrary Lagrangian-Eulerian finite element method for transient dynamic fluid-structure interactions. *Computer Methods in Applied Mechanics and Engineering*, 33:689–723, 1982.
- J. W. Douchette, P. D. Corl, H. M. Payne, E. Flynn, M. Goto, M. Nassi, and J. Segal. Validation of a Doppler guide wire for intravascular measurement of coronary artery flow velocity. *Circulation*, 85:1899–1911, 1992.

- A. Eriksson, E. Greiff, T. Loupas, M. Persson, and P. Pesque. Arterial pulse wave velocity with tissue Doppler imaging. *Ultrasound in Medicine & Biology*, 28: 571–580, 2002.
- D. H. Evans, W. N. McDicken, R. Skidmore, and J. P. Woodcock. *Doppler ultrasound: Physics, instrumentation, and clinical applications*. John Wiley and Sons, 1989.
- M. Evans, N. Hastings, and B. Peacock. *Statistical Distributions*. Wiley New York, 2000.
- M. A. Fernandez and M. Moubachir. A Newton method using exact Jacobians for solving fluid-structure coupling. *Computers & Structures*, 83:127–142, 2005.
- M. A. Fernandez, V. Millisic, and A. Quarteroni. Analysis of a geometrical multiscale blood flow model based on the coupling of odes and hyperbolic pdes. *Multiscale Modeling and Simulation*, 4:215–236, 2005.
- M. A. Fernandez, J. F. Gerbeau, and C. Grandmont. A projection algorithm for fluid-structure interaction problems with strong added-mass effect. *Comptes Rendus Mathematique*, 342(4):279–284, 2006.
- M. F. Fillinger and R. A. Schwartz. Volumetric blood flow measurements with color Doppler ultrasonography: the importance of visual clues. *Journal of Ultrasound in Medicine*, 3:123–130, 1993.
- L. Formaggia, F. Nobile, A. Quarteroni, and A. Veneziani. Multiscale modelling of the circulatory system: a preliminary analysis. *Computing and Visualization in Science*, 2:75–83, 1999.
- L. Formaggia, J. F. Gerbeau, F. Nobile, and A. Quarteroni. On the coupling of 3D and 1D Navier-Stokes equations for flow problems in compliant vessels. *Computer Methods in Applied Mechanics and Engineering*, 191:561–582, 2001.
- C. Forster, W. A. Wall, and E. Ramm. Artificial added mass instabilities in sequential staggered coupling of nonlinear structures and incompressible viscous flows. *Computer Methods in Applied Mechanics and Engineering*, 196:1278–1293, 2007.
- M. D. Fox. Multiple crossed-beam ultrasound Doppler velocimetry. *IEEE Trans Son Ultrason*, SU-25:281–286, 1978.
- O. Frank. Die Elastizität der Blutgefäße. *Z. Biol*, 71:255–272, 1922.
- K. H. Fraser, S. Meagher, Blake J R., W. J. Easson, and P. R. Hoskins. Characterization of an abdominal aortic velocity waveform in patients with abdominal aortic aneurysm. *Ultrasound in Medicine & Biology*, 34(1):73, 80 2008.
- M. H. Friedman, C. B. Barger, D. D. Duncan, G. M. Hutchins, and F. F. Mark. Effects of arterial compliance and non-Newtonian rheology on correlations between intimal thickness and wall shear. *Journal of Biomechanical Engineering*, 114:317–320, 1992.

- Y. C. Fung. *Biomechanics: mechanical properties of living tissues*. Berlin, Germany: Springer, 1993.
- C. G. Giannopapa. *Fluid Structure Interaction in Flexible Vessels*. PhD thesis, King's College London, 2004.
- F. J. H. Gijssen, F. N. van de Vosse, and J. D. Janssen. Influence of the non-Newtonian properties of blood on the flow in large arteries: Steady flow in a carotid bifurcation model. *Journal of Biomechanics*, 32(6):601–608, 1999a.
- F. J. H. Gijssen, F. N. van de Vosse, and J. D. Janssen. Influence of the non-Newtonian properties of blood on the flow in large arteries: Unsteady flow in a 90 degree curved tube. *Journal of Biomechanics*, 32(7):705–713, 1999b.
- R. W. Gill. Measurement of blood flow by ultrasound: accuracy and sources of error. *Ultrasound in Medicine & Biology*, 11:625–641, 1985.
- D. P. Hart. Super-resolution PIV by recursive local-correlation. *Journal of Visualization*, 3(2):187–194, 2000.
- K. Hayashi, S. Handa, H. Nagasawa, A. Okumura, and K. Moritake. Stiffness and elastic behavior of human intracranial and extracranial arteries. *Journal of Biomechanics*, 13:175–184, 1980.
- E. Hermeling, K D. Reesink, R. S. Reneman, and A. P. G. Hoeks. Measurement of local pulse wave velocity: effects of signal processing on precision. *Ultrasound in Medicine & Biology*, 33(5):774–481, 2007.
- A. P. G. Hoeks, P. J. Brands, F. A. Smeets, and R. S. Reneman. Assessment of the distensibility of superficial arteries. *Ultrasound in Medicine & Biology*, 16:121–128, 1990.
- A. P. G. Hoeks, J. J. W. van der Vorst, A. Dabekaussen, P. J. Brands, and R. S. Reneman. An efficient algorithm to remove low frequency Doppler signals in digital Doppler systems. *Ultrasound Imaging*, 13:135–144, 1991.
- A. P. G. Hoeks, C. Willekes, P. Boutouyrie, P. J. Brands, J. M. Willigers, and R. S. Reneman. Automated detection of local artery wall thickness based on M-line signal processing. *Ultrasound in Medicine & Biology*, 23:1017–1023, 1997.
- A. P. G. Hoeks, J. M. Willigers, and R. S. Reneman. Effects of assessment and processing techniques on the shape of arterial pressure-distension loops. *Journal of Vascular Research*, 37:494–500, 2000.
- A. P. G. Hoeks, J. M. Meinders, and R. Dammers. Applicability and benefit of arterial transfer functions. *Journal of Hypertension*, 21:1241–1243, 2003.
- T. J. R. Hughes and J. Lubliner. On the one-dimensional theory of blood flow in large vessels. *Mathematical Biosciences*, 18:161–170, 1973.

- J. A. Jensen and P. Munk. A new method for estimation of velocity vectors. *IEEE Transactions on ultrasonics, ferroelectric and frequency control*, 45(3):837–851, 1998.
- R. D. Keane and R. J. Adrian. Optimization of particle image velocimeters: 1. double pulsed systems. *Measurement Science and Technology*, 1:1202–1215, 1992.
- A. W. Khir, A. O’Brien, J. S. R. Gibbs, and K. H. Parker. Determination of wave speed and wave separation in arteries. *Journal of Biomechanics*, 34:1145–1155, 2001.
- H. B. Kim, J. Hertzberg, C. Lanning, and R. Shandas. Noninvasive measurement of steady and pulsating velocity profiles and shear rates in arteries using echo piv: In vitro validation studies. *Annals of Biomedical Engineering*, 32(8):1067–1076, 2004a.
- H. B. Kim, J. R. Hertzberg, and R. Shandas. Development and validation of echo piv. *Experiments in Fluids*, 36:455–462, 2004b.
- R. Krams, G. Bambi, F. Guidi, F. Helderman, A. F. W. van der Steen, and P. Tortoli. Effect of vessel curvature on Doppler derived velocity profiles and fluid flow. *Ultrasound in Medicine & Biology*, 31(5):663–671, 2005.
- F. W. Kremkau. *Diagnostic ultrasound: principles and instruments*. W.B. Saunders Company, 1998.
- D. Ku, D. P. Giddens, C. K. Zarins, and S. Glagov. Pulsatile flow and atherosclerosis in the human carotid bifurcation. *Arteriosclerosis*, 5:293–302, 1985.
- D. N. Ku. *Hemodynamics and atherogenesis at the human carotid bifurcation*. PhD thesis, Georgia Institute of Technology, 1983.
- S. Laurent, L. Cockcroft, L. Van Bortel, P. Boutouyrie, C. Giannattasio, D. Hayoz, B. Pannier, C. Vlachopoulos, I. Wilkinson, and H. Struijker-Boudier. Expert consensus document on arterial stiffness: methodological issues and clinical applications. *European Heart Journal*, 27:2588–2605, 2006.
- C. A. D. Leguy, E. M. H. Bosboom, A. P. G. Hoeks, and F. N. van de Vosse. Assessment of blood volume flow in slightly curved arteries from a single velocity profile. *Journal of Biomechanics*, DOI: 10.1016/j.jbiomech.2009.04.032, 2009.
- C. A. D. Leguy, E. M. H. Bosboom, A. P. G. Hoeks, and F. N. van de Vosse. Model-based assessment of dynamic arterial blood volume flow from ultrasound measurements. *Medical & Biological Engineering & Computing*, 47:641–648, 2009.
- E. D. Lehmann, J. R. Parker, K. D. Hopkins, M. G. Taylor, and R. G. Gosling. Validation and reproducibility of pressure-corrected aortic distensibility measurements using pulse-wave-velocity measurements. *Journal of Biomechanical Engineering*, 15:221–228, 1993.

- J. K. Li. *Dynamics of the vascular system*. New Jersey: World Scientific, 2004.
- L. Liu, H. Zheng, L. Williams, F. Zhang, R. Wang, J. Hertzberg, and R. Shandas. Development of a custom-designed echo particle image velocimetry system for multi-component hemodynamic measurements: system characterization and initial experimental results. *Physics in Medicine and Biology*, 53:1397–1412, 2008.
- H. G. Matthies and J. Steindorf. Partitioned but strongly coupled iteration schemes for nonlinear fluid-structure interaction. *Computers & Structures*, 80: 27–30, 2002.
- D. J. McConalogue and R. S. Srivastava. Motion of a fluid in a curved tube. *Proceedings of the Royal Society of London. Series A*, 307(37-53), 1968.
- D. A. McDonald. *Blood Flow in Arteries*. Edward Arnold, London, 1974.
- J. M. Meinders and A. P. G. Hoeks. Simultaneous assessment of diameter and pressure waveforms in the carotid artery. *Ultrasound in Medicine & Biology*, 39(2):147–154, 2004.
- J. M. Meinders, L. Kornet, P. J. Brands, and A. P. G. Hoeks. Assessment of local pulse wave velocity in arteries using 2D distension waveforms. *Ultrasonic Imaging*, 23:199–215, 2000.
- J. M. Meinders, P. J. Brands, J. M. Willigers, L. Kornet, and A. P. G. Hoeks. Assessment of the spatial homogeneity of artery dimension parameters with high frame rate 2-D B-mode. *Ultrasound in Medicine & Biology*, 27(6):785–794, 2001.
- S. C. Milasseau, F. G. Guigui, R. P. Kelly, K. Prasad, J. R. Cockcroft, J. M. Ritter, and P. J. Chowienzyk. Noninvasive assessment of the digital volume pulse. comparison with the peripheral pressure pulse. *Hypertension*, 36(952-956), 2000.
- W. R. Milnor. *Hemodynamics*. Williams & Wilkins, 1989.
- G. F. Mitchell, H. Parise, J. A. Vita, M. G. Larson, E. Warner, J. F. Keaney, M. J. Keyes, D. Levy, R. S. Vasan, and E. J. Benjamin. Local shear stress and brachial artery flow-mediated dilation: the framingham heart study. *Hypertension*, 44 (134), 2004.
- S. Murata, Y. Miyake, and T. Inaba. Laminar flow in a curved pipe with varying curvature. *Journal of Fluid Mechanics*, 73:735–752, 1976.
- M. S. Olufsen, C. S. Peskin, W. Y. Kim, E. M. Pedersen, A. Nadim, and J. Larsen. Numerical simulation and experimental validation of blood flow in arteries with structured-tree outflow conditions. *Annals of Biomedical Engineering*, 28:1281–1299, 2000.
- M. F. O’Rourke. Mechanical principles. arterial stiffness and wave reflection. *Pathol Biol (Paris)*, 47:623–633, 1999.

- J. R. Overbeck, K. W. Beach, and D. E. Strandness. Vector Doppler: accurate measurement of blood velocity in two dimensions. *Ultrasound in Medicine & Biology*, 18:19–31, 1992.
- D. Paeng, R. Y. Chiao, and K. K. Shung. Echogenicity variations from porcine blood i: the "bright collapsing ring" under pulsatile flow. *Ultrasound in Medicine & Biology*, 30(1):45–55, 2004a.
- D. Paeng, R. Y. Chiao, and K. K. Shung. Echogenicity variations from porcine blood ii: the "bright collapsing ring" under oscillatory flow. *Ultrasound in Medicine & Biology*, 30(6):815–825, 2004b.
- K. H. Parker and C. J. H. Jones. Forward and backward running waves in the arteries: analysis using the method of characteristics. *Journal of Biomechanical Engineering*, 112:322–326, 1990.
- T. J. Pedley. *The Fluid Mechanics of Large Blood Vessels*. Cambridge University Press, 1980.
- S. Petersen, V. Petra, M. Rayner, J. Leal, R. Luengo-Fernandez, and A. Cray. European cardiovascular disease statistics. Technical report, University of Oxford, 2005.
- T. Powalowski and B. Pensko. A noninvasive ultrasonic method for the elasticity evaluation of the carotid arteries and its application in the diagnosis of the cerebro-vascular system. *Archives of Acoustics*, 13:109–126, 1988.
- A. Quarteroni and A. Veneziani. Analysis of a geometrical multiscale model based on the coupling of ODE's and PDE's for blood flow simulations. *Multiscale Modeling and Simulation*, 1:173–195, 2003.
- S. I. Rabben, S. Bjaerum, V. Sorhus, and H. Torp. Ultrasound based vessel wall tracking: an auto-correlation technique with rf center frequency estimation. *Ultrasound in Medicine & Biology*, 28:505–517, 2002.
- S. I. Rabben, N. Stergiopoulos, L. R. Hellevik, O. A. Smiseth, S. Slordahl, S. Urheim, and B. Angelsen. An ultrasound-based method for determining pulse wave velocity in superficial arteries. *Journal of Biomechanics*, 37:1615–1622, 2004.
- K. V. Ramnarine, D. K. Nassiri, P. R. Hoskins, and J. Lubbers. Validation of a new blood-mimicking fluid for use in Doppler flow test objects. *Ultrasound in Medicine & Biology*, 24(3):451–459, 1998.
- R. S. Reneman and A. P. G. Hoeks. Noninvasive vascular ultrasound: An asset in vascular medicine. *Cardiovascular Research*, 45:27–35, 2000.
- P. J. Reuderink, F. N. van de Vosse, A. A. van Steenhoven, M. E. H. van Dongen, and J. D. Janssen. Incompressible low-speed-ratio flow in non-uniform distensible tubes. *International Journal for Numerical Methods in Fluids*, 16:597–612, 1993.

- M. C. M. Rutten. *Fluid-solid interaction in large arteries*. PhD thesis, Eindhoven University of Technology, 1998.
- L. Sandrin, S. Manneville, and M. Fink. Ultrafast two-dimensional ultrasonic speckle velocimetry: a tool in flow imaging. *Applied Physics Letters*, pages 1155–1157, 2001.
- E. L. Schiffrin. Vascular stiffening and arterial compliance: implications for systolic blood pressure. *American Journal of Hypertension*, 17:39S–48S, 2004.
- H. Schlichting. *Boundary Layer Theory*. McGraw-Hill, New York, 1960.
- A. Segal. *SEPRAN introduction, user’s manual, programmer’s guide and standard problems*. Ingenieursbureau SEPRA, 2004.
- J. H. Siggers and S. L. Waters. Steady flows in pipes with finite curvature. *Physics of fluids*, 17(077102), 2005.
- J. H. Siggers and S. L. Waters. Unsteady flows in pipes with finite curvature. *Journal of Fluid Mechanics*, 600:133–165, 2008.
- N. Stergiopoulos, B. E. Westerhof, and N. Westerhof. Total arterial inertance as the fourth element of the windkessel model. *American Journal of Physiology*, 45:H81–H88, 1999.
- P. C. Struijk, J. W. Wladimiroff, W. C. J. Hop, and E. Simonazzi. Pulse pressure assessment in the human fetal descending aorta. *Ultrasound in Medicine & Biology*, 18:39–43, 1992.
- T. L. Szabo. *Diagnostic ultrasound imaging: inside out*. Elsevier Academic Press, 2004.
- C. A. Taylor, T. J. R. Hughes, and C. Zarins. Computational investigations in vascular disease. *Computers in Physics*, 10:224–232, 1996.
- C. A. Taylor, T. J. R. Hughes, and C. K. Zarins. Finite element modelling of blood flow in arteries. *Computer Methods in Applied Mechanics and Engineering*, 158: 155–196, 1998.
- M. G. Taylor. An experimental determination of the propagation of fluid oscillations in a tube with a viscoelastic wall; together with an analysis of the characteristics required in an electrical analogue. *Physics in Medicine and Biology*, 4:63–82, 1959.
- T. E. Tezduyar, S. Sathe, M. Schwaab, and B. S. Conklin. Arterial fluid mechanics modeling with the stabilized space-time fluid-structure interaction technique. *International Journal for Numerical Methods in Fluids*, 57(5):601–629, 2008a.
- T. E. Tezduyar, M. Schwaab, and S. Sathe. Sequentially-Coupled Fluid-Structure Interaction (SCAFSI) technique. *Computer Methods in Applied Mechanics and Engineering*, DOI: 10.1016/j.cma.2008.05.024, 2008b.

- H. C. Topakoglu. Laminar flows of an incompressible viscous fluid in curved pipes. *Journal of Mathematics and Mechanics*, 16(12):1321–1337, 1967.
- P. Tortoli, V. Michelassi, G. Bambi, F. Guidi, and D. Righi. Interaction between secondary velocities, flow pulsation and vessel morphology in the common carotid artery. *Ultrasound in Medicine & Biology*, 29(3):407–415, 2003.
- G. E. Trahey, J. W. Allison, and O. T. von Ramm. Angle independent ultrasonic detection of blood flow. *IEEE Transactions on Biomedical Engineering*, 34(12):965–967, 1987.
- J. Udesen and J. A. Jensen. Experimental investigation of transverse flow estimation using transverse oscillation. In *Proc IEEE Ultrason Symp*, pages 1586–1589, 2003.
- J. Udesen and J. A. Jensen. An in-vivo investigation of transverse flow estimation. *Proceedings of SPIE*, 5373:307–314, 2004.
- L. van Bortel, E. J. Balkestein, J. J. van der Heijden-Spek, F. H. Vanmolkot, J. A. Staessen, J. A. Kragten, J. W. Vredeveld, M. E. Safar, H. A. Struijker-Boudier, and A. P. G. Hoeks. Non-invasive assessment of local arterial pressure: Comparison of applanation tonometry and echo-tracking. *Journal of Hypertension*, 19:1037–1044, 2001.
- F. N. van de Vosse, J. de Hart, C. H. G. A. van Oijen, D. Bessems, T. W. M. Gunther, A. Segal, B. J. B. M. Wolters, J. M. A. Stijnen, and F. P. T. Baaijens. Finite-element-based computational methods for cardiovascular fluid-structure interaction. *Journal of Engineering Mathematics*, 47(3-4):335–368, 2003.
- C. N. van den Broek, R. A. Pullens, O. Frobert, M. C. M. Rutten, W. F. den Hartog, and F. N. van de Vosse. Medium with blood-analog mechanical properties for cardiovascular tissue culturing. *Biorheology*, 45(6):651–61, 2008.
- P. van Loon, W. Klip, and E. L. Bradley. Length-force and volume pressure relationship of arteries. *Biorheology*, 14:181–201, 1977.
- R. van Loon, P. D. Anderson, J. de Hart, and F. P. T. Baaijens. A combined fictitious domain/adaptive meshing method for fluid-structure interaction in heart valves. *International Journal for Numerical Methods in Fluids*, 46:533–544, 2004.
- A. C. Verkaik, B. W. A. M. M. Beulen, A. C. B. Bogaerds, M. C. M. Rutten, and F. N. van de Vosse. Estimation of volume flow in curved tubes based on analytical and computational analysis of axial velocity profiles. *Physics of fluids*, 21(2):023602–1/13, 2009.
- I. E. Vignon-Clementel, C. A. Figueroa, K. E. Jansen, and C. A. Taylor. Outflow boundary conditions for three-dimensional finite element modeling of blood flow and pressure in arteries. *Computer Methods in Applied Mechanics and Engineering*, 195:3776–3796, 2006.

- A. J. Ward-Smith. *Internal Fluid Flow*. Clarendon Press, Oxford, 1980.
- N. Westerhof, P. Sipkema, G. C. van den Bos, and G. Elzinga. Forward and backward waves in the arterial system. *Cardiovascular Research*, 6(6):648–656, 1972.
- J. Westerweel. *Digital particle image velocimetry - theory and application*. PhD thesis, Delft University, The Netherlands, 1993.
- J. Westerweel, D. Dabiri, and M. Gharib. The effect of a discrete offset on the accuracy of cross-correlation analysis of digital PIV recordings. *Experiments in Fluids*, 23:20–28, 1997.
- R. Williams, A. Needles, E. Cherin, S F. Foster, Y. Zhou, and M. Henkelman. A retrospective method for pulse-wave velocity measurements in the mouse. *IEEE Ultrasonics Symposium 1*, 1:381–384, 2005.
- R. Williams, A. Needles, E. Cherin, Y. Zhou, M R. Henkelman, S L. Adamson, and S F. Foster. Noninvasive ultrasonic measurement of regional and local pulse-wave velocity in mice. *Ultrasound in Medicine & Biology*, 33(9):1368–1375, 2007.
- R. A. Wilson, C. Di Mario, R. Krams, L. K. Soei, L. Wenguang, A. C. Laird, S H. The, E. Gussenhoven, P. Verdouw, and J R. Roelandt. In vivo measurement of regional large artery compliance by intravascular ultrasound under pentobarbital anesthesia. *Angiology*, 46:481–488, 1995.
- B. J. B. M. Wolters, M. C. M. Rutten, G. W. H. Schurink, U. Kose, J. de Hart, and F. N. van de Vosse. A patient-specific computational model of fluid-structure interaction in abdominal aortic aneurysms. *Medical Engineering & Physics*, 27: 871–883, 2005.
- J. R. Womersley. Method for the calculation of velocity, rate of flow and viscous drag in arteries when the pressure gradient is known. *Journal of Physiology*, 127:553–563, 1955.
- Y. W. Yuan and K. K. Shung. Echoicity of whole blood. *Journal of Ultrasound in Medicine*, 8:425–434, 1989.
- C. K. Zarins, D. P. Giddens, B. K. Bharadvaj, V. S. Sottiurai, R. F. Mabon, and S. Glagov. Quantitative correlation of plaque localization with flow velocity profiles and wall shear stress. *Circulation Research*, 53:502–514, 1983.



## Appendix A

# Analytical solutions for the axial velocity ( $w$ )

In this appendix the results of the analytical approximation methods of Dean, Topakoglu and Siggers & Waters with respect to the axial velocity ( $w$ ) are shown. It should be noticed that all authors used different scaling and non-dimensionalisation methods, which are not explicitly stated here and for which we would like to refer to the corresponding articles.

### A.1 Derivation by Dean

Dean derived a higher order series solution expanded in  $K$  to describe the fully developed, steady flow analytically in a tube with a small  $K$ -number, which results for the axial velocity in:

$$w = w_0 + Kw_1 + K^2w_2 + \dots \quad (\text{A.1})$$

The solutions obtained from the series expansion are given by:

$$w_0 = 1 - r'^2, \quad (\text{A.2})$$

$$w_1 = \frac{\cos \theta}{576} \left( \frac{19r'}{40} - r'^3 + \frac{3r'^5}{4} - \frac{r'^7}{4} + \frac{r'^9}{40} \right), \quad (\text{A.3})$$

where  $r' = r/a$ .

## A.2 Derivation by Topakoglu

Topakoglu performed a power series expansion in  $\delta$  and by insertion of:

$$w = w_0 + \delta w_1 + \delta^2 w_2 + \dots \quad (\text{A.4})$$

Topakoglu derived the following equations, describing the axial velocity:

$$w_0 = f_0 = Re(1 - r'^2), \quad (\text{A.5})$$

and

$$w_1 = f_1 \cos \theta, \quad (\text{A.6})$$

where

$$f_1 = -\frac{3}{4}f_0 \left[ 1 - \frac{1}{8640} Re^2 (19 - 21r'^2 + 9r'^4 + r'^6) \right] r' \quad (\text{A.7})$$

and finally

$$w_2 = f_{20} + f_{22} \cos 2\theta, \quad (\text{A.8})$$

where

$$\begin{aligned} f_{20} = \frac{-1}{32} f_0 \left\{ 3 - 11r'^2 + \frac{1}{7200} Re^2 [148 + 43r'^2 - 132r'^4 + \right. \\ \left. + 68r'^6 - 7r'^8 \frac{1}{3225.6} Re^2 (823.8 - 3432.2r'^2 + 5835.8r'^4 - \right. \\ \left. 5252.2r'^6 + 2713.8r'^8 - 803r'^{10} + 121r'^{12} - 7r'^{14})] \right\} \end{aligned} \quad (\text{A.9})$$

and

$$\begin{aligned} f_{22} = \frac{1}{8} \left\{ 2.5 - \frac{1}{3456} Re^2 [46.3 - 61.3r'^2 + 29.6r'^4 - 4r'^6 - \right. \\ \left. \frac{1}{42336} Re^2 (1456.9 - 2402.06r'^2 + 1746.49r'^4 - 705.47r'^6 + \right. \\ \left. 191.23r'^8 - 28.01r'^{10} + 1.6r'^{12})] \right\} r'^2. \end{aligned} \quad (\text{A.10})$$

## A.3 Derivation by Siggers & Waters

Siggers & Waters used a series solution for  $w$  expanded in  $Dn$ , where  $w_k$  is allowed to depend on  $\delta$  to derive a solution for the axial velocity

$$w = Dn \sum_{k=0}^{\infty} Dn^{2k} w_k, \quad (\text{A.11})$$

with

$$w_k = \sum_{j=0}^{\infty} \delta^j w_{kj} = w_{k0} + \delta w_{k1} + \delta^2 w_{k2} + \dots, \quad (\text{A.12})$$

with

$$w_{00} = \frac{1}{4}(1 - r'^2), \quad (\text{A.13})$$

$$w_{01} = -\frac{3}{16}r'(1 - r'^2) \cos \theta, \quad (\text{A.14})$$

$$w_{02} = \frac{1}{128}(1 - r'^2)(-3 + 11r'^2 + 10r'^2 \cos 2\theta). \quad (\text{A.15})$$

To get the  $O(Dn^3)$  solution they set  $w_1 = w_1^{[1]} + w_1^{[2]}$ , with  $w_1^{[1]} = w_{10}^{[1]} + \delta w_{11}^{[1]} + \dots$  and  $w_2^{[1]} = w_{10}^{[2]} + \delta w_{11}^{[2]} + \dots$ , with:

$$w_{10}^{[1]} = \frac{1}{2^{15} \cdot 3^2 \cdot 5} r'(1 - r'^2)(19 - 21r'^2 + 9r'^4 - r'^6) \cos \theta, \quad (\text{A.16})$$

$$w_{11}^{[1]} = \frac{1}{2^{18} \cdot 3^3 \cdot 5^2} (1 - r'^2) [6(109 - 586r'^2 + 689r'^4 - 311r'^6 + 39r'^8) - 5r'^2(163 - 193r'^2 + 86r'^4 - 10r'^6) \cos 2\theta] \quad (\text{A.17})$$

and

$$w_{10}^{[2]} = 0, \quad (\text{A.18})$$

$$w_{11}^{[2]} = \frac{1}{2^{17} \cdot 3^2 \cdot 5^2} (1 - r'^2) [-(257 - 543r'^2 + 557r'^4 - 243r'^6 + 32r'^8) - 25r'^2(10 - 14r'^2 + 7r'^4 - r'^6) \cos 2\theta]. \quad (\text{A.19})$$

Some more equations for higher order derivations were shown, but the explicit solutions were not stated.



## Samenvatting

Ultrageluid wordt in de kliniek vaak toegepast om op een niet-invasieve manier geometrische eigenschappen van grote vaten, zoals diameter en wanddikte en hemodynamische variabelen zoals bloedstroomsnelheid te bepalen. Om biomechanische parameters en hemodynamische variabelen die karakteristiek zijn voor de ontwikkeling van hart en vaatziekten, zoals compliantie en impedantie, te bepalen, is de bepaling van geometrie en bloedstroomsnelheid alleen onvoldoende. Daarvoor is een gelijktijdige en bij voorkeur niet invasieve meting van debiet en druk vereist.

Met de huidige ultrageluidstechnieken is het onmogelijk om gelijktijdig debiet en druk nauwkeurig te bepalen. Debiet wordt vaak bepaald aan de hand van twee metingen: een diametermeting (geluidsbundel loodrecht op het vat) en een meting van de maximale axiale bloedstroomsnelheid met behulp van Doppler ultrageluid (geluidsbundel onder een hoek met het vat). Door een theoretische snelheidsverdeling aan te nemen, bijvoorbeeld een Poiseuille of Womersley profiel, wordt hieruit vervolgens het debiet berekend. In-vivo zijn vaten zelden recht: vaten zijn taps toelopend, gekromd en hebben vertakkingen. Dientengevolge zijn er secundaire snelheidscomponenten aanwezig die de axiale snelheidsverdeling beïnvloeden. Dit resulteert in asymmetrische axiale snelheidsverdelingen. Omdat de aangenomen snelheidsverdelingen slechts geldig zijn voor rechte vaten, geeft een dussdanige bepaling een onnauwkeurige afschatting van het debiet. Verder is het onmogelijk om gelijktijdig met de snelheidsmeting nauwkeurig de wandbeweging te bepalen, waardoor de debietmeting nog verder verslechtert en het gelijktijdig bepalen van druk uit wandbeweging en debiet onmogelijk wordt.

In dit onderzoek worden Particle Image Velocimetry (PIV) gebaseerde algoritmen toegepast op RF-data die verkregen zijn met behulp van een commercieel beschikbaar, voor klinische toepassing goedgekeurd ultrageluidssysteem. Dit maakt het mogelijk om snelheidscomponenten loodrecht op de ultrageluidbundel, en dus gelijktijdig wandpositie en axiale snelheid nauwkeurig te meten. Deze snelheidsmeettechniek is gevalideerd door metingen van het snelheidsprofiel in een experimentele opstelling te vergelijken met resultaten van computational fluid dynamics (CFD) berekeningen, voor stationaire en instationaire stromingen in een recht vat. Er werd een goede overeenstemming gevonden voor het axiale snelheidsprofiel. Integratie van het gemeten axiale snelheidsprofiel leverde een nauwkeurige afschatting

van het debiet op.

Omdat in de praktijk de meeste vaten gekromd zijn is de snelheids meetmethode vervolgens gevalideerd voor toepassing op stromingen in dit soort geometrieën. In de experimentele opstelling zijn axiale snelheidsprofielen gemeten voor stationaire en instationaire stroming in kromme buizen. Opnieuw zijn de gemeten profielen vergeleken met resultaten van CFD-berekeningen. Ook hier werd een goede overeenstemming gevonden tussen de gemeten profielen en de met behulp van CFD berekende snelheidsprofielen.

Om nauwkeurig debiet te bepalen op basis van de gemeten asymmetrische axiale snelheidsprofielen, is een analytische en een op CFD gebaseerde studie gedaan naar stroming in kromme vaten. Deze studie heeft geresulteerd in de  $\cos \theta$ -methode. Toepassing van de  $\cos \theta$ -methode op de gemeten asymmetrische axiale profielen gaf een nauwkeurige afschatting van het debiet, voor stationaire en instationaire flow. Vergeleken met de huidig toegepaste afschattingsmethode voor het debiet werd een grote verbetering gevonden. Voor een fysiologisch relevant debiet gaf de  $\cos \theta$ -methode een gemiddelde afwijking van 5% ten opzichte van het referentiedebiet terwijl deze voor de huidig toegepaste Poiseuille en Womersley benaderingen gelijk was aan 20%.

Tenslotte is getracht om de lokale druk te bepalen uit enkel een niet-invasieve ultrageluidsmeting door een meting van de diameter te combineren met een gelijktijdige bepaling van de lokale compliantie. De lokale compliantie is bepaald door de lokale golfsnelheid (PWV) te meten. Verschillende methoden om lokaal de PWV te meten zijn getest in de experimentele opstelling. Hieruit bleek dat de QA-methode, een methode waarbij de lokale PWV bepaald wordt uit de verhouding tussen veranderingen in debiet en veranderingen in oppervlak van de dwarsdoorsnede van het vat, het mogelijk maakt om lokaal nauwkeurig PWV te meten. Door de PWV meting te combineren met een gelijktijdige meting van de diameter werd de lokale druk nauwkeurig afgeschat. Dit geeft aan dat het haalbaar is om op een niet-invasieve manier in-vivo druk te meten met behulp van ultrageluid.

Hoewel de meettechnieken besproken in deze studie alleen getest zijn voor toepassing in een gecontroleerde experimentele omgeving, zijn de vooruitzichten voor klinische toepassing veelbelovend. De gepresenteerde methoden maken het mogelijk om de toestand van het vaatbed nauwkeuriger te bepalen, waardoor in de toekomst informatie verkregen kan worden over het effect van therapeutische ingrepen en factoren geïdentificeerd kunnen worden die karakteristiek zijn voor de ontwikkeling van hart- en vaatziekten.

## Dankwoord

Graag wil ik een aantal mensen bedanken die bijgedragen hebben aan het tot stand komen van dit proefschrift. Ten eerste wil ik mijn directe begeleiders bedanken. Frans, ik heb het erg kunnen waarderen dat je wekelijks tijd vrij maakte voor een overleg. Bedankt voor al de nuttige input die je me gegeven hebt en de vrijheid die ik gekregen heb bij het uitvoeren van dit promotieonderzoek. Marcel, jou wil ik met name bedanken voor je kundige adviezen betreffende het opzetten en verrichten van de experimenten. Ik heb de discussies die we gehad hebben bij de totstandkoming van dit proefschrift ook zeer gewaardeerd.

Ik wil de mannen van Hemolab, Jurgen, Marco en Sjoerd, bedanken voor de ondersteuning bij het ontwerpen en vervaardigen van de diverse onderdelen voor de experimentele opstelling. Leo en Patrick wil ik bedanken voor de hard- en software support die vereist was voor het uitvoeren van de diverse Sepran simulaties. Ik wil mijn collega's in het Art.Med project bedanken voor de samenwerking. Verder wil ik mijn afstudeerders, Anna Catharina, Gregory, Olga en Rebeca bedanken voor hun bijdrage aan dit onderzoek, maar ook voor de prettige ervaringen die ik zelf als begeleider heb opgedaan. Tenslotte wil ik mijn kamergenoten en collega's die ik in de loop van de jaren gehad heb bedanken voor de gezelligheid en afleiding.

Ook een aantal mensen buiten de werkkring wil ik bedanken. Bram, Dennis, Jack, Robert en Tim, onze diverse mountainbike trips en wekelijkse squash activiteiten hebben voor de nodige ontspanning en plezier gezorgd. Dennis, broertje, in het bijzonder wil ik jou en Anneke bedanken voor de steun en vriendschap gedurende de afgelopen jaren.

Ik wil mijn familie bedanken voor hun interesse in mij en mijn werk. Pap en mam, bedankt voor alle steun en het onvoorwaardelijke vertrouwen dat jullie altijd in me gehad hebben. Zonder de mogelijkheden die jullie me geboden hebben was ik nooit zo ver gekomen.

De laatste woorden zijn gereserveerd voor Marleen. Bedankt voor je geduld en begrip, jouw steun is voor mij van onbetaalbare waarde.



## Curriculum Vitae

Bart Beulen werd geboren op 15 september 1981 te Geleen. In 1999 behaalde hij zijn VWO diploma aan het Bisschoppelijk College Schöndeln te Roermond. Tijdens zijn opleiding Technische Natuurkunde aan de Technische Universiteit Eindhoven liep hij stage bij Océ Technologies B.V. waar hij onderzoek verrichte naar de dynamica van luchtbellen in inktjet printkoppen. Zijn afstudeerwerk vond wederom plaats bij Océ Technologies B.V., waar hij onderzoek verrichte naar stroming op de nozzleplaat van een inktjet printkop. In 2005 studeerde hij af waarna hij startte met een promotieonderzoek aan de faculteit Biomedische Technologie van de Technische Universiteit Eindhoven. Dit promotieonderzoek heeft hij verricht in de groep Cardiovasculaire Biomechanica en heeft geleid tot dit proefschrift.